

CHARACTERIZATION AND THERMODYNAMIC STABILITY OF WEYL
SEMIMETALS

DEVELOPMENT OF *AB INITIO* CHARACTERIZATION TOOL FOR
WEYL SEMIMETALS AND THERMODYNAMIC STABILITY OF
KAGOME WEYL SEMIMETALS

By Himanshu SAINI,

*A Thesis Submitted to the School of Graduate Studies in the Partial Fulfillment
of the Requirements for the Degree Master of Applied Science*

McMaster University © Copyright by Himanshu SAINI April 26, 2023

McMaster University

Master of Applied Science (2023)

Hamilton, Ontario (Department of Materials Science and Engineering)

TITLE: Development of *ab initio* characterization tool for Weyl semimetals and thermodynamic stability of kagome Weyl semimetals

AUTHOR: Himanshu SAINI (McMaster University)

SUPERVISOR: Dr. Oleg RUBEL

NUMBER OF PAGES: xi, 135

Abstract

Topological materials have discovered ultrahigh magnetoresistance, chiral anomalies, the inherent anomalous Hall effect, and unique Fermi arc surface states. Topological materials now include insulators, metals, and semimetals. Weyl semimetals (WSM) are topological materials that show linear dispersion with crossings in their band structure which creates the pair of Weyl nodes of opposite chirality. WSMs have topological Fermi arc surface states connecting opposing chirality Weyl nodes. Spin-orbit coupling can result in the band opening in Dirac nodal rings, and creating the pair of Weyl nodes either by breaking the time-reversal or spatial inversion symmetry (but not both) [1–3]. The chirality of a Weyl node is set by the Berry flux through a closed surface in reciprocal space around it. The purpose of this thesis was to characterize and investigate the thermodynamic stability of WSM. To accomplish these goals, quantum mechanical modeling at the level of density functional theory (DFT) was used.

`WloopPHI`, a Python module, integrates the characterization of WSMs into `WIEN2k`, a full-potential all-electron density functional theory package. It calculates the chirality of the Weyl node (monopole charge) with an enhanced Wilson loop method and Berry phase approach. First, TaAs, a well-characterized Weyl semimetal, validates the code theoretically. We then used the approach to characterize the newly discovered WSM YRh_6Ge_4 , and we found a set of Weyl points into it.

Further, we study the stability of the kagome-based materials $\text{A}_3\text{Sn}_2\text{S}_2$, where A is Co, Rh, or Ru, in the context of the ternary phase diagrams and competing binary compounds using DFT. We demonstrated that $\text{Co}_3\text{Sn}_2\text{S}_2$ and $\text{Rh}_3\text{Sn}_2\text{S}_2$ are stable compounds by examining the convex hull and ternary phase diagrams. It is feasible to synthesize $\text{Co}_3\text{Sn}_2\text{S}_2$ by a chemical reaction between SnS, CoSn and Co_9S_8 . Moreover, $\text{Rh}_3\text{Sn}_2\text{S}_2$ can be produced by SnS, RhSn and Rh_3S_4 . On the other hand, we found that $\text{Ru}_3\text{Sn}_2\text{S}_2$ is a thermodynamically unstable material with respect to RuS_2 , Ru_3S_7 and Ru. Our work provides some insights for confirming materials using the DFT approach.

Acknowledgements

I would like to express my sincere appreciation to my supervisor, Prof. Oleg Rubel, for providing me with the invaluable chance to conduct my graduate studies under his supervision. I am really grateful for his professional guidance in the complex world of density functional theory, as well as his gracious feedback and fast support with any work that arose.

Furthermore, I'd like to thank Dr. Marek Niewczas and Dr. Adrian Kitai from my supervisory committee for their essential research suggestions. I'd also like to thank my Rubel group colleagues, Magdalena Laurien, Larissa Grigat, Coulton Boucher, Andres Gomez, and Caio Miliante, for their constant support. Their company and unwavering readiness to help have been invaluable to me on my trip.

My heartfelt appreciation goes to my parents, whose loving and consistent support for my scientific interests has made a huge difference in my life. I am also grateful to Nishtha Piplani for her unwavering dedication, kindness, and patience in both supporting and challenging me. I'm particularly thankful to Mary Bik and Stéphanie Bellemare for their constant support and informative conversations during this journey.

Finally, thank you for your love and care, which have been a constant source of inspiration and encouragement for all of my family and friends, both close and far.

Contents

Abstract	iii
Acknowledgements	iv
Declaration of Authorship	xi
1 Introduction	1
1.1 Motivation	1
1.2 Structure of this thesis	3
2 Basic Concepts and Literature Review	4
2.1 Topological materials	4
2.2 Topological Weyl semimetals	4
2.3 Chirality of Weyl semimetals	5
2.3.1 Berry phase, Berry curvature and Berry flux	5
2.3.2 Numerical implementation of Berry phase methodology for identifying topological materials	7
2.4 Topological kagome materials	9
2.4.1 Weyl points in the magnetic Weyl semimetal $\text{Co}_3\text{Sn}_2\text{S}_2$	10
2.4.2 Anomalous Hall effect in $\text{Co}_3\text{Sn}_2\text{S}_2$	12
2.5 Formability of Kagome lattice based materials	15
3 Computational method	18
3.1 Density Functional Theory	20
3.1.1 The Hohenberg–Kohn Theorems	20
3.1.2 The Kohn–Sham Auxiliary System	22
4 Characterization of Weyl semimetals using WloopPHI	26
4.1 Introduction	27
4.2 Method	31

4.2.1	Chirality of a Weyl point	31
4.2.2	Program implementation	32
4.2.3	Sample work flow	34
4.2.4	Convergence and reliability tests	39
4.3	Results	43
4.3.1	TaAs: method verification	43
4.3.2	YRh ₆ Ge ₄	44
4.4	Conclusion	46
5	Thermodynamic stability of kagome lattice A₃Sn₂S₂: (A: Co, Rh, Ru)	48
5.1	Introduction	49
5.2	Methodology	50
5.2.1	Thermodynamic Stability	51
5.2.2	Formation energy predictions	54
5.2.3	Computational details for first-principles calculations	55
5.3	Results and Discussion	57
5.4	Conclusion	67
A	Chapter 4 Supplement: Block diagram of WloopPHI code.	69
B	Chapter 5 Supplement: Finite temperature correction in DFT calculated formation energies.	71
C	Chapter 5 Supplement: DFT input files for all the structures.	74
D	Chapter 5 Supplement: Python code for ternary phase diagram	113
D.1	main.py	114
D.2	GenerateData.py	115
D.3	PhaseDiagram.py	118
D.4	Phase diagrams and convex Hull using ASE Python Package [101]	125
	Bibliography	128

List of Figures

1.1	Concepts in quantum materials.	2
2.1	Schematic band crossings and band structure.	5
2.2	Berry curvature.	6
2.3	Loops around the sphere on which WCC are computed.	8
2.4	Kagome lattice.	10
2.5	Electronic structure of $\text{Co}_3\text{Sn}_2\text{S}_2/\text{Se}_2$	12
2.6	Berry curvature contribution to AHE.	14
2.7	Transport measurements of the anomalous Hall angle.	15
2.8	The crystal structure of $\text{Co}_3MM'X_2$	16
2.9	Stable configurations of Co-based compounds.	17
3.1	Illustration of DFT.	21
3.2	Schematic representation of Hohenberg–Kohn theorem.	21
3.3	Schematic representation of Kohn–Sham auxiliary system.	23
4.1	(a) Weyl nodes of opposite chirality at the intercept of two bands. Arrows indicate the source (red) and sink (blue) of the Berry curvature $\nabla_{\mathbf{k}} \times \mathbf{A}_n$. (b) The node can be viewed as a monopole with a chiral charge (positive node is shown with the chirality $\chi = +1$). The charge is determined by a Berry flux through a closed surface S that encloses the Weyl node. (c) Construction of a series of Wilson loops that enclose one Weyl node. There is a Berry phase ϕ associated with each loop that represents a Berry flux through the surface S' of the loop. (d) Use of a right-hand rule in definition of a positive direction of the Berry flux through the loop. (e) Evolution of Berry phase (wrapped in the range $[-\pi, +\pi]$) as a function of the loop’s position along the k_z direction. The discontinuity (marked with an arrow) corresponds to a Weyl point. (f) A finite Berry phase (unwrapped) accumulates as the Wilson loop traverses through the BZ. The accumulated phase represents the chirality $\chi = +1$ of the Weyl point.	29

4.2	(a) The crystal structure of TaAs. (b) The bulk Brillouin zone. (c) Band structure calculated with the PBE functional without SOC. Energies are plotted relative to the Fermi energy. (d) Band structure with SOC. The Berry phase calculations include band 84 only.	34
4.3	Characterization Weyl points in TaAs using the extended Wilson loop method. (a) BZ projections with Weyl points in questions. The loops and their trajectories are shown. Arrows indicate the order in which k points are assembled in the loop. (b,c,d) Evolution of the Berry flux through three different loops along their trajectories. (b) Two positive Weyl points. (c) Two negative Weyl points. (d) A pair of Weyl points of opposite chirality.	38
4.4	Effect of the Wilson loop size on evaluation of the Weyl node chirality in TaAs. (a) Brillouin zone with loops of various sizes (large, intermediate, and small). (b,d,f) Evolution of the Berry phase (wrapped) for large, intermediate, and small loops, respectively. (c,e,d) The same for the unwrapped Berry phase. The Weyl point identification using the largest loop has failed since other neighbouring Weyl point also contribute to the Berry flux and obstruct the result. Smaller loop sizes are preferable to achieve reliable data.	40
4.5	Effect of the number of intermediate Wilson loops along the loop trajectory on evaluation of the Weyl node chirality in TaAs: (a) Brillouin zone with Weyl nodes (only two relevant ones are shown), Wilson loop and its trajectory. (b,c), (d,e), (f,g) Evolution of wrapped and unwrapped Berry phase $\phi(k)$ along the loop trajectory sampled with 21, 91 and 551 equally spaced Wilson loops, respectively. The data get smoother and more reliable as the number of Wilson loops increases. Only with the highest mesh number we can clearly resolve two 2π discontinuities on the panel (f), which correspond to two Weyl points of opposite chirality $\chi = -1$ (left) and $\chi = +1$ (right).	42
4.6	Mapping of Weyl points in the BZ of TaAs. (a,b) Top and side view of BZ. There are in total 12 pairs of Weyl points with $+1$ and -1 chirality marked as red and blue circles, respectively.	43

4.7	(a) Crystal structure of YRh_6Ge_4 . (b) Bulk BZ. (c) Band structure calculated with the PBE functional without SOC. Band crossings with two-fold degeneracies (excluding spin) are labelled $x4$. (d) Band structure with SOC. The proximity to the Weyl point is identified on a path between high-symmetry k points. TDPs refers to a pair of triply degenerate points.	45
4.8	Mapping of Weyl point in the Brillouin zone of YRh_6Ge_4 : (a,b) The top and side view of the Brillouin zone. Weyl points are shown with red and blue solid circles. (c) Evolution of the Berry flux through the Wilson loops along its trajectory allows to identify a k_z coordinate, the sign and chirality of Weyl points.	46
5.1	Illustration of convex hull diagram.	52
5.2	Illustration of ternary phase diagram using python code.	57
5.3	Structure of $\text{A}_3\text{Sn}_2\text{S}_2$ ($A = \text{Co}, \text{Rh}, \text{and Ru}$).	58
5.4	Binary convex Hull diagrams.	60
5.5	Ternary phase diagrams.	64
5.6	Reaction prediction using ternary phase diagram.	67
A.1	Block diagram of <code>WloopPHI</code> code.	70
B.1	Calculation procedure for forsterite. Reprint with permission from [107], copyright 2018 Springer Nature. This article has Open Access permission under the terms of the Creative Commons Attribution 4.0 International License .	73
D.1	Format for the <code>Co3Sn2S2.csv</code> file.	115
D.2	Illustration of ternary phase diagram using python code.	119
D.3	Illustration of ternary phase diagram using ASE python package [101]. (a) Ternary phase diagram with binary phase only, (b) Ternary phase diagram with ternary compound, and (c) Convex Hull diagram for Co-S	127

List of Tables

5.1	Atomic radii and oxidation states data.	50
5.2	Formation enthalpies of Binary Polymorphs.	61
5.3	Chemical accuracy of formation energy.	63
5.4	Formation enthalpies of reactants and product.	65
5.5	Reactions and the reaction energies.	66

Declaration of Authorship

I, Himanshu SAINI, declare that this thesis titled, “Development of *ab initio* characterization tool for Weyl semimetals and thermodynamic stability of kagome Weyl semimetals” and the work presented in it are my own. I confirm that:

- Chapter 2, The explanation is adapted from the textbook: Berry phases in electronic structure theory [4] and from the article [5].
- Chapter 3, The explanation in this chapter was adapted from the two textbooks: Materials Modelling using Density Functional Theory [6], and Electronic Structure Basic Theory and Practical Methods [7].
- Chapter 4, Characterization of Weyl semimetals using WloopPHI. The code was implemented by me. I conducted the calculations and data analysis for Weyl points. The first draft was written by me and afterwards during revisions by Dr. Oleg Rubel the manuscript was mostly modified including figures.
- Chapter 5, Thermodynamic stability of kagome lattice $A_3Sn_2S_2$: (A: Co, Rh, Ru). I conceived the idea and perform all the calculations and data analysis. I also have developed the code in Python for ternary phase diagram. Explanation in methodology section is adapted from the recently published article on computational approaches to predict the thermodynamic stability of inorganic solids [8]

Chapter 1

Introduction

1.1 Motivation

In ordinary electronic devices, information processing and communication are accomplished by the flow of electric charges. These devices are based on semiconductors that are not magnetic. Spintronic devices, on the other hand, utilise the spin of electrons to regulate charge currents. By integrating processing, storage, sensing, and logic into a single platform, spintronics could complement and, in some situations, outperform semiconductor-based electronics, giving advantages in terms of scale, power consumption, and data processing speed [9]. Since the discovery of gigantic magnetoresistance (GMR) in 1988, in the field of spintronics numerous fascinating phenomena have discovered. Spin-transfer torque (STT) and spin-orbit torque (SOT), giant tunnelling magnetoresistance (TMR) in MgO-based magnetic tunnel junctions (MTJs), and large interfacial magnetic anisotropy at magnetic metal/oxide interfaces have paved the way for the development of scalable nonvolatile magnetic random-access memories (MRAMs) [10]. In order for spintronic devices to meet the growing need for high-speed, high-density, and low-power electronic components, additional advances in the design of materials are necessary.

In the last two decades, new concepts have been established for many-body systems, revealing never-before-observed features, phenomena, and functions. These materials are quantum materials, and they exhibit the novel and special properties that result from strong interactions between the elements, such as the Mott transition, high-temperature superconductivity, topological electronics, quantum computing, and giant magnetoelectric effect, as depicted in Fig 1.1a [11]. In solids, electrons have several degrees of freedom, including charge, spin, orbital, topology, and lattice structure, as depicted schematically in Fig. 1.1b. Atomic potential on the crystal lattice structure determines the topological

characteristics. Recent advancements in our understanding of quantum materials are centred on the topological nature of the electronic states [11].

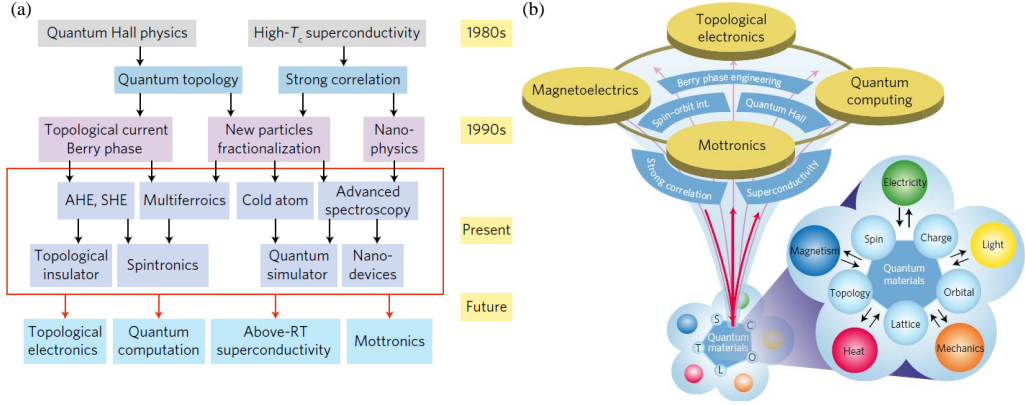


FIGURE 1.1: (a) A concise overview of the studies on the physics of quantum materials and functions. (b) The pentagon at the bottom illustrates the varying degrees of freedom of tightly correlated electrons in materials that respond to external stimuli. These high couplings lead to emergent functions with cross correlations between distinct physical observables, as well as developments in emergent function applications, such as Mottronics, magnetoelectrics, topological electronics, and quantum computing. Reprint with permission from [11], copyright 2017 Springer Nature.

New phenomena, including ultrahigh magnetoresistance [12], chiral anomaly [13–17], the intrinsic anomalous Hall effect [18–22], and exotic Fermi arc surface states [23, 24], have been predicted and discovered thanks to developments in the field of topological materials [25–29]. The range of topological materials has broadened to include metals and semimetals in addition to insulators [14, 30–32]. Weyl semimetals are classified as topological materials possessing Fermi surface Chern numbers that are non-zero and enclosing the band crossing point known as the Weyl point (or Weyl nodes). This point is characterised as a singular point of Berry curvature or a "magnetic monopole" in momentum space [3]. The unusual electrical properties of magnetic Weyl semimetals make them excellent candidate for spintronic devices. They exhibit isolated degeneracies between valence and conduction bands in the 3D Brillouin zone (BZ), as well as an enormous Berry curvature that is projected to cause an intrinsic anomalous Hall effect as a result of both extrinsic scattering and an inherent mechanism connected with its curvature [21]. Magnetic Weyl semimetals can be thought of as a stack of quantum anomalous Hall insulator layers in which coupling between them closes the bulk band gap at isolated Weyl nodes [21].

Recently, several promising candidates for magnetic Weyl semimetals have been proposed, like $\text{Y}_2\text{Ir}_2\text{O}_7$, HgCr_2Se_4 , and some Co_2 -based Heusler compounds [23, 33–36]. The experimental identification of these materials is also under progress; for instance, 16% anomalous Hall angle is observed in the magnetic field induced Weyl semimetal GdPtBi [19]. To create GdPtBi a Weyl semimetal, however, a finite external magnetic field is required. Therefore, the search for intrinsic magnetic Weyl semimetals with Weyl nodes close to the Fermi level is an effective technique for obtaining materials for spintronic devices that exhibit both a high anomalous Hall conductivity and a large anomalous Hall angle.

The kagome lattice exhibits exotic topological states with out-of-plane magnetization in condensed matter physics. Consequently, it is an ideal platform for studying the quantum anomalous Hall effect [37, 38]. The kagome lattice is a two-dimensional arrangement of triangles with shared corners. These geometries symbolise the concept of frustration, which refers to the existence of competing forces that cannot be fulfilled simultaneously. *Frustrated magnets* are materials in which localised magnetic moments, or spins, interact through competing exchange interactions that cannot be concurrently satisfied, leading to a substantial degeneracy in the ground state of the system [39]. Recently, transition-metal-based kagome magnets with enormous Berry curvature fields and exceptional magnetic tunability have exhibited anomalous Hall effect. In this family, the kagome magnet $\text{Co}_3\text{Sn}_2\text{S}_2$ is recognised as a viable Weyl semimetal candidate due to the presence of Weyl nodes in the BZ. Moreover, they also exhibit strong anomalous Hall effect and anomalous Hall angle [40].

The purpose of this thesis was to theoretically characterize Weyl Semimetals with an emphasis on their thermodynamic stability using cutting-edge predictive physical modelling. We examined and characterized the existing and newly proposed Weyl semimetals with theoretical methods in order to highlight their features and add to the knowledge of material design.

1.2 Structure of this thesis

The structure of this thesis is as follows: In Chapter 2, I present fundamental principles relevant to my investigation. In Chapter 3, I introduce the computational methodology. In Chapters 4 and 5, I then discuss the research outcomes achieved during my graduate studies.

Chapter 2

Basic Concepts and Literature Review

2.1 Topological materials

In mathematics, topology is about the same basic properties of an object even the object is deformed. The deformation does not include any tearing in the object, and hence it classifies the object based on the number of holes [41]. Similarly, in materials, the properties that are invariant under smooth deformation are known as topological materials. These materials are insulators, metals, and semimetals in nature [41].

2.2 Topological Weyl semimetals

Weyl semimetals can be understood better with the analogy of three-dimensional generalization of graphene because it exhibits linearly dispersion cone structure formed by energy band crossings [42]. It is similar to Dirac semimetals, but they are different from Weyl semimetals. Dirac semimetals possess four-fold band crossing (Dirac point) because of having both inversion symmetry (\mathcal{P}) and time-reversal symmetry (\mathcal{T}), which gives rise to the doubly degenerate band-structure and four-fold degeneracy of Dirac point [42]. In comparison, Weyl semimetals have two-fold band crossings (Weyl points) because it does not simultaneously have \mathcal{P} and \mathcal{T} , which lifts the two-fold degeneracy of energy bands [42]. The resulting non-degenerate bands are only two-fold degenerate, as shown in Fig. 2.1.

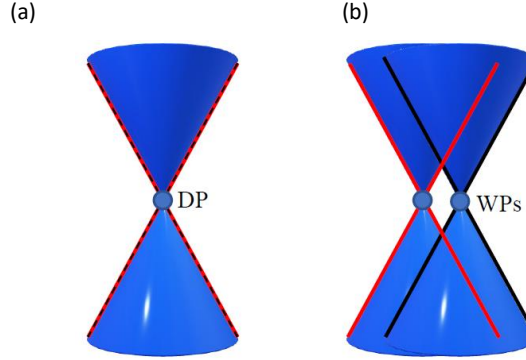


FIGURE 2.1: (a)Dirac semimetals, whose conduction and valence bands cross at a single point with doubly degenerate, resulting in a four-fold crossing point known as a Dirac point (DP). (b) Non-degenerate conduction and valence band crossing in Weyl semimetals, and the crossing is two-fold Weyl points (WPs).

2.3 Chirality of Weyl semimetals

2.3.1 Berry phase, Berry curvature and Berry flux

The description in this section is covered from the text book "Berry phases in electronic structure theory" [4].

A "Berry phase" is a phase angle that ranges from 0 to 2π and illustrates the global phase evolution of a complex vector as it traverses along a path in its vector space. This phase angle is also known as a "Berry phase angle." Moreover, one may refer to it as a "geometric phase" or a "Pancharatnam phase". The Berry phase in the continuous formulation is [4]

$$\phi = \oint \langle u_\lambda | i\partial_\lambda u_\lambda \rangle d\lambda. \quad (2.1)$$

The right hand side integrand is known as the *Berry connection* or *Berry potential* [4],

$$A(\lambda) = \langle u_\lambda | i\partial_\lambda u_\lambda \rangle = -Im\langle u_\lambda | \partial_\lambda u_\lambda \rangle. \quad (2.2)$$

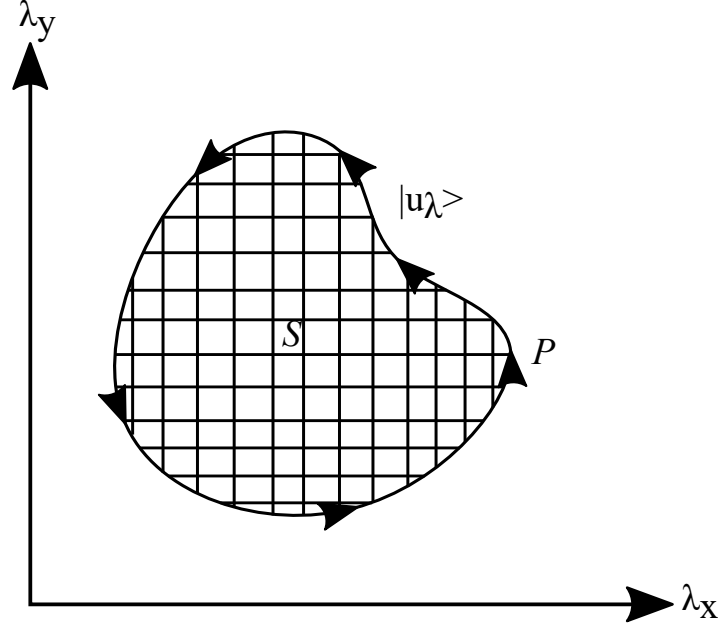


FIGURE 2.2: Region S of a two-dimensional parameter space, bounded by loop P . Reprint with permission from [4], copyright 2018 Cambridge University Press.

In a two-dimensional parameter space as shown in Fig. 2.2, where any vector can be defined as a function of two variables. The Berry curvature is defined as the Berry phase per unit area in this space. In a discretized context, the Berry curvature can be calculated as the Berry phase surrounding a small area, divided by the area of that region. In a continuum framework, it becomes the curl of Berry connection [4].

$$\Omega(\lambda) = \partial_x A_y - \partial_y A_x = -2Im \langle \partial_x u | \partial_y u \rangle. \quad (2.3)$$

After the Berry curvature has been described as a curl, Stokes' theorem can be used to relate the "Berry flux" through a surface region S to the Berry phase around the boundary. This can be done by determining the relationship between the two quantities. This indicates that it is possible to determine the entire amount of Berry flux that is transmitted through a surface by integrating the Berry curvature over the surface, and this result is equivalent to the Berry phase that is present around the perimeter of the surface.

In the continuum limit, the Berry flux computed on a closed 2D manifold is quantized and equal to 2π times an integer, which is known as the Chern number or Chern index of the surface. This quantization of the Berry flux is known as the Chern theorem, and the integer C is a topological invariant or topological index attached to the manifold of states defined over the surface. The Chern number is a measure of the topology of the manifold, which means it does not depend on the specific details of the system but only on the global structure of the manifold [4].

$$\oint_S \Omega \cdot dS = 2\pi C \quad (2.4)$$

2.3.2 Numerical implementation of Berry phase methodology for identifying topological materials

This section was adapted from [5].

The Z2Pack software package, developed by Dominik Gresch et al. [5], is a method for calculating topological invariants in materials at all levels of modeling, from continuous $\mathbf{k} \cdot \mathbf{p}$ models to tight-binding models and *ab initio* calculations. The method is based on the concept of hybrid Wannier functions (HWF), and the flow of HWF charge centers reveals the nontrivial topological invariant. This technique can be applied to topological insulators and semimetals as well.

The average position of a set of Wannier functions in the home unit cell is called the Wannier charge center (WCC). Gresch et al. [5] used a 1D representation of WCCs in terms of Berry potential to compute the hybrid WCCs. The hybrid WCCs can be considered the WCCs of a 1D system coupled to external parameters (k_x, k_y) . By tracking these hybrid WCCs, the Chern number, a topological invariant of band structures, can be obtained [5].

$$C_\gamma = \frac{1}{2\pi} \int_{BZ} d^2k \operatorname{Tr}[F_\gamma] = \frac{1}{2\pi} \int_{BZ} d^2k \operatorname{Tr}[\Omega_\gamma], \quad (2.5)$$

For an isolated band or set of bands, the Chern number in a 2D or 2D cross-section surface of the 3D Brillouin zone (BZ) can be defined as the integral over the BZ of the Berry curvature.

Gresch et al. [5] also defined the Chern number in terms of hybrid WCCs, which can be used to find the chirality of the Weyl point on any closed 2D manifold surface of the BZ. To compute the chirality of the Weyl point, they used the Wilson loop method, which involves discretizing a closed sphere around the Weyl point into small 2D loops, computing the hybrid WCC for each loop, and the Chern number is [43]

$$C = \frac{1}{a_x} (\sum_n \bar{x}_n(k_y = 2\pi) - \sum_n \bar{x}_n(k_y = 0)) \quad (2.6)$$

here, $\bar{x}_n(k_y)$ is the WCCs which is a function of k_y , and $k_y \in [0, 2\pi]$

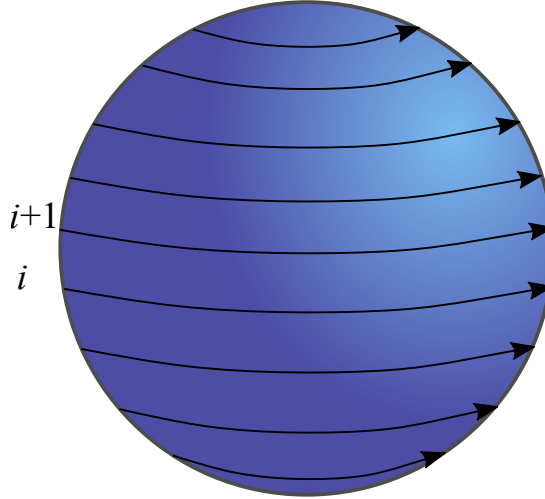


FIGURE 2.3: Loops around the sphere on which WCC are computed. Each loop circles the sphere in mathematically positive direction at a constant azimuthal angle θ . The loops go from the south pole ($\theta = -\pi$) to the north pole ($\theta = 0$). Reprint with permission from [5], copyright 2017 American Physical Society.

Currently several groups investigating in the field of topological materials, and hence, the development of these packages is also increasing. Apart from `Z2Pack`, mentioned in the previous section, there is one more software package called `WannierTools` [44] based on a tight-binding approach. The algorithm to finding the chirality of the Weyl node in this package is similar to the `Z2Pack`. However, both the software packages are used to characterize the Weyl semimetals but the procedure defined in those packages required `Wannier90` to construct the WCCs by using the list of nearest neighbour k points generated by `Wannier90`. Additionally, these packages does not support the full

potential all electron code such as WIEN2k. Therefore, there is a necessary to implement a code which does not required to compute the WCCs and supports full potential all electron code like WIEN2k. These implementations could improve the efficiency of the characterization of Weyl points.

2.4 Topological kagome materials

The kagome lattice is a corner-sharing triangular lattice as shown in Fig. 2.4(a), which is described by using three lattice vectors [45]. Kagome lattice based materials often show geometrical frustration, which refers to the phenomena where magnetic spins are arranged in triangular crystal lattices so that no ordered state can be possible to satisfy the nearest-neighbor interactions. The Hamiltonian for kagome lattice is [45]

$$H_k = \begin{pmatrix} 0 & 2tc_1 & 2tc_2 \\ 2tc_1 & 0 & 2tc_{12} \\ 2tc_2 & 2tc_{12} & 0 \end{pmatrix}, \quad (2.7)$$

where t is the hopping parameter, $c_i = \cos \frac{1}{2}\theta_i$ and $c_{ij} = \cos \frac{1}{2}(\theta_i - \theta_j)$. The eigen values are [45]

$$E_{1,2} = -t \pm t\sqrt{3 + 2\cos\theta_1 + 2\cos\theta_2 + 2\cos(\theta_1 - \theta_2)} \quad (2.8)$$

and

$$E_3 = +2t. \quad (2.9)$$

The parallelogram of $\mathcal{N} \times \mathcal{N}$ unit cells is wrapped onto the torus in Fig. 2.4(b) [46]. Thus, for $t = -1$ the lower flat-band with energies $E_3 = -2t$, a middle band with $E_2 \in [-2t, +t]$, and the upper band $E_1 \in [+t, +4t]$ are shown in Fig. 2.4(c),(d).

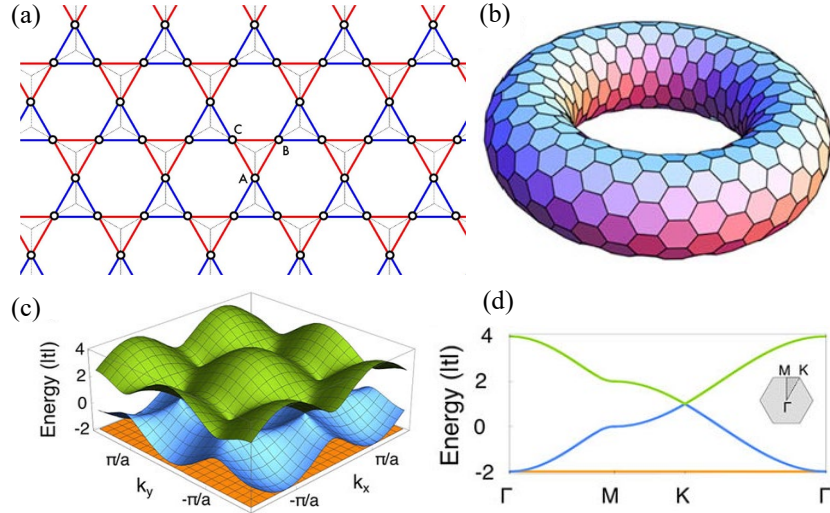


FIGURE 2.4: (a) The Kagome lattice, which is a triangular Bravais lattice with a three element basis (A,B,C). The Kagome lattice is the line graph of a honeycomb lattice [45], (b) Schematic hexagonal unit cells under periodic boundary conditions, (c) The band structure of the kagome lattice for $t=-1$. The flat band at -2 is shown in orange, and the two dispersive graphene-like bands above it are shown in blue and green. The middle band touches the flat band at $k=0$, (d) Line cut through the band structure along a path through the first Brillouin zone shown in the inset. The Fermi energy is at the crossing point of blue and the green band. Reprint with permission from [46], copyright 2020 Springer Nature.

Recently, theoretical study have demonstrated that several systems with flat bands in the absence of magnetic fields show quantum Hall physics [47]. As shown in Fig. 2.4(c),(d), the kagome lattice has both a flat band and Dirac cone-like structure, which strongly agrees with the fact that it exhibits the quantum Hall physics without any applied magnetic field [47].

Thus far, we have addressed the evolution of the linear band structure crossings in kagome-based lattices. In the following section, we will discuss the existing research on these topological kagome materials.

2.4.1 Weyl points in the magnetic Weyl semimetal $\text{Co}_3\text{Sn}_2\text{S}_2$

Qiunan et al. [48] recently study the new ferromagnetic Weyl semimetal (WSM) $\text{Co}_2\text{Sn}_2\text{S}_2$ and $\text{Co}_2\text{Sn}_2\text{Se}_2$ [48], where they have studied the topological Fermi arc states in both of the materials on a cleaved surface. In Fig. 2.5 the results of band structure

and predicted Weyl points are shown. Both $\text{Co}_2\text{Sn}_2\text{S}_2$ and $\text{Co}_2\text{Sn}_2\text{Se}_2$ exhibits a rhombohedral lattice structure with the space group R-3m (No. 166) [48]. The structure can be seen as a 2D lattice stacked along the z-direction, as shown in Fig. 2.5(a). The Co atoms form a kagome lattice in the xy plane, with their magnetic moment aligned along the z-direction in Fig. 2.5(b) and therefore they do not have any frustrated magnetism. These kagome lattice layers are sandwiched between neighboring S or Se layers and are connected through another Sn layer in the z-direction. The electronic structure of $\text{Co}_3\text{Sn}_2\text{S}_2$ is shown in Fig. 2.5(c), where they found the material exhibits the half-metallic band structure, where the spin-up channel crosses the Fermi level E_F and therefore has metallic character, while the spin-down channel is insulating, with a band-gap of 0.35 eV. They also have found the linear band crossings of spin-up states. Because of inversion as well as C_{3z} rotation symmetries, there are a total of six nodal rings in the whole BZ, as indicated in Fig. 2.5(d),(e). Moreover, when SOC is taken into consideration, the nodal ring becomes gaped out, and one pair of linear crossings is preserved in the form of Weyl points with opposite topological charges of Chern numbers +1 and -1. Generally, the Weyl points do not present at the high-symmetry k path. Therefore, in irreducible BZ of $\text{Co}_3\text{Sn}_2\text{S}_2$ and $\text{Co}_3\text{Sn}_2\text{S}_2$ the Weyl point present near $(0.313, -0.0866, -0.0866)$ and $(-0.287, 0.106, 0.106)$ in the fraction coordinate of the primitive cell. The other five Weyl points can be obtained by inversion and C_{3z} rotation symmetry. In the end, the Weyl points of $\text{Co}_3\text{Sn}_2\text{S}_2$ and $\text{Co}_3\text{Sn}_2\text{Se}_2$ will lie 60 and 110 meV above E_F . Hence, electron doping is preferred for detecting Weyl-point-dominated properties [48].

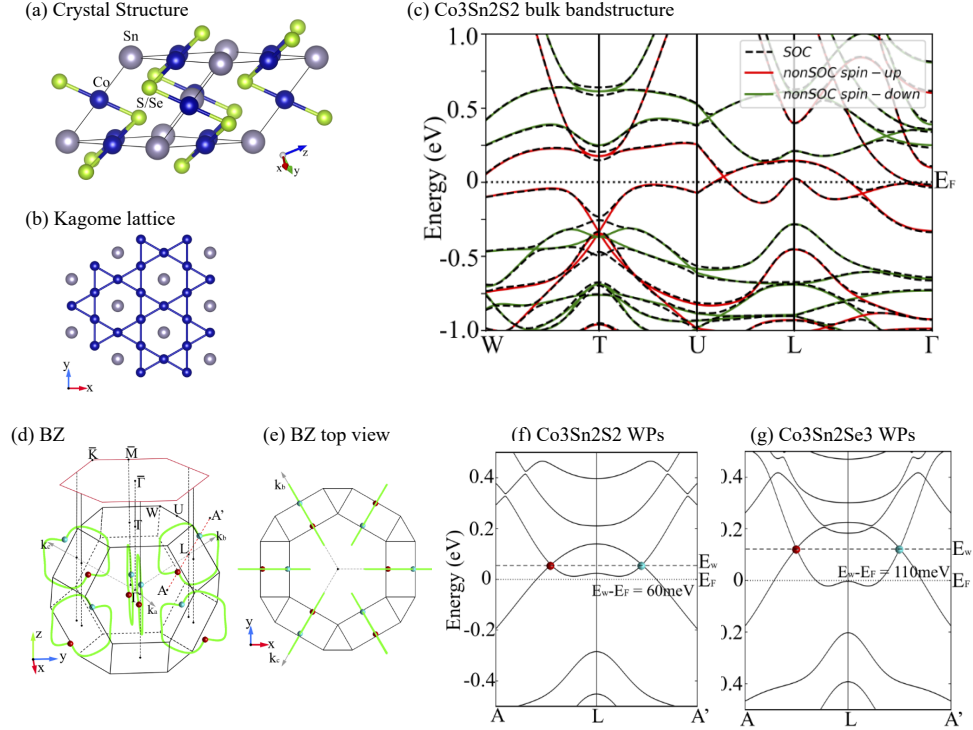


FIGURE 2.5: (a) Rhombohedral lattice structure of $\text{Co}_3\text{Sn}_2\text{S}_2$ and $\text{Co}_3\text{Sn}_2\text{Se}_2$, which exhibit a layered lattice structure in the xy plane. (b) The kagome lattice structure of Co atoms in the xy plane. (c) Band structures of $\text{Co}_3\text{Sn}_2\text{S}_2$, with (black dashed lines) and without (red solid lines for spin up and green solid lines for spin down) SOC. (d) Location of the Weyl points (red and blue represent opposite chiralities) and nodal lines (green) in the 3D Brillouin zone (BZ) and the 2D BZ projected in the (001) direction. (e) Top view along the z direction of BZ with nodal lines and Weyl points. (f) and (g) Energy dispersion along the k path crossing a pair of Weyl points located on the same nodal line for $\text{Co}_3\text{Sn}_2\text{S}_2$ and $\text{Co}_3\text{Sn}_2\text{Se}_2$, respectively. The Fermi level and energy of the Weyl points are labeled E_F and E_W , respectively. Reprint with permission from [48], copyright 2018 by the American Physical Society.

2.4.2 Anomalous Hall effect in $\text{Co}_3\text{Sn}_2\text{S}_2$

Giant anomalous Hall effect is observed in the magnetic Weyl semimetal with broken time-reversal symmetry $\text{Co}_3\text{Sn}_2\text{S}_2$ [21]. The intrinsic anomalous Hall conductivity (AHC) is determined by the integral of the Berry curvature in the whole BZ by using the Kubo formula approach in the linear response and clean limit [21]:

$$\sigma_{yx}^z(E_F) = e^2 \hbar \left(\frac{1}{2\pi} \right)^3 \int_k dk \sum_{E(n,k) < E_F} f(n,k) \Omega_{n,yx}^z(k), \quad (2.10)$$

$$\Omega_{n,yx}^z(k) = \text{Im} \sum_{n' \neq n} \frac{\langle u(n,k) | \hat{v}_y | u(n',k) \rangle \langle u(n',k) | \hat{v}_x | u(n,k) \rangle - (x \leftrightarrow y)}{(E(n,k) - E(n',k))^2}, \quad (2.11)$$

where $f(n, \mathbf{k})$ is the Fermi-Dirac distribution, $E(n, \mathbf{k})$ is the eigenvalue of the n th eigenstate of $|u(n, \mathbf{k})\rangle$ at \mathbf{k} point, and $v_{x(y)} = \frac{1}{\hbar} \frac{\partial H(\mathbf{k})}{\partial k_{x(y)}}$ is the velocity operator [21].

The reason why $\text{Co}_3\text{Sn}_2\text{S}_2$ shows the giant anomalous Hall effect is the large Berry curvature. The Berry curvature contribution, which is dominated by the Weyl nodes, is shown in Fig. 2.6. In addition to a large AHC, they also found the magnetic Weyl semimetal shows a temperature-dependent giant anomalous Hall angle (AHA) characterized by the ratio of σ_H^A/σ (in Fig. 2.7(a)). The ratio first increases with an increase in temperature from 5.6% at 2K, to reach a maximum of around 20% at 120K. After the Curie temperature ($T_C = 175\text{K}$) the ratio again decreases. In Fig. 2.7(b)), it is clearly shown that AHA is approximately 20% in the temperature range from 75 to 175K irrespective of the magnetic field magnitudes. They also have compared the AHA of $\text{Co}_3\text{Sn}_2\text{S}_2$ to the previously reported values, and it is shown that the material $\text{Co}_3\text{Sn}_2\text{S}_2$ dominates because of the large Berry curvature contribution around the Weyl points. These results shows that the non-trivial kagome-lattice $\text{Co}_3\text{Sn}_2\text{S}_2$ possesses both large AHA and AHC simultaneously at zero external magnetic field, which makes this system unusual among the known AHE materials.

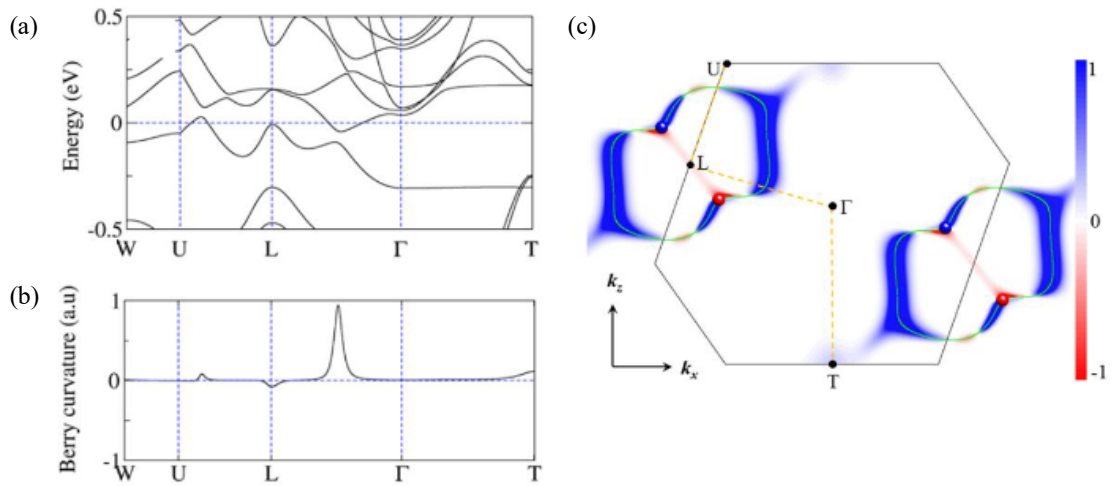


FIGURE 2.6: (a) SOC electronic band structure, and the Fermi energy is at 0eV. (b) Berry curvature of $\text{Co}_3\text{Sn}_2\text{S}_2$ along the high symmetry paths for the valance band at crossing. (c) Berry curvature distribution in $k_y = 0$ plane. Reprint with permission from [21], copyright 2018 Springer Nature.

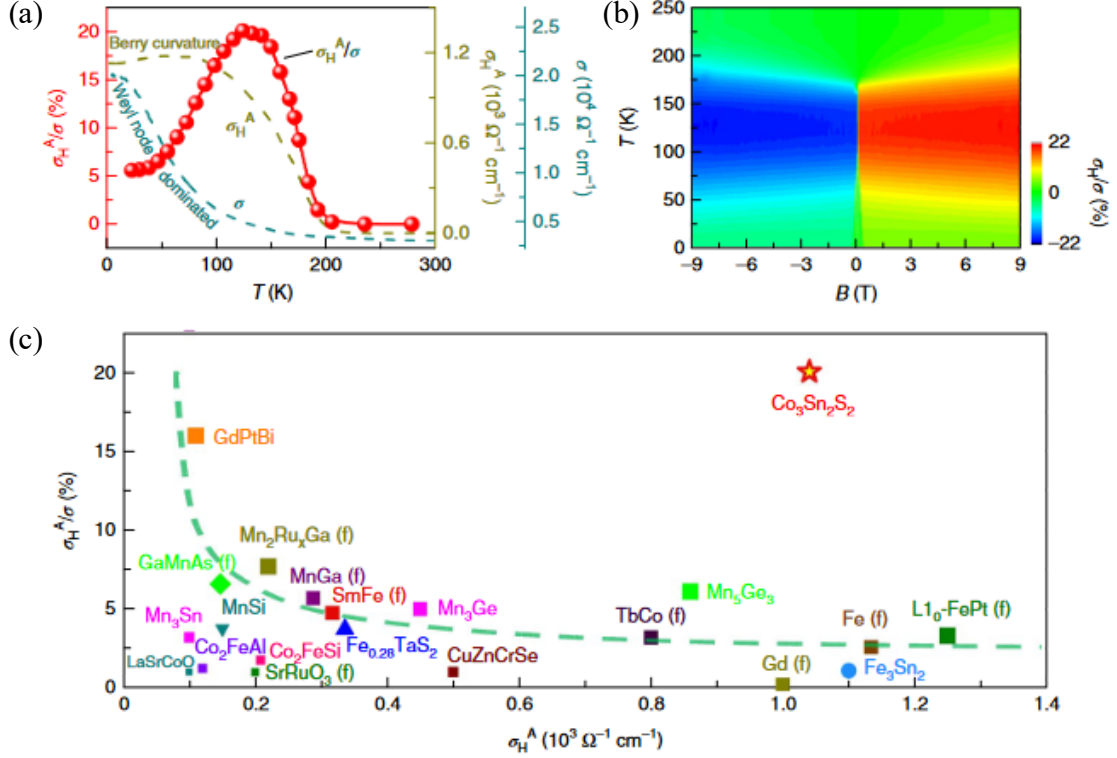


FIGURE 2.7: (a) Temperature dependence of the anomalous Hall conductivity (σ_H^A), the charge conductivity (σ) and the anomalous Hall ratio (σ_H^A/σ) at zero magnetic field. (b) Contour plots of the Hall angle in the B - T space. (c) Comparison of σ_H^A -dependent anomalous Hall angle results and previously reported data for other AHE materials. Reprint with permission from [21], copyright 2018 Springer Nature.

2.5 Formability of Kagome lattice based materials

This section will discuss the structural stability of Co-based kagome lattice or shandite alloys, $\text{Co}_3\text{MM}'\text{X}_2$ ($M/M' = \text{Ge}, \text{Sn}, \text{Pb}$; $\text{X} = \text{S}, \text{Se}, \text{Te}$) studied by Luo *et al.* [49]. They have investigated the topological properties and the thermodynamic stability of these alloys. To design the alloys global structure search approach has been used based on the particle swarm optimization (PSO) algorithm implemented in the software Crystal Structure Analysis by Particle Swarm Optimization (CALYPSO) code [50]. They have discovered the structural tolerance factor below which the kagome lattice-based structure becomes unstable. Moreover, they have determined that $\text{Co}_3(\text{SnPb})\text{S}_2$ alloys can be three-dimensional quantum anomalous Hall metals (QAHMs), that means depending on

the relative positions of Sn and Pb, the Weyl points are present in the $\text{Co}_3(\text{PbSn})\text{S}_2$ but no Weyl points for $\text{Co}_3(\text{SnPb})\text{S}_2$.

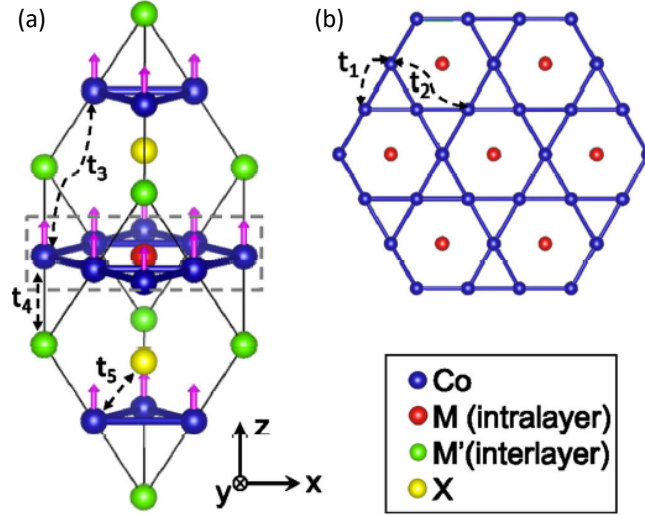


FIGURE 2.8: (a) The crystal structure of shandite $\text{Co}_3\text{MM}'\text{X}_2$ (the pink arrows represent the orientation of spin). (b) The Kagome plane embedded in the shandite structure (highlighted by the dotted gray line in a). The tight-binding hopping parameters t_1 - t_5 . Reprint with permission from [49], copyright 2021 Springer Nature open access article distributed under the terms of the Creative Commons CC BY license.

Crystal structure and the magnetic ground state are shown in Fig. 2.8(a). It is shown in the figure that the Co atoms form the kagome lattice enclosed by the grey rectangle in Fig. 2.8 and projected on kagome lattice as shown in Fig. 2.8. Metal atoms M and M' are occupied both in-plane and out of plane (between the kagome lattice) sites. Further, by using the PSO method, they have studied all the possible structures and found the stable and metastable crystal phases of $\text{Co}_3\text{MM}'\text{X}_2$ as shown in Fig. 2.9. The crystal structures are color-coded, and the one listed first is the most stable configuration. The frequency indicates the number of times the structure is identified. The compounds $\text{Co}_3\text{Sn}_2\text{S}_2$, $\text{Co}_3\text{Pb}_2\text{S}_2$, $\text{Co}_3\text{Sn}_2\text{Se}_2$, $\text{Co}_3\text{Sn}_2\text{S}_2$, and $\text{Co}_3\text{SnPbS}_2$ have the shandite structure (the space group 166) as shown in Fig. 2.9 represented by red bar. On the other hand, $\text{Co}_3\text{Ge}_2\text{Se}_2$ and $\text{Co}_3\text{M}_2\text{Te}_2$ structures are unstable with respect to the structure tolerance factor (s) [49],

$$s = \frac{r(M)}{r(X)} \quad (2.12)$$

where $r(M)$ and $r(X)$ is radius of metal and chalcogen respectively. From Fig. 2.9, the compounds with large $s \geq 1.5$ adopt shandite stable structure otherwise unstable.

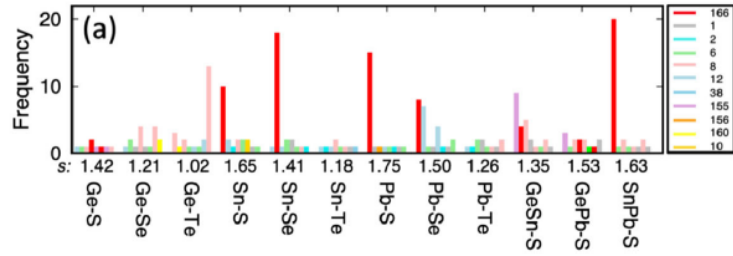


FIGURE 2.9: The low-energy structures for Co-based materials (Co-M-X or Co-MM²-X), where the crystal structures are color coded and arranged by the energy hierarchy for a given composition, i.e., the one listed first is the most stable configuration. The red bars represent the shandite structure (No. 166). The vertical axis represents the emergent frequency of different structures from the PSO simulation. Reprint with permission from [49], copyright 2021 Springer Nature open access article distributed under the terms of the Creative Commons CC BY license.

In conclusion, Luo et al. studied the structural stability of Co-based shandite structures where they have explored the different alloys by replacing metal atoms M/M' and chalcogen X in the Co₃MM' configuration. Further, they have discovered the structure stability descriptor or tolerance factor for shandite structures. However, there is some gap. First, they have focused only on Cobalt-based shandite structure, limiting the search for new potential alloy. Second, they have not studied the stability criteria with energy convex Hull diagram. For example, they found Co₃PbSnS₂ is a stable structure, but there is no comment on the stability of Co₃PbSnS₂ concerning the binary structures Co-Pb, Co-Sn, Co-S.

Chapter 3

Computational method

Author contribution:

The explanation in this chapter was adapted from the two textbooks:

1. Materials Modelling using Density Functional Theory [6], and
2. Electronic Structure Basic Theory and Practical Methods [7].

With significant breakthroughs in fundamental theory, novel algorithms, and computational methodologies, the science of electronic structure is at a crucial juncture. Physicists, chemists, and materials scientists can now get fresh insights into crucial problems in physics, chemistry, and materials science by determining numerous material properties directly from the fundamental electron equations. Electronic structure simulations are increasingly being utilized by both experimentalists and theorists in order to comprehend the characteristic features of matter and make accurate predictions for genuine materials and experimentally observable phenomena [7].

Materials modeling is the application of mathematical models to predict and quantify material properties, including finite element approaches and atomic-scale simulations. Solving the Schrodinger equation for electrons in a potential energy field is the basis for these simulations. This equation is applied to characterize the behavior of electrons in sub-nanometer simulations of atoms. Due to the atomistic character of the investigated systems, the simulations are "ab initio," which means they are based on first principles. Quantum mechanics' fundamental equation, the Schrodinger equation, defines the stationary states of an electron in a given potential energy field $V(r)$ (Ch.2, pg. 20)[6]

$$\left[\frac{\mathbf{p}^2}{2m_e} + \mathbf{V}(r) \right] \psi(r) = E\psi(r), \quad (3.1)$$

where, $\mathbf{p} = -i\hbar\nabla$ is the momentum operator, m_e is the mass of the electron, and E is the energy eigen value for the stationary state described by the wave function ψ .

By precisely characterizing systems with a large number of electrons and nuclei, the statement explains how to construct a realistic and workable theory of materials. The method employs a many-body wavefunction, designated Ψ , that depends on the positions of each electron and nucleus. This wavefunction is employed to modify (3.1), which explains the behavior of a single electron in a static potential (Ch.2, pg. 25)[6]

$$\left[\underbrace{-\sum_i \frac{\nabla_i^2}{2} - \sum_I \frac{\nabla_I^2}{2M_I}}_{\text{Kinetic Energy}} - \underbrace{\sum_{i,I} \frac{Z_I}{|\mathbf{r}_i - \mathbf{R}_I|}}_{\text{Coulomb attraction}} + \underbrace{\frac{1}{2} \sum_{i \neq j} \frac{1}{|\mathbf{r}_i - \mathbf{r}_j|} + \frac{1}{2} \sum_{I \neq J} \frac{Z_I Z_J}{|\mathbf{R}_I - \mathbf{R}_J|}}_{\text{Coulomb Repulsion}} \right] \Psi = E_{tot} \Psi, \quad (3.2)$$

where, i and I representation used for the electron and the nuclei respectively.

The modified equation, (3.2), describes the many-body Schrodinger equation in terms of Hartree atomic units ($E_{Hartree} = \frac{\hbar^2}{m_e}$) and is utilized in first-principles material modeling. The equation displays the kinetic energy terms for each electron and nucleus, as well as the Coulomb attraction and repulsion terms between the atoms. Atomic numbers and atomic masses are the only external parameters required for this procedure.

A "many-body wavefunction" (3.3) is used to accurately represent the behaviour of a large number of electrons and nuclei in a material system. This renders the theory of materials more practical and realistic (Ch.2, pg. 21)[6]

$$\Psi = \Psi(\mathbf{r}_1, \mathbf{r}_2, \dots, \mathbf{r}_N; \mathbf{R}_1, \mathbf{R}_1, \dots, \mathbf{R}_M). \quad (3.3)$$

3.1 Density Functional Theory

As described in [7] at pg. 130, in 1927, Thomas and Fermi created the Thomas-Fermi theory, which was the first density-functional theory of quantum systems. This method, on the other hand, is not good for simulating modern electronic structures because it doesn't take into account electron exchange or correlation. Later, Dirac developed the local approximation to electron exchange. This allowed the energy to be applied to electrons at an outside potential. The appeal of density functional theory is not to be confused with the Thomas-Fermi method. It cannot be used for electrons in matter because it omits out essential parts of physics, chemistry, and physics [7].

3.1.1 The Hohenberg–Kohn Theorems

The theoretical framework that describes the electronic structure of a quantum mechanical system with electron density distribution ($n_0(r)$) is called density functional theory (DFT), as illustrated in Fig 3.1. $n_0(r)$ is a scalar quantity that can be used to calculate the ground and excited states of a system [7].

Mermin, Hohenberg, and Kohn first introduced the concept. However, it is difficult to create functionals that are suitable for multi-electron systems. Kohn and Sham's auxiliary system approach allows for the construction of functionals that can be used in real systems with many electrons [7].

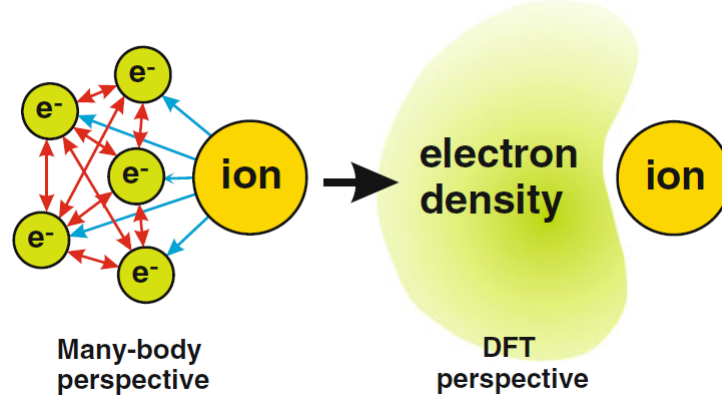


FIGURE 3.1: Illustration of the core principle of a density functional theory to describe individual electron mutual interactions and their interactions with ions by an electron ensemble described just by its density. Reprint with permission from [51], copyright 2015 Springer-Verlag Berlin Heidelberg .

Hohenberg and Kohn use density functional theory as an *exact many-body theory*. The formulation can be used to formulate any system of interacting particles in an external potential $V_{ext}(r)$ with a hamiltonian in Hartree atomic units (Ch.6, pg. 132) [7]

$$\hat{H} = -\frac{1}{2} \sum_i \nabla_i^2 + \sum_i V_{ext}(\mathbf{r}_i) + \frac{1}{2} \sum_{i \neq j} \frac{e^2}{|\mathbf{r}_i - \mathbf{r}_j|}. \quad (3.4)$$

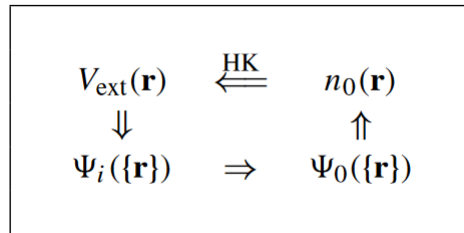


FIGURE 3.2: Hohenberg–Kohn diagram. The smaller arrows represent the standard solution of the Schrödinger equation, where the potential $V_{ext}(r)$ defines all system states $\Psi_i(\mathbf{r})$, including the ground state $\Psi_0(\mathbf{r})$ and ground-state density $n_0(\mathbf{r})$. The Hohenberg–Kohn theorem completes the circle with the long "HK" arrow. Reprint with permission from [7], copyright 2020 Cambridge University Press.

The theory of DFT is based on two theorems that Hohenberg and Kohn were the

first to prove. These theorems examine the relationship between the density of particles $n_0(\mathbf{r})$, their Hamiltonian, and external potential ($V_{ext}(\mathbf{r})$) in a particle-based system [7].

The first theorem says that the ground-state particle density $n_0(\mathbf{r})$ in the external potential $V_{ext}(\mathbf{r})$, is the only factor that determines the value of the potential $V_{ext}(\mathbf{r})$. The theorem also asserts that many-body wavefunctions with a constant change in energy can describe all excited states and ground states. $n_0(\mathbf{r})$ is the basis for the Hamiltonian. Knowing the $n_0(\mathbf{r})$ of the system lets us precisely predict its characteristics. Fig 3.2 is an illustration of the relationships that Hohenberg and Kohn established between the variables [7].

The second theorem states that it is possible to construct a universal functional for the energy $E[n]$ in terms of the density $n(\mathbf{r})$ that is applicable to any external potential $V_{ext}(\mathbf{r})$. This implies that the energy of the ground state of the system could be expressed as a function of its density. It is only dependent upon the electron density as well as external potential [7].

According to this theorem, the exact ground-state energy of the system is the global lowest value of this functional for any given $V_{ext}(\mathbf{r})$, and the density $n(\mathbf{r})$ that minimizes the functional is the exact ground-state density $n_0(\mathbf{r})$. The functional can be reduced in relation to density in order to obtain the exact ground-state density and energy. The theorem also has an additional consequence: By using only the functional $E[n]$, it is possible to determine the exact ground-state energy, or density, of the system. Since the functional is diminished in relation to density, it is possible to estimate the ground-state energy or density. This is a great way to determine the electronic property of the system [7].

3.1.2 The Kohn–Sham Auxiliary System

In density functional theory, the Kohn-Sham approach simplifies the calculation of the ground state energy and density for many-body systems obeying the hamiltonian Eq.(3.2) with interacting particles. This strategy replaces a complex Hamiltonian system with a simpler auxiliary system (Fig 3.3) that can be solved more quickly. The strategy aims to find a distinct system whose ground state density is identical to that of the original system without interaction (independent-particle approximation) and is therefore simpler to solve. Therefore, in rest of the chapter the wavefunction has decoupled coordinates of electrons. Kohn and Sham hypothesised that this could be achieved by including exchange-correlation effects into an effective potential resulting from particle interactions [7].

For non-interacting systems, Kohn-technique Sham’s employs the ground state density to generate a set of independent-particle equations. These equations can be solved numerically, and a density-specific exchange correlation functional can be applied to incorporate all many-body effects. This exchange correlation functional accurately accounts for the difficult-to-calculate electron-electron interactions in the system. The precision with which the Kohn-Sham equations may compute the ground state density and energy of an interacting system is constrained by the accuracy of exchange correlation functional approximations. The Kohn-Sham approach has shown to be a useful tool in density functional theory, allowing for the calculation of properties of vast, complicated systems that would otherwise need an excessive amount of computing to evaluate using more conventional methods [7].

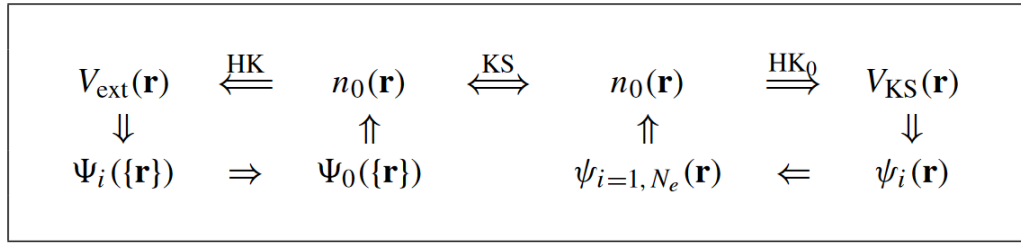


FIGURE 3.3: Hohenberg–Kohn applied to the noninteracting problem is HK_0 . The arrow labeled KS connects any location to any other point between the many-body and auxiliary independent-particle systems in both directions. Thus, the independent-particle Kohn–Sham problem dictates all features of the complete many-body system. Reprint with permission from [7], copyright 2020 Cambridge University Press.

The Kohn-Sham method involves two assumptions for the development of an auxiliary system. Firstly, it asserts that a non-interacting particle system can accurately reflect the ground state density of a real system, despite the absence of formal evidence to support this claim. This idea is referred to as "non-interacting-V representability," and Fig 3.3 illustrates its relationship to real and auxiliary systems. Second, the Kohn-Sham technique assumes that an auxiliary Hamiltonian possesses a standard kinetic operator and an effective local potential $V_{ef}^\sigma(\mathbf{r})$ that act on a spin (σ) carrying electron at a particular location \mathbf{r} [7].

Actual calculations are carried out on the auxiliary independent-particle system specified by the auxiliary hamiltonian \hat{H}_{aux}^σ [7] (This section is adapted from Ch. 7, pg.147-149 [7])

$$\hat{H}_{aux}^\sigma = \frac{-1}{2}\nabla^2 + V^\sigma(\mathbf{r}). \quad (3.5)$$

To define functionals for a range of densities, the expressions must hold true for all $V^\sigma(\mathbf{r})$ within a certain range. For a system of $N = N^\uparrow + N^\downarrow$ electrons obeying this hamiltonian, the ground state consists of one electron in each of the N^σ orbitals $\psi_i^\sigma(\mathbf{r})$ with the lowest eigenvalues ϵ_i^σ of the hamiltonian Eq.(3.5). Sums of squares of orbitals for each spin determine the density of the auxiliary system [7]

$$n(\mathbf{r}) = \sum_{\sigma} n(\mathbf{r}, \sigma) = \sum_{\sigma} \sum_{i=1}^{N^\sigma} |\psi_i^\sigma(\mathbf{r})|^2, \quad (3.6)$$

the independent-particle kinetic energy T_s and the classical Coulomb interaction energy of the electron density $n(\mathbf{r})$ interacting with itself can be expressed as [7]

$$T_s = \frac{-1}{2} \sum_{\sigma} \sum_{i=1}^{N^\sigma} \langle \psi_i^\sigma | \nabla^2 | \psi_i^\sigma \rangle = \frac{1}{2} \sum_{\sigma} \sum_{i=1}^{N^\sigma} \int d^3r |\nabla \psi_i^\sigma(\mathbf{r})|^2, \quad (3.7)$$

$$E_{Hartree}[n] = \frac{1}{2} \int d^3r d^3r' \frac{n(\mathbf{r})n(\mathbf{r}')}{|\mathbf{r} - \mathbf{r}'|}. \quad (3.8)$$

In order to solve the whole interacting many-body problem, Kohn-Sham propose the formula for the ground-state energy functional [7]

$$E_{KS} = T_s + \int d\mathbf{r} V_{ext}(\mathbf{r})n(\mathbf{r}) + E_{Hartree}[n] + E_{II} + E_{XC}[n]. \quad (3.9)$$

Here, the external potential of the nuclei or any other fields (assumed spin-independent) is represented by $V_{ext}(\mathbf{r})$. Therefore, a neutral grouping can be formed using the sum of the terms that involve V_{ext} , $E_{Hartree}$, and E_{II} [7]. The independent-particle kinetic energy, denoted by the symbol T_s , is presented explicitly in the form of a functional of the orbitals [7]. Nevertheless, according to the Hohenberg–Kohn arguments, which are applied to the independent-particle hamiltonian Eq.(3.5), T_s must be a unique functional of the density. All many-body effects of exchange and correlation are pooled into the exchange correlation energy E_{XC} , and it is straightforward to demonstrate that E_{XC} is functional by employing the Hohenberg–Kohn functional [7]

$$E_{XC}[n] = \langle \hat{T} \rangle - T_s[n] + \langle \hat{V}_{int} \rangle - E_{Hartree}[n]. \quad (3.10)$$

The functional $[n]$ is dependent on both position and spin $n(\mathbf{r}, \sigma)$, suggesting that solving the Kohn-Sham equations for independent particles would yield exact ground state energy and density if we knew the universal functional E_{XC} . Instead, Kohn-Sham

uses an approximation of exchange correlation energy $E_{xc}[n]$, to calculate the ground state properties in a multibody electron system [7].

The solution for the ground state of the Kohn–Sham auxiliary system can be seen as a minimization with respect to either $n(\mathbf{r}, \sigma)$ or $V_{eff}^\sigma(\mathbf{r})$. This is called the *Kohn–Sham variational equations* [7]

$$\frac{\delta E_{KS}}{\delta \psi_i^{\sigma*}(\mathbf{r})} = \frac{\delta T_s}{\delta \psi_i^{\sigma*}(\mathbf{r})} + \left[\frac{\delta E_{ext}}{\delta n(\mathbf{r}, \sigma)} + \frac{\delta E_{Hartree}}{\delta n(\mathbf{r}, \sigma)} + \frac{\delta E_{XC}}{\delta n(\mathbf{r}, \sigma)} \right] \frac{\delta n(\mathbf{r}, \sigma)}{\delta \psi_i^{\sigma*}(\mathbf{r})} = 0, \quad (3.11)$$

$$\left\langle \psi_i^\sigma \left| \psi_j^{\sigma'} \right. \right\rangle = \delta_{i,j} \delta_{\sigma,\sigma'}. \text{ (Orthonormalization)} \quad (3.12)$$

From Eq.(3.6) and Eq.(3.7) this becomes the Kohn–Sham Schrödinger-like equations [7]:

$$(H_{KS}^\sigma - \epsilon_i^\sigma) \psi_i^\sigma(\mathbf{r}) = 0, \quad (3.13)$$

where ϵ_i are the eigenvalues, and H_{KS} is the effective hamiltonian

$$H_{KS}^\sigma(\mathbf{r}) = \frac{-1}{2} \nabla^2 + V_{KS}^\sigma(\mathbf{r}), \quad (3.14)$$

Here,

$$\begin{aligned} V_{KS}^\sigma(\mathbf{r}) &= V_{ext}(\mathbf{r}) + \frac{\delta E_{Hartree}}{\delta n(\mathbf{r}, \sigma)} + \frac{\delta E_{XC}}{\delta n(\mathbf{r}, \sigma)} \\ &= V_{ext}(\mathbf{r}) + V_{Hartree}(\mathbf{r}) + V_{XC}^\sigma(\mathbf{r}). \end{aligned} \quad (3.15)$$

Chapter 4

Characterization of Weyl semimetals using WloopPHI

Author contribution:

Dr. Oleg Rubel conceived the idea. The code was implemented by me and reviewed by Dr. Oleg Rubel. I conducted the main part of the calculations and data analysis. The first draft was written by me and revised by Oleg Rubel (mostly rewritten with figures). Characterization of triple degenerate points including calculations and figures were done by Dr. Oleg Rubel. The project was supervised by Oleg Rubel.

This chapter was published in Computer Physics Communications, 270 (2021), 108147, DOI:10.1016/j.cpc.2021.108147.

Abstract

WloopPHI is a Python code that expands the features of WIEN2k, a full-potential all-electron density functional theory package, by the characterization of Weyl semimetals. It enables the calculation of the chirality (or “monopole charge”) associated with Weyl nodes and nodal lines. The theoretical methodology for the calculation of the chirality is based on an extended Wilson loop method and a Berry phase approach. We validate the code using TaAs, which is a well-characterized Weyl semimetal, both theoretically and experimentally. Afterwards, we applied the method to the characterization of YRh₆Ge₄ and found a set of Weyl points (ca. 0.2 eV below the Fermi energy).

4.1 Introduction

With the help of developments in the field of topological materials [25–29], new phenomena including ultrahigh magnetoresistance [12], chiral anomaly [13–17], the intrinsic anomalous Hall effect [18–22], and unusual Fermi arc surface states [23, 24] have been predicted and discovered. From insulators to metals and semimetals, the range of topological materials has grown [14, 30–32]. Gapless semimetals are a topological subset of Weyl semimetals (WSMs). Topological Fermi arc surface states connecting Weyl nodes with opposing chirality are a characteristic of WSMs [1, 3, 23, 24, 33, 52, 53]. Weyl points develop in materials when a Dirac nodal ring experiences spin-orbit coupling (SOC), breaking either time-reversal or spatial inversion symmetry (but not both) [1–3].

The chirality of Weyl nodes can be characterized as the Berry flux through a closed surface S in reciprocal k space (Fig. 4.1a,b) that surrounds the Weyl node in question [3]

$$\gamma_n = \oint_S (\nabla_{\mathbf{k}} \times \mathbf{A}_n) \cdot d\mathbf{S}. \quad (4.1)$$

Here n is the band index for the lower of the two bands at the crossing (i.e., $n = N$ in Fig. 4.1a) and \mathbf{A}_n is a Berry connection [54]

$$\mathbf{A}_n(\mathbf{k}) = i \langle u_{n\mathbf{k}} | \nabla_{\mathbf{k}} | u_{n\mathbf{k}} \rangle, \quad (4.2)$$

with $u_{n\mathbf{k}}$ being the cell-periodic part of the Bloch wave function $\psi_{n\mathbf{k}}(\mathbf{r}) = u_{n\mathbf{k}}(\mathbf{r})e^{i\mathbf{k}\cdot\mathbf{r}}$, and the term $\nabla_{\mathbf{k}} \times \mathbf{A}_n$ representing the Berry curvature vector field. The topological

properties of a Weyl point are captured by its chirality

$$\chi = \gamma_n/2\pi. \quad (4.3)$$

According to the no-go theorem [55, 56], Weyl points most frequently occur in pairs with opposite chirality or opposite “monopole charge” (± 1). Moreover, bands crossings with larger monopole charge magnitudes such as 2, 3, etc. are also feasible [57]. Even while there is a tendency in the literature [58–60] to refer to “Chern number” as a synonym for the chirality of specific Weyl points, we choose not to do so here. The goal is to prevent confusion with another Chern number that determines an anomalous Hall conductivity and is defined as an integral of the Berry curvature over the entire Brillouin zone and occupied bands (Ref. [4], chap.5).

There are two open-source software programs `WannierTools` [44] and `Z2Pack` [5, 61] provide complete tool-kits for the theoretical characterization of topological materials, including WSMs. Both tools build a small sphere around the target node to assess the chirality of the Weyl point. They follow the evolution (winding) of the total hybrid Wannier charge centres computed on loops as a function of the polar angle to determine the chirality of the enclosed Weyl point. There is, however, a significant distinction between these two programs. Through the use of a tight-binding framework produced by `Wannier90` [62], `WannierTools` offers an indirect characterization of *ab initio* electronic band structure. On the other hand, `Z2Pack` is capable of working at all stages of materials modelling and even directly integrating with *ab initio* calculations [5]. However, `Z2Pack` just needs `Wannier90` to create the list of nearest neighbours (aseedname.nnkp file), which is then used by a first-principles algorithm to determine overlap projections and ultimately the Wannier charge centres (WCC).

Weyl semimetals are characterised using `WloopPHI`, an open-source program, which is presented here. In contrast to `WannierTools`, `WloopPHI` can be used without creating a Wannier Hamiltonian or use `Wannier90` straight from the scratch. Although `Z2Pack` can be run without Wannierization, or from first principles, it needed `Wannier90` to finish the calculations for WCC. `Z2Pack` can interface with a number of plane wave codes, but not fully functional with all-electron codes like `WIEN2k`.

For `WloopPHI`, we propose an alternative methodology to characterize Weyl points and calculate their chirality. Instead of constructing a closed surface S , we select a small open surface S' defined by a closed loop L in reciprocal space (Fig. 4.1c). The Berry

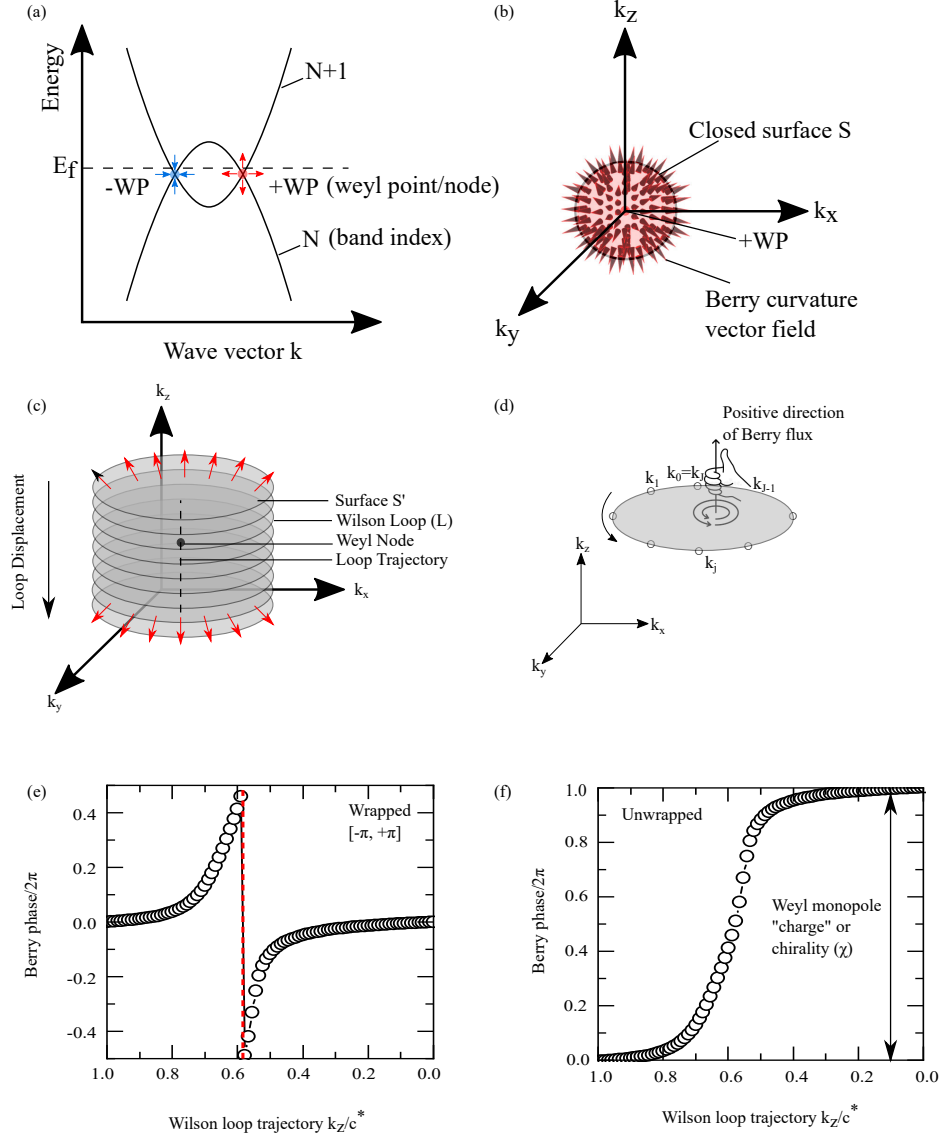


FIGURE 4.1: (a) Weyl nodes of opposite chirality at the intercept of two bands. Arrows indicate the source (red) and sink (blue) of the Berry curvature $\nabla_{\mathbf{k}} \times \mathbf{A}_n$. (b) The node can be viewed as a monopole with a chiral charge (positive node is shown with the chirality $\chi = +1$). The charge is determined by a Berry flux through a closed surface S that encloses the Weyl node. (c) Construction of a series of Wilson loops that enclose one Weyl node. There is a Berry phase ϕ associated with each loop that represents a Berry flux through the surface S' of the loop. (d) Use of a right-hand rule in definition of a positive direction of the Berry flux through the loop. (e) Evolution of Berry phase (wrapped in the range $[-\pi, +\pi]$) as a function of the loop's position along the k_z direction. The discontinuity (marked with an arrow) corresponds to a Weyl point. (f) A finite Berry phase (unwrapped) accumulates as the Wilson loop traverses through the BZ. The accumulated phase represents the chirality $\chi = +1$ of the Weyl point.

flux through this surface can be found using Stokes' theorem

$$\phi_n = \iint_{S'} (\nabla_{\mathbf{k}} \times \mathbf{A}_n) \cdot d\mathbf{S}' = \oint_L \mathbf{A}_n \cdot d\mathbf{k}. \quad (4.4)$$

This method's key benefit is that we do not need to be familiar with the Berry curvature vector field. Furthermore, there are no gauge-fixing conditions needed with our technique. According to King-Smith and Vanderbilt [63], integration of the Berry connection on a complete loop of k points in reciprocal space (Fig. 1d) is well established and is directly implementable in *ab initio* electronic structure programs. We are interested in the changes that occur when the loop travels along a trajectory that encloses a Weyl node in terms of the Berry flux via S' (also known as the Berry phase on the loop) (Fig.1c). The loop trajectory can be selected so that it develops in a direction that is "negative," as determined by the right-hand rule (Fig.1d). Berry curvature vector field flux via the loop S' will be modest while the loop is distant from the Weyl node and progressively grow as the loop approaches the node because Weyl points can either be sources or sinks of the field (Fig.1e). The position of a Weyl node will be indicated by the existence of a discontinuity in the Berry phase. The winding number of the Berry phase along the trajectory of the loop (Fig. 1f) of the enclosed Weyl node(s) is used to express chirality [2]. The benefit of enclosing a Weyl node in a cylindrical shape (as opposed to a spherical surface used in Z2Pack or WannierTools) is that the precise position of the Weyl node along the height of the cylinder need not be known beforehand. The disadvantage is that more computations must be done because more loops must be built to map the height.

We refer to our technique as a "Wilson loop" extension to recognize its relationship to Wilson [64] suggestion that a gauge field be calculated on a closed path. It should not be confused with another Wilson loop approach variation, which is used to calculate the \mathbb{Z}_2 topological invariant and is known as an evolution of WCC [65, 66]. The latter indicates that the Berry phase on a string of k points in the Brillouin zone (BZ) is calculated in one dimension (1D) (analogous to calculation of electronic polarization in solids [63]). The periodicity of the BZ ensures that this one-dimensional string has a closed loop structure. WSMs are subjected to the development of WCCs to uncover their \mathbb{Z}_2 topological invariant [3, 67, 68], although no information on the chirality of specific Weyl points is provided. Soluyanov et al. [58] improved the Wilson-loop and hybrid-Wannier-centers approach for type-II WSMs by building circular Wilson loops on a tiny sphere around a Weyl point to determine its chirality.

We use WIEN2k [69, 70], an all-electron DFT [71, 72] package, as the foundation for putting our strategy into practise. For the purpose of calculating the Berry phase on the Wilson loop, we combine the Wien2wannier [73] and BerryPI codes [74], both of which are implemented in the WIEN2k package. We describe the well-known topological material TaAs [3, 24, 52] in order to validate our methods before examining the Weyl points of the recently found material YRh₆Ge₄ [75–77].

4.2 Method

4.2.1 Chirality of a Weyl point

To evaluate the chirality of Weyl points, we applied the extended Wilson loop approach. In the BZ, a Wilson loop is a random closed k -point route (Fig.1d). Wave functions assessed along this path develop a complete Berry phase $\phi(k)$. Instead of referring to a k point on the loop itself, k in this case denotes a position on the loop’s trajectory. A Weyl point (or points) of interest are encircled by a sequence of parallel Wilson loops that are built in this manner. The winding number of the computed Berry phase $\phi(k)$ along the trajectory is equal to the chirality.

A general expression for the Berry phase on a Wilson loop for a manifold of bands in a range $n_a \dots n_b$ is determined using BerryPI following the numerical method outlined in Ref. [63]

$$\phi_{n_a:n_b} = \text{Im} \left[\ln \prod_{j=0}^{J-1} \det \mathbb{M}_{l \times l}(\mathbf{k}_j, \mathbf{k}_{j+1}) \right]. \quad (4.5)$$

Here, the product index j loops across all k points on the Wilson loop in this case, where \mathbb{M} is the overlap matrix of dimension $l^2 = (1 + n_b - n_a)^2$ (Fig. 4.1d). The overlap integral $\mathbb{M}_{mn}(\mathbf{k}_j, \mathbf{k}_{j+1}) = \langle u_{m\mathbf{k}_j} | u_{n\mathbf{k}_{j+1}} \rangle$ is computed. Wien2wannier carries out the Bloch function’s periodic components between two cells. In order to calculate the Berry phase, just one band needs to be used ($n_a = n_b = N$ or $n_a = n_b = N + 1$, but not both $n_a = N, n_b = N + 1$). It may be advantageous to include a range (e.g., $n_a = 1, n_b = N$) if we want to rule out crossover between bands $N - 1$ and N that could unintentionally fall within the Wilson loop. In the latter scenario, we may reduce the number of semi-core electrons by choosing a suitable bottom band range n_a .

Depending on how the Berry curvature is defined, there are two possible sign conventions for the Berry phase (see Sec. 3.2 in Ref. [4]). According to the convention used in Eq. (4.5), the Berry curvature’s z -axis component is defined mathematically as

$(\nabla_{\mathbf{k}} \times \mathbf{A}_n)_z = \partial_y A_x - \partial_x A_y$, which is also consistent with the right-hand rule. Alternatively, the terms $\partial_\alpha A_\beta$ can be swapped, as seen in Ref. [44], resulting in a sign reversal for both the Berry curvature and the phase in Eq. (4.5). Reversal of the sign for the chirality of Weyl nodes is an effect of the differing sign convention. The characterisation of WSMs is not hampered by the various standards since Fermi arc predictions, which are observables, depend on the polarity difference between Weyl nodes.

A schematic representation of the implemented approach is shown in Figure 4.1c,d. The range of $[-\pi, +\pi]$ encompasses the Berry phases $\phi(k)$ estimated for each Wilson loops along the trajectory (see Fig. 4.1e). A discontinuity in the evolution of the Berry phase along the trajectory will appear if the trajectory has a Weyl point. An inversion of the Berry flux direction on the loop plane going through the Weyl point explains the discontinuity. The number of Weyl points and the number of discontinuities along the loop trajectory are equal. We unwrap $\phi(k)$ (Fig.1f) and analyze the phase difference between the final and initial point on the loop trajectory to determine the chirality χ of each individual Weyl point. The χ is computed as

$$\chi = \frac{1}{2\pi} \text{unwrap}[\phi(k_{\text{fin}}) - \phi(k_{\text{init}})]. \quad (4.6)$$

The definition of the initial and final point implies that the loop evolves along the *negative* direction as defined by the right-hand rule (Fig. 4.1d). The unwrapping is performed by the python `numpy.unwrap` function, which minimizes discontinuities in the array of phases $\phi(k)$ by adding or subtracting a multiple of 2π .

4.2.2 Program implementation

WloopPHI is a python code for *ab initio* calculation of the Berry phase along a series of Wilson loops. It works in a package with WIEN2k, Wien2wannier, and BerryPI. The block diagram is shown in Appendix A. WloopPHI became a part of WIEN2k standard distribution starting with the version 21.1 released on Apr 2021. At the same time, we offer a current development version of WloopPHI via a GitHub repository [78] that captures any work-in-progress and bug fixes prior to the next WIEN2k release.

WloopPHI requires one input file which contains information about the WIEN2k case directory, the number of intermediate Wilson loops on the trajectory, the upper band index N , and the list of k points ($\mathbf{k}_1, \mathbf{k}_2, \dots, \mathbf{k}_{J-1}$, Fig. 4.1d) that compose the Wilson loop in the initial and final parts of the trajectory (intermediate loops will be interpolated).

The execution of the code is done by invoking `WloopPHI` with one argument, which is the Wilson loop input file name (say `Wloop.in`). This argument is mandatory. Optional arguments include: `-sp` which allows spin-polarized calculation, `-orb` which allows for additional orbital potentials (local density approximation + Hubbard U or exact exchange for correlated electrons), and `-p` for parallel calculation (requires `.machines` file as described in the WIEN2k users guide [69])

```
python /path/to/WIEN2k/SRC_BerryPI/BerryPI/WloopPHI.py Wloop.in [-sp] [-orb] [-p]
```

The spin-orbit coupling is activated implicitly. The code generates one output file, `PHI.dat`, and associated figures. The output file contains four columns: The Wilson loop trajectory evolution coordinate k , the computed “raw” Berry phases $\phi(k)$, the Berry phases wrapped in the range $[-\pi, +\pi]$, and the unwrapped Berry phases. The last column contains all the information needed for computing the chirality using Eq. (4.6).

To find the coordinates in the first column, we calculate the distance between the first loop and the last loop and divide it by the specified number of Wilson loops which gives the distance between subsequent Wilson loops along the trajectory, Δk . The Δk is used to find the intermediate points along the evolution direction of the Wilson loop which is identical for all k-points in the Wilson loop

$$\Delta k = \frac{\sqrt{(k_{x_i} - k_{x_f})^2 + (k_{y_i} - k_{y_f})^2 + (k_{z_i} - k_{z_f})^2}}{n_{wl} - 1}, \quad (4.7)$$

where \mathbf{k}_i and \mathbf{k}_f stand for the initial and final coordinates of the first k-point on the Wilson loop, n_{wl} is the number of Wilson loops.

An example output file for TaAs for one Weyl point is given below. For this calculation, the Wilson loop was moved along the k_z direction from $k_z = 1$ to $k_z = 0$ in units of the reciprocal lattice vector c^* . The trajectory contained a total of 91 loops.

# Loop (z)	BerryPhase(BP)	BP(-/+pi wrap)	BP(unwrap)
1.00000	-6.28319	-0.00000	-0.00000
0.98889	0.00712	0.00712	0.00712
0.97778	0.01377	0.01377	0.01377
0.96667	0.02049	0.02049	0.02049
0.95556	0.02738	0.02738	0.02738
0.94444	-6.24853	0.03466	0.03466
0.93333	6.32555	0.04236	0.04236
0.92222	0.05028	0.05028	0.05028

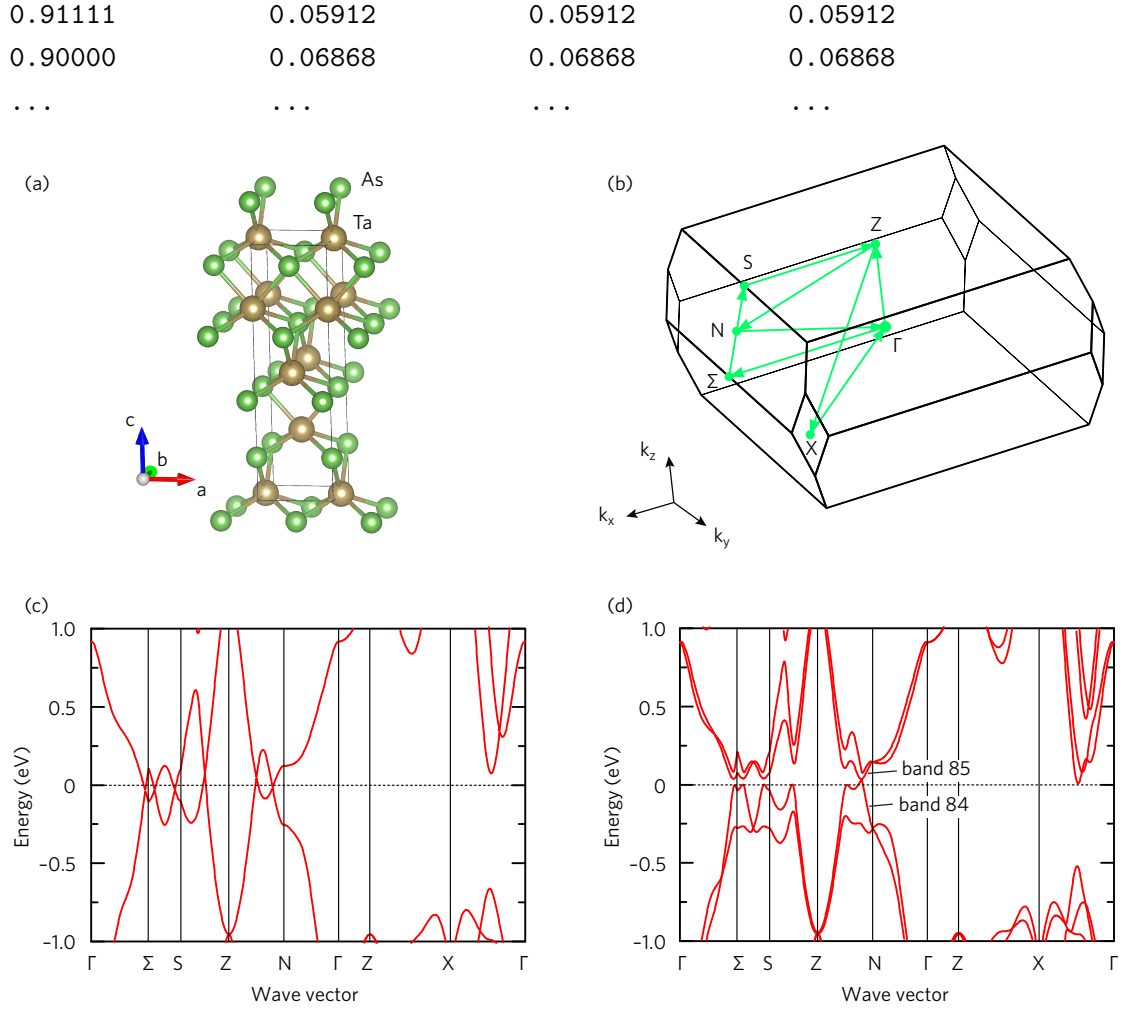


FIGURE 4.2: (a) The crystal structure of TaAs. (b) The bulk Brillouin zone. (c) Band structure calculated with the PBE functional without SOC. Energies are plotted relative to the Fermi energy. (d) Band structure with SOC. The Berry phase calculations include band 84 only.

4.2.3 Sample work flow

Here we present a sample calculation for TaAs using WIEN2k with the Perdew, Burke, and Ernzerhof [79] (PBE) exchange-correlation functional. The steps are as follows:

- Generate the input structure file for TaAs using the `w2web` interface, the `makestruct` utility or from a cif file. The following lattice parameters for TaAs were used: $a = b = 3.436 \text{ \AA}$; $c = 11.640 \text{ \AA}$ and angles $\alpha = \beta = \gamma = 90^\circ$. TaAs crystallizes in a body-centered-tetragonal structure with space group $I4_1md$ (No. 109). The unit

cell contains 2 non-equivalent atoms with fractional coordinates Ta (0, 0, 0.75), and As (0, 0, 0.1677) [3]. The structure of TaAs is shown in Fig. 4.2a.

- Initialize the calculation with PBE, 3% reduction of muffin-tin radii R_{MT} , the product $\min(R_{\text{MT}})K_{\text{max}} = 7$, and 300 k points in the whole BZ.

```
init_lapw -b -vxc 13 -red 3 -rkmax 7 -numk 300
```

- Perform a self-consistent field (SCF) calculation with energy convergence of 10^{-4} Ry, and charge convergence of $10^{-3}e$.

```
run_lapw -ec 0.0001 -cc 0.001
```

- Save the calculation to the folder noSOC.

```
save_lapw -d noSOC
```

- Initialize the SOC using all the default parameters and run a SCF cycle with SOC.

```
init_so_lapw  
run_lapw -ec 0.0001 -cc 0.001 -so
```

- Calculate the band structure to help locate band crossings for potential Weyl points. Generate a $\Gamma - \Sigma - S - Z - N - \Gamma - Z - X - \Gamma$ k path with 600 intermediate points using XCrysDen [80], and save the k point list to a file `case.klist_band` (here the case is TaAs, so the file name is `TaAs.klist_band`). Afterward, check the `case.klist_band` for entries like “*****” that show a problem with format. If this formatting error appears, the number of points on the path needs to be reduced.

- Calculate the eigenvalues and wave functions for all k points selected on the path.

```
x lapw1 -band  
x lapwso
```

- Generate files for plotting the band structure, `case.spaghetti_ene`.

```
x spaghetti -so
```

- Plot the band structures without SOC and with SOC (Fig. 4.3c,d). For obtaining band structure data without SOC one has to run spaghetti program without `-so` option (`x spaghetti`) after the command `x lapw1 -band` and save the data for

plotting. There is a small gap of a few meV in the vicinity of the Weyl points because our path does not intersect the band crossing precisely.

- To calculate the chirality of the Weyl point, make an input file for the `WloopPHI.py` code. For TaAs, the input file is given below:

```
91
84:84
&WloopCoordinate
0.25000 0.00000 1.00000 ; 0.25000 0.00000 0.00000
0.29000 0.00000 1.00000 ; 0.29000 0.00000 0.00000
0.30000 0.04000 1.00000 ; 0.30000 0.04000 0.00000
0.29000 0.08000 1.00000 ; 0.29000 0.08000 0.00000
0.25000 0.08000 1.00000 ; 0.25000 0.08000 0.00000
0.24000 0.04000 1.00000 ; 0.24000 0.04000 0.00000
END
```

The description of input file line-by-line is given below:

Line 1: 91

This line gives the number of Wilson loops including the initial point and the final point on the trajectory.

Line 2: 84:84

It specifies the range of bands $n_a : n_b$ in Eq. (4.5). In TaAs (Fig. 4.2d) crossings occur between bands 84 and 85, hence only band 84 (lower band of the Weyl point, $n_a = n_b = N$) is considered. The chirality would switch the sign to opposite, if we were to select the upper band instead ($n_a = n_b = N + 1$). The phase vanishes if both bands are selected ($n_a = N, n_b = N + 1$). It is possible to select all underlying bands 1:84 if we suspect crossings between bands 83 and 84 might enter into the Wilson loop and interfere with the Weyl point in question.

Line 3: &WloopCoordinate

This line indicates the beginning of the Wilson loop coordinate list.

Lines 4-9:

```
0.25000 0.00000 1.00000 ; 0.25000 0.00000 0.00000
...
```

Each line contains the coordinates of a point on the initial Wilson loop and the final Wilson loop of the trajectory. Here, we define a hexagonal Wilson loop (thus six lines) whose starting coordinates k_x , k_y , and k_z are given first, before the semicolon, and the ending coordinates are given after the semicolon. Coordinates of the k points in the *conventional* (neither primitive, nor Cartesian) BZ can be extracted from **XCrysDen**. This loop coordinates are chosen in such a way that it encloses the band crossing at coordinate $(k_x = 0.28, k_y = 0.02, k_z = 0.59)$, which we will analyze concerning the chirality. The Wilson loop trajectory enclosing the Weyl point evolves along the k_z direction because the Weyl point which we want to characterize is located along the k -path Z–N in Fig. 4.2c. One can also use more k points to construct the Wilson loop by adding more lines to this section of the input file.

Line 10: END

This the end of the input. It should always be written in the input file.

- Execute **WloopPHI**

```
python /path/to/WIEN2k/SRC_BerryPI/BerryPI/WloopPHI.py Wloop.in [-sp] [-orb] [-p]
```

This is the most computationally intensive part. The **WloopPHI** script automatically executes the following steps for each Wilson loop along the trajectory: (i) generate a series of **case.klist** with coordinates of k points on the loop interpolated between the initial and final k points and (ii) run **BerryPI** to calculate the Berry phase ϕ on each loop. The second step includes execution of **WIEN2k** to generate wave functions for k on the loop and **Wien2wannier** to calculate the overlap matrix \mathbb{M} . The **WloopPHI** output data are tabulated in the **PHI.dat** file.

- Plot the data from **PHI.dat** and calculate the chirality using Eq. (4.6).

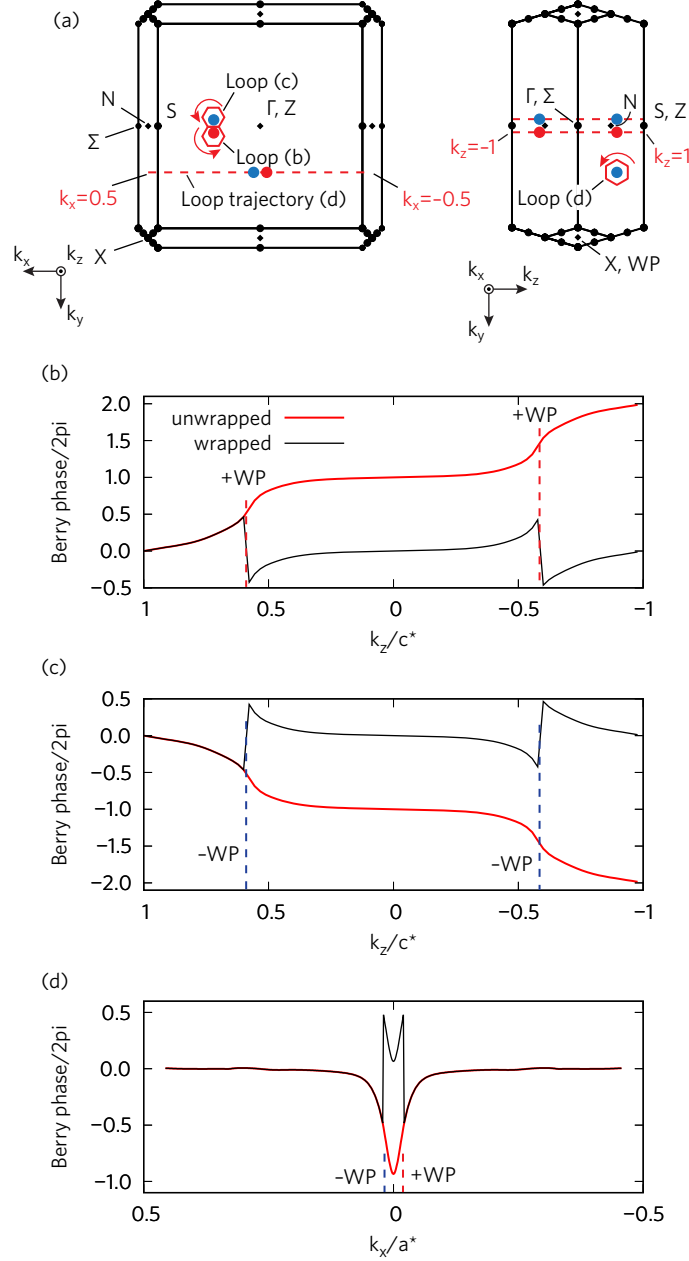


FIGURE 4.3: Characterization Weyl points in TaAs using the extended Wilson loop method. (a) BZ projections with Weyl points in questions. The loops and their trajectories are shown. Arrows indicate the order in which k points are assembled in the loop. (b,c,d) Evolution of the Berry flux through three different loops along their trajectories. (b) Two positive Weyl points. (c) Two negative Weyl points. (d) A pair of Weyl points of opposite chirality.

4.2.4 Convergence and reliability tests

The general strategy for finding Weyl points is to first analyze the *non-relativistic* band structure for the band crossings which hold a two-fold degeneracy (excluding spin). These crossings belong to continuous nodal lines that can be mapped within the BZ. Nodal lines of interest are those intersecting the Fermi energy. Weyl points are located in the proximity to these nodal lines. Finding exact positions of Weyl points is done by inspecting band crossings on *relativistic* band structures using off-symmetry k point trajectories. Afterwards, we construct the Wilson loop around the band crossings of interest and find the evolution of the Berry curvature along the Wilson loop trajectory which gives the information on the chirality.

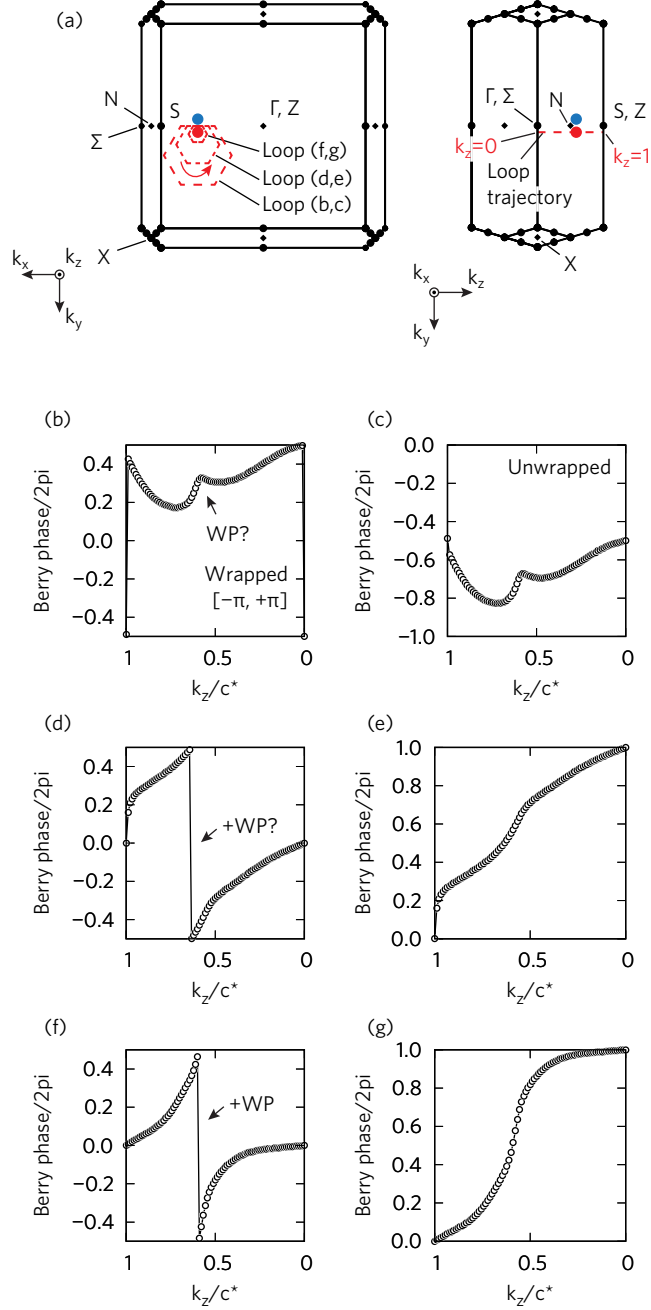


FIGURE 4.4: Effect of the Wilson loop size on evaluation of the Weyl node chirality in TaAs. (a) Brillouin zone with loops of various sizes (large, intermediate, and small). (b,d,f) Evolution of the Berry phase (wrapped) for large, intermediate, and small loops, respectively. (c,e,g) The same for the unwrapped Berry phase. The Weyl point identification using the largest loop has failed since other neighbouring Weyl point also contribute to the Berry flux and obstruct the result. Smaller loop sizes are preferable to achieve reliable data.

Calculations of the chirality are sensitive to two parameters: the size of the Wilson loop and the number of loops along the trajectory. Figure 4.4 shows the Wilson loop size effect on the computed Berry phase and the chirality. Here, we considered three cases of the loop size (large, medium, and small) with the same trajectory along k_z , which encloses one of the Weyl points in TaAs (Fig. 4.4a). Figure 4.4b shows the effect of a large loop size, where the computed Berry phase exhibits a smooth evolution along the trajectory without any discontinuity, even though the trajectory contains one Weyl point. Due to the large loop size, other Weyl points located nearby induce a non-negligible flux through the loop and interfere with the selected point. Thus, we are unable to characterize the Weyl point and obtain a wrong chirality ($\chi = 0$), as shown in Fig. 4.4c. Starting with a medium loop size it becomes possible to characterize the chirality of the Weyl point (Fig. 4.4d,e). The smaller is the loop, the easier to identify a discontinuity in the Berry phase and the more accurate is the chirality (Fig. 4.4f,g).

The effect of the number of intermediate Wilson loops along the trajectory path on characterization of a doublet of Weyl points in TaAs is shown in Fig. 4.5. For comparison, we have considered three cases with 21, 91, and 551 Wilson loops. This time we selected a doublet of closely-spaced Weyl points in k_x direction (Fig. 4.5a) of initially unknown chirality. If we compare the results in Fig. 4.5b,d,f, it is clearly shown that when we increase the number of Wilson loops, the evolution of the Berry phase becomes sharper allowing us to resolve two discontinuities, *i.e.*, two Weyl points. Since the unwrapped phase first drops and then raises again (Fig. 4.3g), we can conclude that the two Weyl points have different polarity and project no chirality on the 2D (100) surface BZ.

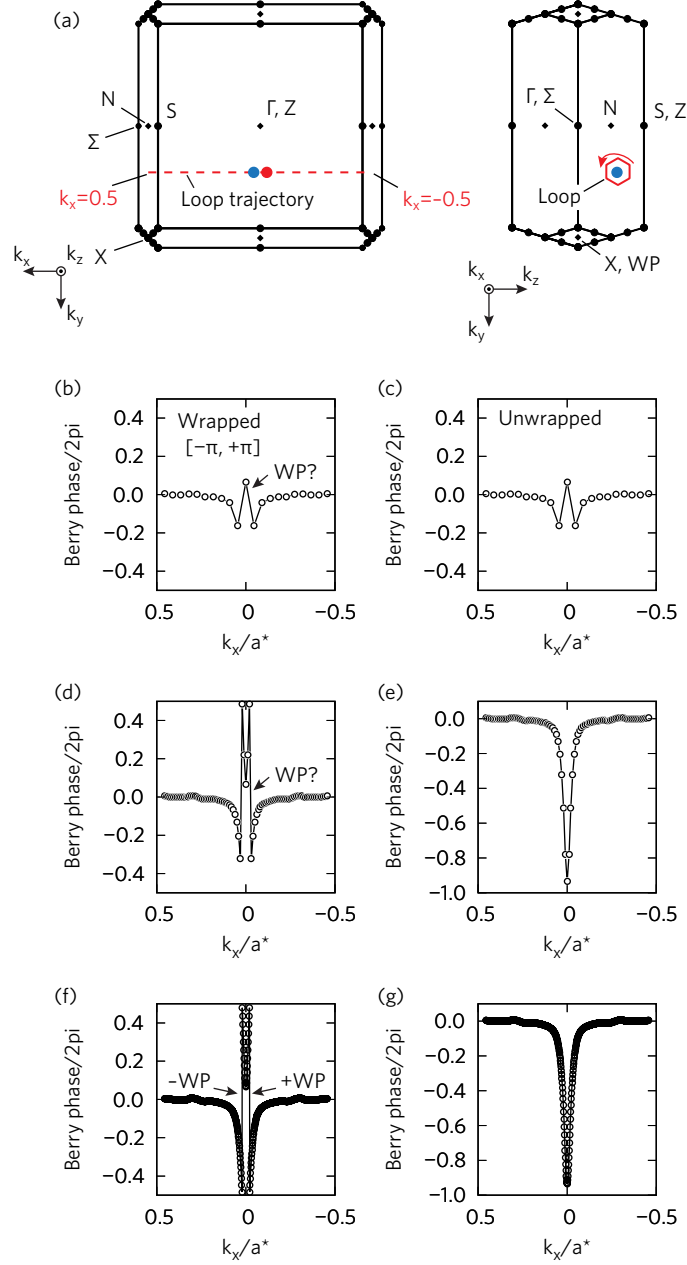


FIGURE 4.5: Effect of the number of intermediate Wilson loops along the loop trajectory on evaluation of the Weyl node chirality in TaAs: (a) Brillouin zone with Weyl nodes (only two relevant ones are shown), Wilson loop and its trajectory. (b,c), (d,e), (f,g) Evolution of wrapped and unwrapped Berry phase $\phi(k)$ along the loop trajectory sampled with 21, 91 and 551 equally spaced Wilson loops, respectively. The data get smoother and more reliable as the number of Wilson loops increases. Only with the highest mesh number we can clearly resolve two 2π discontinuities on the panel (f), which correspond to two Weyl points of opposite chirality $\chi = -1$ (left) and $\chi = +1$ (right).

4.3 Results

4.3.1 TaAs: method verification

To validate the method, we analyze the Weyl points of TaAs, a well-characterized topological material [3, 24, 52]. First, we calculate the band structure of TaAs without SOC with the PBE functional along high-symmetry directions in the BZ, as shown in Fig. 4.2b,c. The band structure plot without SOC (Fig. 4.2c) suggests that multiple band crossings (Dirac nodes) occur close to the Fermi energy along the Γ - Σ , Σ -S, S-Z, and Z-N lines. Our results are in good agreement with previous studies [3, 24]. For the band structure with SOC (Fig. 4.2d), we find that all the band crossings near the Fermi energy disappear. Instead, there is a small band gap of around 5 meV along the Z-N line. We can explore the vicinity of this k point to see if it includes any Weyl points.

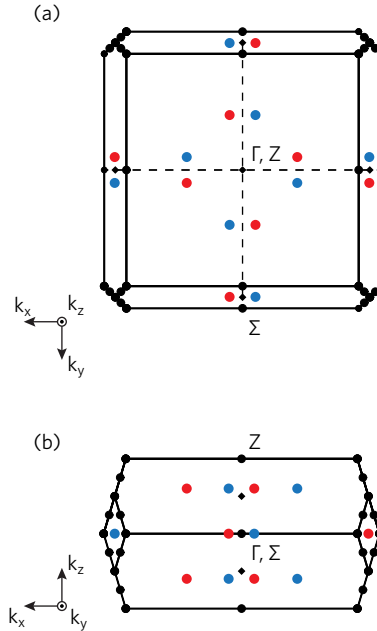


FIGURE 4.6: Mapping of Weyl points in the BZ of TaAs. (a,b) Top and side view of BZ. There are in total 12 pairs of Weyl points with +1 and -1 chirality marked as red and blue circles, respectively.

To calculate the chirality of the Weyl point formed by the band crossing along the Z-N direction in the BZ, we construct a Wilson loop which evolves from $k_z = 1$ to $k_z = -1$ in units of the conventional reciprocal lattice vector c^* (Fig. 4.3a). The result for loop (b) is plotted in Fig. 4.3b. It shows two Weyl points of chirality $\chi = +1$ each, which is an odd number (non-trivial), and hence it confirms the existence of Weyl points

in TaAs. Similarly, we apply our methodology to characterize other Weyl points in the BZ using loops (c) and (d) (see Fig. 4.3c,d), which include another pair of points with $\chi = -1$ and a pair of points with the opposite chirality. There are a total of 6 Weyl points in the irreducible BZ, which translates to 24 Weyl points in the whole BZ due to the fourfold rotation symmetry (Fig. 4.6). This result is in agreement with previous studies [3, 24, 52].

4.3.2 YRh₆Ge₄

Now that our method is validated, we can examine a recently proposed topological semimetal YRh₆Ge₄ [75–77]. YRh₆Ge₄ belongs to the $P\bar{6}m2$ space group with lattice parameters $a = b = 7.067(3)$ Å and $c = 3.862(2)$ Å [76] and angles $\alpha = \beta = 90^\circ$ and $\gamma = 120^\circ$. The structure optimization was performed with the projected augmented wave method [81, 82] as implemented in the Vienna *ab initio* simulation package package [83–85]. The PBE version of a generalized gradient approximation was used for the exchange-correlation functional. Pseudopotentials with semicore electrons were selected for Y, Rh, Ge and included 11, 15, 14 valence electrons, respectively. We used a kinetic energy cutoff of 390 eV for the plane-wave basis (25% higher than recommended) and the $5 \times 5 \times 8$ k -point mesh for BZ sampling. Both the cell parameters and internal atomic positions were fully relaxed until the forces on all atoms were smaller than 0.02 eV/Å. The optimized parameters were $a = b = 7.186$ Å and $c = 3.851$ Å. Once the equilibrium structure was obtained, the electronic structure calculation was performed with WIEN2k (the plane wave cutoff parameter of $RK_{\max} = 8$ and $5 \times 5 \times 10$ k -point mesh for BZ sampling).

Figure 4.7a,b shows the crystal structure and bulk BZ of YRh₆Ge₄, respectively. The calculated band structure of YRh₆Ge₄ without SOC is presented in Fig. 4.7c. We can see two types of band crossings $x4 - x6$. The search for Weyl points begins with inspecting a relativistic band structure along the same k path (Fig. 4.7d). Nodal points are now gapped due to the lack of inversion symmetry. The smallest gap emerges at the band crossing along the Γ -K direction ($x4$) in the BZ (labelled as WP on Fig. 4.7d). The location of WP in the BZ is illustrated in Fig. 4.8a,b. To evaluate the chirality of the WP Weyl points, we construct the Wilson loop with a trajectory from $k_z = -0.04$ to $k_z = +0.04$ plane (Fig. 4.8a,b). We choose the Wilson loop trajectory in such a way that it includes the pair of Weyl points WP along the Γ -K direction. The Berry phase evolution along the Wilson loop trajectory is plotted in Fig. 4.8c. One can identify the places of sharp increase and decrease in $\phi(k_z)$. The plot is similar to Fig. 4.3d. Further

analysis of the unwrapped Berry phase yields the chirality of the WP Weyl points $\chi = -1$ and $\chi = +1$.

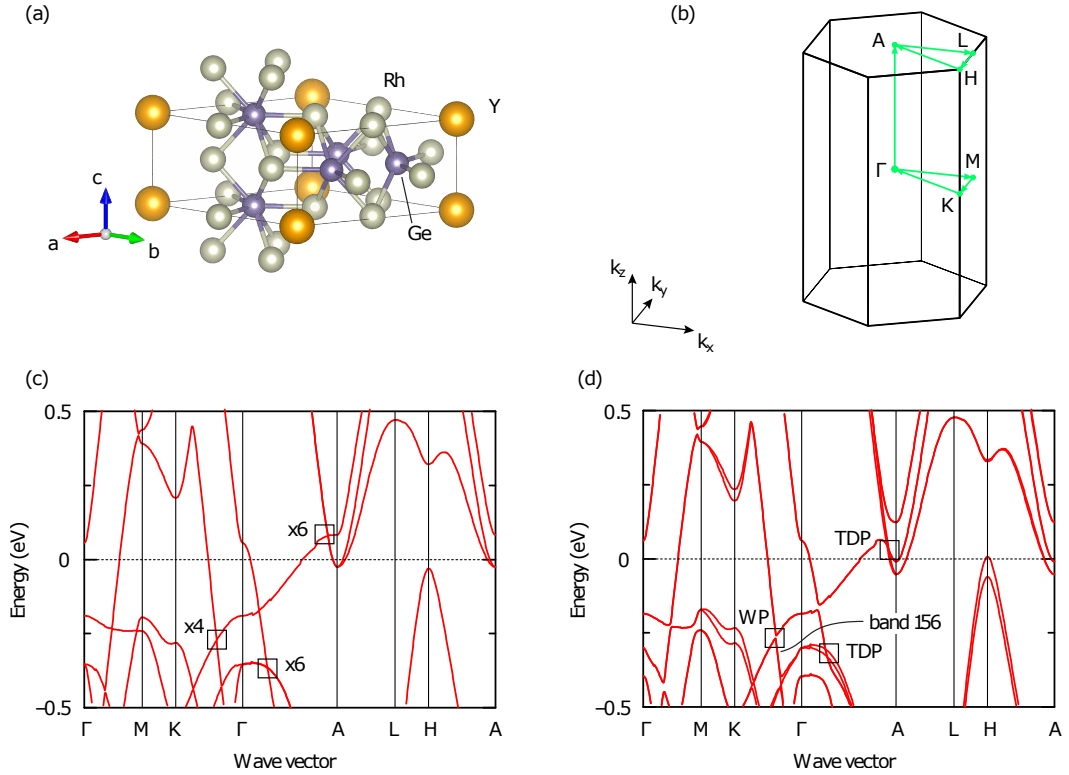


FIGURE 4.7: (a) Crystal structure of YRh_6Ge_4 . (b) Bulk BZ. (c) Band structure calculated with the PBE functional without SOC. Band crossings with two-fold degeneracies (excluding spin) are labelled $x4$. (d) Band structure with SOC. The proximity to the Weyl point is identified on a path between high-symmetry k points. TDPs refers to a pair of triply degenerate points.

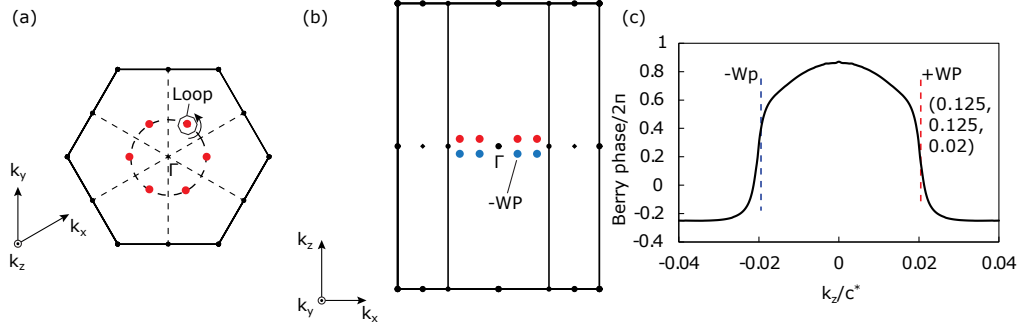


FIGURE 4.8: Mapping of Weyl point in the Brillouin zone of YRh_6Ge_4 : (a,b) The top and side view of the Brillouin zone. Weyl points are shown with red and blue solid circles. (c) Evolution of the Berry flux through the Wilson loops along its trajectory allows to identify a k_z coordinate, the sign and chirality of Weyl points.

Guo et al. [77] emphasized the presence of triply degenerate nodal points (TDPs) in the band structure of YRh_6Ge_4 (also marked as TDP in Fig. 4.7d). Of particular interest are the TDP crossings x6 near the A point, which are close to the Fermi energy. Because of D_{3h} point group symmetry, these crossings occur at the high symmetry axis $\Gamma - A$ which lie in the mirror plane $A - \Gamma - H$ of BZ in Fig. 4.7b [86]. Due to D_{3h} point group symmetry the C_3 eigenvalues of the bands are degenerate which results in the trivial pair of TDPs [87].

4.4 Conclusion

We described the methodology of `WloopPHI`, a code designed to calculate the chirality of band crossing points for the characterization of Weyl points using an extended Wilson loop method. The code `WloopPHI` has been implemented in `WIEN2k` (an all-electron density functional package). Our method is verified using `TaAs`—a well-known Weyl semimetal—and the results show good agreement with previous studies. Further, we have applied the approach to the newly studied material YRh_6Ge_4 . Its band structure without the spin-orbit coupling exhibits two types of crossings near to the Fermi energy. These crossings transform into Weyl point (located ~ 0.2 eV below the Fermi energy) when the spin-orbit coupling is included. The chirality (or monopole charge) of Weyl points is linked to a change in the Berry phase accumulated on the Wilson loop ($\pm 2\pi$) as the point in question passes through the surface of the loop. We mapped chirality and location in the Brillouin zone for Weyl point in the proximity of the Fermi energy.

The obtained results show that it is feasible to calculate the chirality of band crossings with the WloopPHI code.

Acknowledgements

Authors are indebted to Prof. Zhiqiang Mao (Pennsylvania State University) for drawing out attention to the YRh_6Ge_4 material. Funding was provided by the Natural Sciences and Engineering Research Council of Canada (NSERC) under the Discovery Grant Program RGPIN-2020-04788. Calculations were performed using a Compute Canada infrastructure supported by the Canada Foundation for Innovation under the John R. Evans Leaders Fund program.

Chapter 5

Thermodynamic stability of kagome lattice $A_3Sn_2S_2$: (A: Co, Rh, Ru)

Author contribution:

I had the concept during a discussion with Dr. Oleg Rubel. I performed the calculations and conducted the data analysis. I prepared the manuscript.. Dr. Oleg Rubel supervised the project. The chapter has not been published. Explanation in methodology section is adapted from the recently published article on computational approaches to predict the thermodynamic stability of inorganic solids [8]

Abstract

Using density functional theory (DFT) with adjusted total energies obtained by applying empirical corrections [88], we analyze the stability of the kagome-based materials $A_3Sn_2S_2$, where A is Co, Rh, or Ru, in the context of the ternary phase diagrams and competing binary compounds. We show that $Co_3Sn_2S_2$ and $Rh_3Sn_2S_2$ are stable compounds when we look at the convex hull of free energy. It is possible to synthesize $Co_3Sn_2S_2$ through the reaction of CoSn and CO_3S_4 , $Rh_3Sn_2S_2$ can be obtained through the reaction of $Rh_{17}S_{15}$ and Rh_2Sn . On the other hand, we find that $Ru_3Sn_2S_2$ is a compound that is thermodynamically unstable. In addition, we found that $Ru_3Sn_2S_2$ can be decomposed into SnS and Ru. Our work offers some insights for using the DFT to make predictions about new types of materials.

5.1 Introduction

In recent years, quantum materials have developed broadly in topological phase transitions, such as topological semimetals (TSM)[11, 89], where the presence of degeneracies in the band structures near the Fermi level are observed[90]. Semimetals possess a negligible or vanishing density of states near Fermi energy (E_F). Among them, a new class of materials exists where the isolated twofold degeneracies (Weyl nodes) at the band crossings of conduction and valence bands in the three-dimensional (3D) Brillouin zone (BZ) leads to a finite density of states. Weyl nodes are chiral, acting as monopole sources and sinks of Berry curvature in the BZ, and when the quantized Berry flux through some of the Fermi-surface sheets is nonzero the material is classified as a Weyl semimetal (WSMs)[90]. WSMs show the exotic transport properties – that cannot be described using the classical physics, for example anomalous Hall effect, which arises due to the spin-orbit coupling and the Berry curvature due to the presence of Weyl nodes[91–93]

It has been studied that the kagome lattice is the most fundamental model for the exotic topological phase in condensed matter physics[94]. The $Co_3Sn_2S_2$ is a thoroughly studied material based on kagome lattice. It shows a large anomalous Hall conductivity and a giant anomalous Hall angle originating from the Berry curvature[94]. The thermodynamic stability of the cobalt-based kagome lattice has been studied theoretically[49], where $Co_3MM'X_2$ ($M/M' = Ge, Sn, Pb$, and $X = S, Se, Te$, denoted as Co-MM'-X) compounds are investigated. For structural stability, they found a descriptor – the ratio of the radii of metal and the chalcogen atom, which describes the stability of the shandite crystal structure and the magnetic states. However, the study does not show the

thermodynamic stability with respect to convex Hull diagram. In thermodynamics, the formation enthalpy with respect to convex Hull is an important parameter to comment the stability of any structure. In order to find the stability of any ternary structure, we need the binary phases, and in their studies, they did not shed any light on the stability with respect to binary phases. The Materials project [95] solves the convex Hull diagram problem. We found all the binary phases and the ternary phase diagrams on the Materials project for $\text{Co}_3\text{Sn}_2\text{S}_2$, $\text{Rh}_3\text{Sn}_2\text{S}_2$, and $\text{Ru}_3\text{Sn}_2\text{S}_2$.

Here, we present the comprehensive study of the $\text{A}_3\text{Sn}_2\text{S}_2$ ($\text{A} = \text{Co}, \text{Rh}, \text{and Ru}$) compound and its stability related to the transition element. Our study is similar to the Materials project [88, 95]. For the transition elements we have considered the Co, Rh, and Ru because of their similar atomic radii and oxidation states to form the structure as tabulated in Table 5.1. The change in atomic radii are within 10% for Co, Rh, and Ru which shows Ru can replace Co in $\text{Co}_3\text{Sn}_2\text{S}_2$ which is experimentally observed material [94] without any distortion in the lattice. Moreover, Ru has same oxidation state +4 as of Co. Hence, our hypothesis is to find the stability of new hypothetical kagome based lattice material $\text{Ru}_3\text{Sn}_2\text{S}_2$ with respect to experimental observed materials $\text{Co}_3\text{Sn}_2\text{S}_2$ [94] and $\text{Rh}_3\text{Sn}_2\text{S}_2$ [96].

TABLE 5.1: Atomic radii and oxidation states data used in this work. Red color values of oxidation states the values we used to predict the initial structure with charge neutrality.

Elements	Atomic radii (\AA) [97]	Oxidation States [98]
Co	1.35	-3,-1,0,+1,+2,+3,+4,+5
Rh	1.35	-3,-1,0,+1,+2,+3,+4,+5,+6,+7
Ru	1.30	-4,-2,0,+1,+2,+3,+4,+5,+6,+7,+8
Sn	1.45	-4,-3,-2,-1,0,+1,+2,+3,+4
S	1.00	-2,-1,0,+1,+2,+3,+4,+5,+6

5.2 Methodology

5.2.1 Thermodynamic Stability

In this section the explanation was obtained from the recently published article on computational approaches to predict the thermodynamic stability of inorganic solids [8].

Inorganic crystalline solid materials are characterized by two characteristics: their composition, and their structure. Composition stands for the element used for the materials and in what proportions, whereas structure tells how the atoms of those elements arrange themselves into a periodic crystal. For the purpose of our study, we investigated the ground-state Density Functional Theory (DFT) calculations, which do not incorporate temperature effects (such as entropic effects or thermal expansion), and as a result, the thermodynamic potential is just the whole amount of energy, denoted by the letter E_{Total} . If the energy of a material can't be lowered by rearranging the atoms that make it up, then the material is thermodynamically stable according to the set of rules [8].

Inorganic crystalline solid materials are characterized by two characteristics: their composition, and their structure. Composition stands for the element used for the materials and in what proportions, whereas structure tells how the atoms of those elements arrange themselves into a periodic crystal. For the purpose of our study, we investigated the ground-state Density Functional Theory (DFT) calculations, which do not incorporate temperature effects (such as entropic effects or thermal expansion), and as a result, the thermodynamic potential is just the whole amount of energy, denoted by the letter E_{Total} . If the energy of a material can't be lowered by rearranging the atoms that make it up, then the material is thermodynamically stable according to the set of rules [8].

The stability of a system can be evaluated with regard to phase separation and phase transition when a predetermined set of parameters has been specified and the energies of all materials that are pertinent have been computed. The stability of a material with regard to phase transition can be ascertained by contrasting the energy of the material of interest with the energies of all crystalline polymorphs that share the same chemical composition. The crystal structure with the least amount of energy is often called the "ground-state polymorph." This structure is stable in terms of phase transition. Consider the hypothetical composition A_2X_5 (where A and X are arbitrary chemical

elements), which has the potential to crystallize into one of two different structures: α or β , with α being the ground-state and β being a metastable polymorph. To get the polymorphic instability of the β phase, one has to figure out the difference in total energy between the two phases [8]:

$$\Delta E_{gs}^{\beta} = E_{Total}^{\beta} - E_{Total}^{\alpha} \quad (5.1)$$

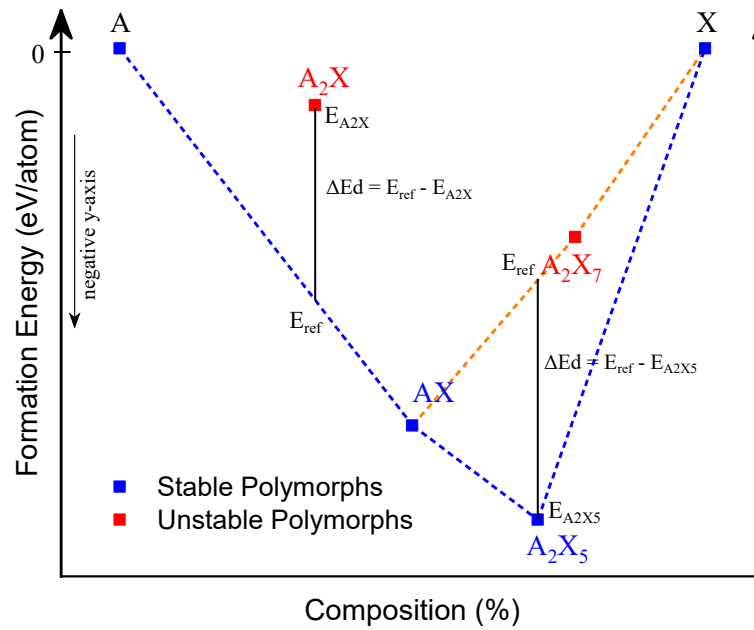


FIGURE 5.1: An illustrated example of convex hull diagram. The blue curve shows the convex hull and the orange curve represents the hypothetical convex hull. For A_2X $\Delta E_d < 0$ so it is unstable, and for A_2X_5 $\Delta E_d > 0$ therefore it is stable. Reprint with permission from [8], copyright 2022 Springer Nature.

The convex hull formalism is then used to evaluate the stability of all ground-state polymorphs over the relevant chemical space of interest in terms of phase separation. The convex hull is illustrated in Fig 5.1, where A and X represent arbitrary elements. AX and A_2X_5 (in blue) are examples of stable polymorphs, whereas A_2X and A_2X_7 (in red) are examples of unstable polymorphs. The goal of the convex hull analysis is to determine whether or not a specific material can reduce its energy by decomposing into a linear combination of other materials that have the same average composition as the material of interest. This is conceptually similar to the Gibbs energy

minimization approach [8]. From Fig 5.1, the formation energy, E_f , of A_2X_5 is obtained by referencing the elemental energies [8]:

$$\Delta E_f^{A_2X_5} = E_{Total}^{A_2X_5} - 2E_{Total}^A - 5E_{Total}^X. \quad (5.2)$$

Here, $E_{Total}^{A_2X_5}$, E_{Total}^A , and E_{Total}^X are the ground state total energies calculated by DFT approach.

The formation energies are produced as a function of some extensive property of the system, which is typically the molar composition of $N - 1$ elements in a chemical space that has N unique elements, for example, x in $A_{1-x}X_x$. The “convex hull of stability” is the term referring to the lower convex envelope that connects these points in formation energy-composition space. This hull is represented by the dashed blue line in Fig 5.1. Since the convex hull is defined across a space of fractional compositions, ΔE_f must be normalized per atom in each formula to ensure that compounds are represented on the basis of 1 mol of atoms per compound. In thermodynamics, the convex hull is a useful technique that can be utilized. Materials lying on the convex hull are thermodynamically stable with respect to phase separation, but materials lying above the hull are unstable because their energy can be decreased through a linear combination of alternate compositions. Any point above $\Delta E_f = 0$ or a comparable reference state is inherently unstable; hence, in thermodynamics, we only care about the "lower" convex hull.

The amount of instability in relation to phase separation is referred to as the decomposition energy, ΔE_d .

$$\Delta E_d = E_{ref} - E_{A_2X_5}. \quad (5.3)$$

where, E_{ref} and $E_{A_2X_5}$ are the formation energies shown in Fig 5.1.

In the case of unstable materials that are located above the convex hull, $\Delta E_d < 0$ is equal to the vertical distance in formation energy space that separates the material from the hull, as illustrated for A_2X in Fig 5.1. ΔE_d is the reaction energy for producing A_2X from the linear combination of neighbors in composition space. $\Delta E_d > 0$ for materials that are stable and lie on the convex hull. It is equivalent to the vertical distance in formation energy space between the material and a hypothetical convex hull (orange curve in Fig 5.1) that has been drawn without the material of interest. Because we

are investigating a hypothetical convex hull that does not include the stable material of interest, it is important to keep in mind that unstable materials have a chance of appearing in the breakdown process of stable materials. In the case shown in Fig 5.1, the breakdown reaction for the stable material A_2X_5 includes the unstable material A_2X_7 . This is due to the fact that A_2X_7 would be present on the hull in the absence of the stable material A_2X_5 [8].

The magnitude of the decomposition energy determines the amount of positive change in ΔE_f that a stable material may endure while still maintaining its stability, as well as the amount of negative change in ΔE_f that is necessary for an unstable material to become stable. When referring to thermodynamic stability in relation to phase separation or transition, the associated energy above the convex hull, also known as the ΔE_{Hull} , is frequently cited as the metric of choice [95]. When dealing with unstable materials, ΔE_{Hull} and ΔE_d are interchangeable; however, when dealing with stable materials, ΔE_{Hull} is always equal to zero, whereas ΔE_d can take on any value that is more than zero. In contrast to ΔE_{Hull} , which only indicates that the material is stable, ΔE_d quantifies how stable that substance is, providing valuable information regarding the uncertainty in the assessment of stability as well as the possibility of synthesis [8].

5.2.2 Formation energy predictions

It is possible to use any density functional theory code for thermodynamic calculations of inorganic crystals as long as it produces total energies. However, given that the generalized gradient approximation (GGA) is a standard approximation to the density functional theory, some practical points will focus on this method [99]. ΔE_d is the starting point for determining ΔE_f , and in order to make correct predictions of ΔE_f , it is necessary to accurately capture the energy differences that exist between compounds and their constituent elements. Convenient error cancellation in total energies is responsible for a significant portion of the success that local and semi-local density functionals have had in accurately representing the thermodynamics of materials [8]. That is to say, there is a possibility of making errors that are inherent to the calculation of total energies, but if these errors are systematic, the calculation of relative energies will have significantly fewer errors [8]. However, the degree to which errors can be cancelled out is directly proportional to the degree to which the materials being compared are

analogous [8]. For instance, it was identified that GGA overbinds the O₂ molecule, which results in a μ_0 (chemical potential of oxygen gas) that is overly negative [8]. This was discovered by observing the effects of GGA on the O₂ molecule. ΔE_f calculations for solid oxides entail doing an energy comparison between the solid and O₂ or any other element in the material [8]. Due to the fact that the level of overbinding for molecular O₂ is not comparable to any overbinding in cation-oxygen bonds that may occur in a crystal, GGA displays significant inaccuracies for the ΔE_f values of oxides [8]. The fact of the matter is that this problem may be readily fixed by adjusting the μ_0 value that represents the elemental reference energy for oxygen. By comparing the GGA-calculated ΔE_f to the experimentally measured enthalpies of formation, ΔH_f , at standard conditions, Wang et al. [88] were able to fit a simple correction to μ_0 for a set of six binary main group metal oxides (Li₂O, Na₂O, MgO, CaO, Al₂O₃, SiO₂). Consequently, all the total energies in our study have been adjusted using Wang et al. [88] empirical technique. In A₃Sn₂S₂, sulfur acts as an anion; hence, the correction applied to the total energy is -0.503 eV/atom, with the uncertainty as an anion being 0.0093 eV/atom [88]. In our total energies the correction was applied as per the equation:

$$\left[E_{Total}^{AS_2} \right]_{Corrected} = E_{Total}^{AS_2} + 2 \times (-0.503). \quad (5.4)$$

here, for example if we consider a compound AS₂ which contains two sulphur atoms we have to add the correction which is -0.503 eV/atom, therefore, we have to add 2×-0.503 to the total energy in order to get the corrected total energy.

5.2.3 Computational details for first-principles calculations

Structure relaxation

To begin, we optimized all of the structures of A₃Sn₂S₂, A–S, and A–Sn (A: Co, Rh, Ru). At the level of the DFT, the structures were relaxed with the help of Kresse and Joubert’s projector-augmented potentials [81, 82] in the Vienna ab initio package (VASP) [85]. It was indicated that Co and Rh each had 9 electrons, the Ru contained 8, the S had 6, and the Sn had 14 electrons. The Perdew-Burke-Ernzerhof (PBE) [99] functional was used so that the ground state energies could be determined. For k grid sampling, we used the fully automatic mesh, and a 600 eV cutoff was used for the plane

wave expansion. The input files (POSCAR and KPOINTS) for all the structures are supplied in Appendix C. To fully relax the structures, the forces between atoms had to be brought down to less than 0.001 eV/atom and the stress was 1kB. Since, our structures contains the transition element, therefore we also considered the magnetism during relaxation. All the initial structures with transition elements are considered as the ferromagnetic which was activated by setting the MAGMOM values in the INCAR file.

Data analysis

Visualization for Electronic and Structural Analysis (VESTA) [100] was used to visualize the crystal structures. The PBE exchange-correlation functional was utilized in VASP in order to derive the total energies, denoted by E_{Total} . Estimates of the formation energies are made using the equation presented in Eq. (5.2) with correction in the total energies (Eq. 5.4). For instance, the formation energy of $\text{Co}_3\text{Sn}_2\text{S}_2$ is calculated as follows:

$$\Delta E_f^{\text{Co}_3\text{Sn}_2\text{S}_2} = E_{Total}^{\text{Co}_3\text{Sn}_2\text{S}_2} - n_{\text{Co}}E_{Total}^{\text{Co}} - n_{\text{Sn}}E_{Total}^{\text{Sn}} - n_{\text{S}}E_{Total}^{\text{S}}. \quad (5.5)$$

where $n_{\text{Co}} = 3$, $n_{\text{Sn}} = 2$ and $n_{\text{S}} = 2$ are the number of atoms in the formula unit.

We have developed a Python code that allows the user to input formation energies and compounds into a *.csv file. This code will then be used to do an analysis of the ternary phase diagram. Additionally, it does an analysis on the ternary phase diagrams and plots them. In order to perform an analysis of the ternary phases, we must first examine all of the potential composition lines that connect the stable binary phases that are located on the edges of the ternary diagram, as is demonstrated in Fig 5.2. After that, an analysis of the formation energy was carried out on each of the intersection points shown in Fig 5.2(a)(c)(d), and the formation line that resulted in the lowest formation energy at the intersection is shown on the diagram in Fig 5.2(b)(d)(f). After obtaining all of the formation lines, we are able to obtain our result, which is the ternary phase diagram with binary phases. The limitation of this program is that it is unable to generate the complete ternary phase diagram with ternary phases. The work is under processing for this functionality. Due to our code limitation, we have explored the further phase diagram analysis with the Atomic Simulation Environment (ASE) python package [101].

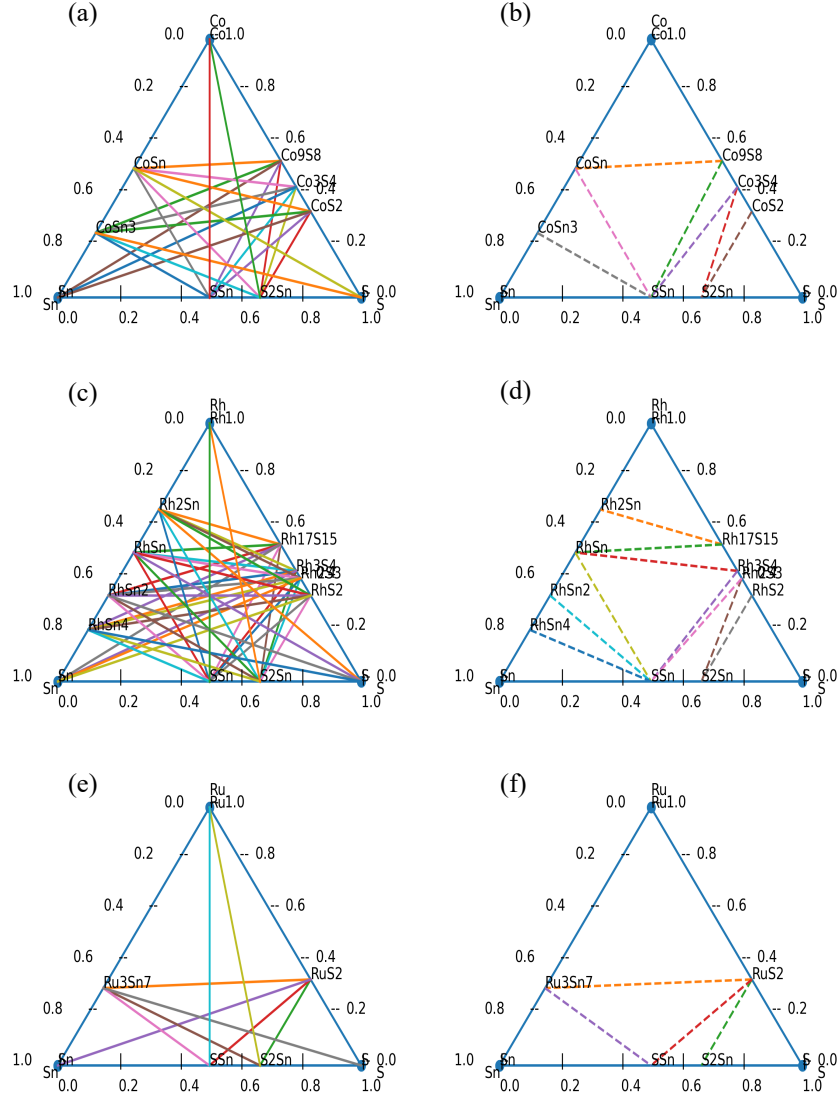


FIGURE 5.2: Illustration of ternary phase diagram using in-lab developed python code (see Appendix D). (a), (c), and (e) are composed with solid lines which shows all the possible compositions exist. (b), (d), and (f) are composed with dotted lines which belongs to the stable compositions. (a), (b) $\text{Co}_3\text{Sn}_2\text{S}_2$; (c), (d) $\text{Rh}_3\text{Sn}_2\text{S}_2$; (e), (f) $\text{Ru}_3\text{Sn}_2\text{S}_2$,

5.3 Results and Discussion

It is well known that the Shandite compound, composed of $\text{Co}_3\text{Sn}_2\text{S}_2$, is a ferromagnet. Its Curie temperature (T_c) is 177K, and its magnetic moment is $0.29 \mu_B/\text{Co}$ [94]. Below

the T_c , photoemission observations and band structure calculations demonstrated that $\text{Co}_3\text{Sn}_2\text{S}_2$ possesses Type-IA half-metallic ferromagnetism with spin-minority states that are separated by gaps [102, 103]. Fig 5.3 depicts the crystal structure of the compound $\text{A}_3\text{Sn}_2\text{S}_2$ (with $\text{A} = \text{Co}, \text{Rh}, \text{and Ru}$), where the blue atoms represent the elements Co, Rh, and Ru, while the gray and yellow atoms represent the elements Sn and S, respectively. The structures shown in Fig 5.3a have been crystallized in a rhombohedral form belonging to the space group R-3m (no. 166) also called trigonal shandite structure [94, 104]. Experimentally observed, $\text{Rh}_3\text{Sn}_2\text{S}_2$ crystallizes into a trigonal shandite type structure ($\text{Pb}_2\text{Ni}_3\text{S}_2$) [96]. The atomic projection on the Kagome lattice is illustrated in Fig 5.3b of the figure. Atoms of Sn can be found in the Kagome lattice in both the in-plane sites of the lattice and the sites that are in between the layers of the lattice. The optimum values for the lattice parameters of $\text{Co}_3\text{Sn}_2\text{S}_2$, $\text{Rh}_3\text{Sn}_2\text{S}_2$, and $\text{Ru}_3\text{Sn}_2\text{S}_2$ are respectively 5.375\AA , 5.574\AA , and 5.570\AA . The calculated lattice parameters for $\text{Co}_3\text{Sn}_2\text{S}_2$ and $\text{Rh}_3\text{Sn}_2\text{S}_2$ are in good agreement with the experimental values for example, $\text{Co}_3\text{Sn}_2\text{S}_2$ has 5.368\AA [94] and $\text{Rh}_3\text{Sn}_2\text{S}_2$ has 5.626\AA [96]. Moreover, the calculated value for the magnetic moment for $\text{Co}_3\text{Sn}_2\text{S}_2$ is $0.33\mu_B/\text{Co}$ which is consistent with the previous study [94]. However, the $\text{Rh}_3\text{Sn}_2\text{S}_2$ shows the zero magnetic moment and $\text{Ru}_3\text{Sn}_2\text{S}_2$ has $0.34\mu_B/\text{Ru}$ magnetic moment. All the values of magnetic moments are calculated without spin-orbit coupling.

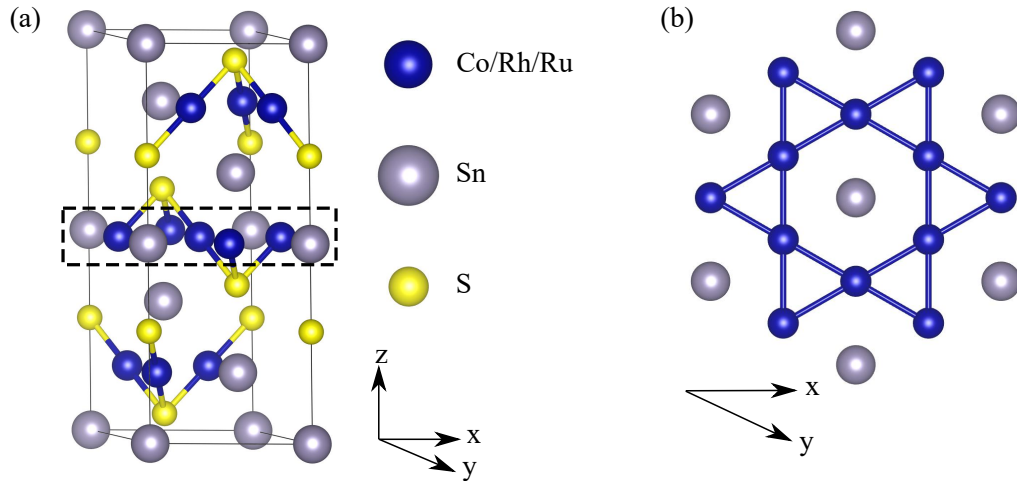


FIGURE 5.3: (a) Shandite's crystal structure: $\text{A}_3\text{Sn}_2\text{S}_2$ (with $\text{A} = \text{Co}, \text{Rh}, \text{and Ru}$). (b) The Kagome plane is incorporated into the structure of Shandite, highlighted by the dotted black line in (a).

We have explored the binary convex hull diagram of A-S, A-Sn, and S-Sn ($\text{A}: \text{Co}, \text{Rh},$

Ru) compounds utilizing minimum-enthalpy structures in order to calculate the thermodynamically stable structures as shown in Fig 5.4. Using the PBE-PAW, we performed the calculations on all of the structures to determine their enthalpies in the ground state. The binary hulls that were generated as a result indicate that there are probable phases of A-S, A-Sn, and S-Sn (A: Co, Rh, and Ru), all of which are anticipated to be stable. In the Table 5.2, the formation enthalpies as described in methodology section 5.2 and Eq. (5.2) for each of the different possible structures are given. We have also discussed the finite temperature correction for the DFT calculated formation energies with the experimental Appendix B and we found the DFT calculated formation energies can be used for the convex Hull and ternary phase diagram analysis. From Table 5.2 we found the several stable structures whose $\Delta E_{Hull} = 0$. The stable structures are Co_3S_4 , Co_9S_8 , CoS_2 , CoSn , CoSn_3 , RhS_2 , Rh_3S_4 , Rh_2S_3 , $\text{Rh}_{17}\text{S}_{15}$, RhSn , RhSn_2 , Rh_2Sn , RhSn_4 , RuS_2 , Ru_3S_7 , SSn , and S_2Sn . We used all these stable structure to further study the thermodynamical stability of the ternary phases $\text{A}_3\text{Sn}_2\text{S}_2$. The formation energies in our study are comparable (within the range of 70meV/atom) with the previously calculated values from Materials project database [88, 95]. The discrepancies occur due to the different $k - mesh$ used in our calculation as compared to the Materials project database. Additionally, we have compared the calculated formation energies with the experimental data [105, 106] as tabulated in Table 5.3, which shows the accuracy of our formation energies are within ± 0.22 eV/atom. Overall there is no major effect of the discrepancies on binary convex Hull diagram. The calculated convex Hull diagrams in this work is similar to the one on Materials project database [88, 95].

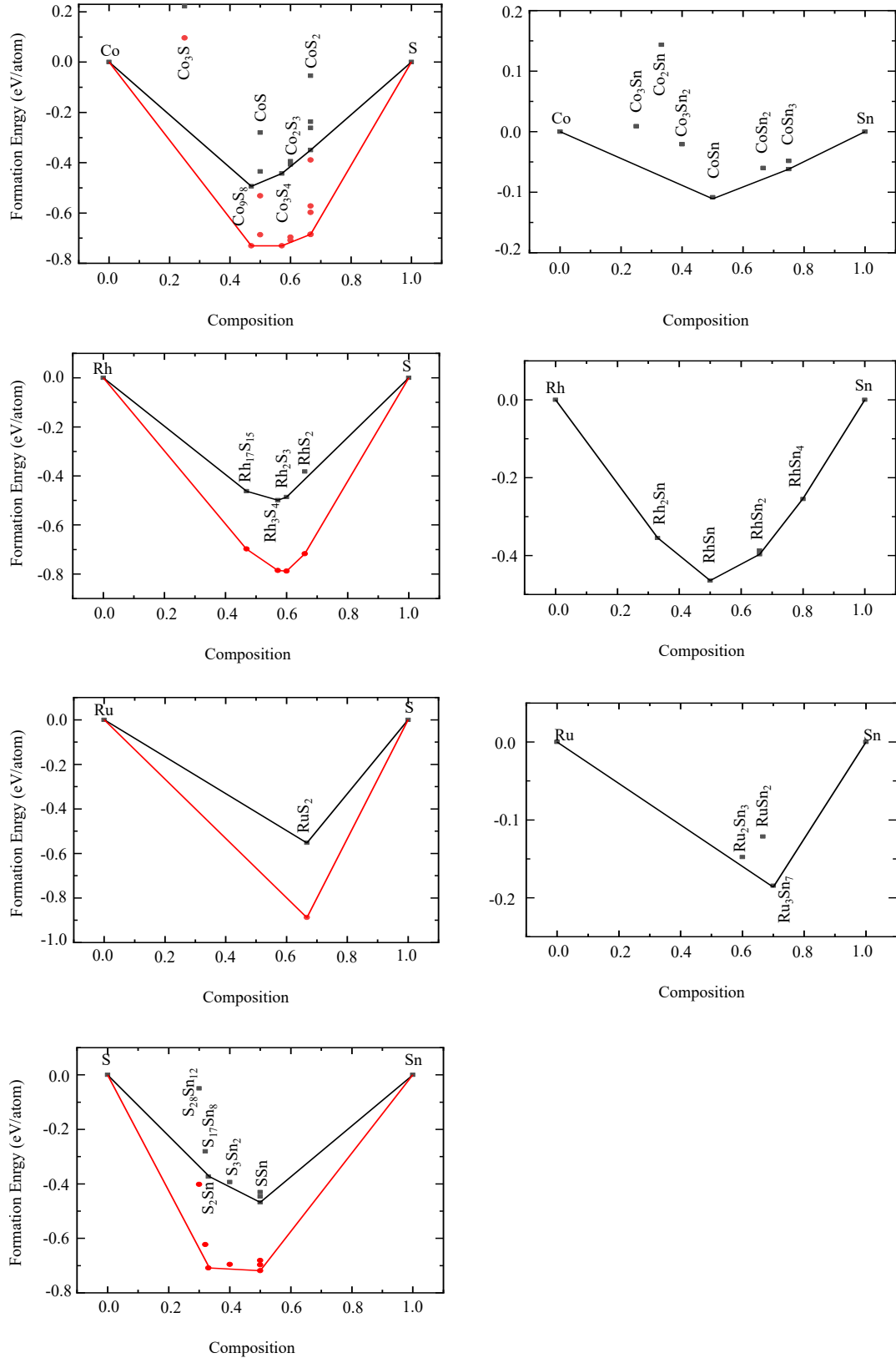


FIGURE 5.4: Convex Hull diagrams of all the binary crystal structures.(a)Co–S. (b)Co–Sn. (c)Rh–S. (d)Rh–Sn. (e)Ru–S. (f)Ru–Sn. (g)S–Sn. Here red curves are the corrected formation energies for sulphur [88].

TABLE 5.2: The formation enthalpies for each of the binary polymorphs are given together with the information regarding their crystal structures. All the formation enthalpies are compared with the existing results from Materials project database [88, 95]. Since, sulfur acts as an anion; hence, the correction applied to the total energy is -0.503eV/atom [88].

Binary Poly-morphs	Crystal System	Space Group No.	Formation Enthalpy, $E_f(\text{eV/atom})$	Formation Enthalpy, $E_f(\text{eV/atom})$ [88, 95] /	Energy above Hull, $E_{Hull}(\text{eV/atom})$
Co ₂ S ₃	Trigonal	167	-0.7085	-0.712	0.0079
Co ₂ S ₃	Tetragonal	141	-0.6961	-0.690	0.0196
Co ₃ S	Hexagonal	194	0.0966	0.109	0.4132
Co ₃ S ₄	Cubic	227	-0.7303	-0.726	0
Co ₉ S ₈	Cubic	225	-0.7301	-0.716	0
CoS	Tetragonal	129	-0.6862	-0.672	0.0419
CoS	Hexagonal	194	-0.5321	-0.534	0.1981
CoS ₂	Cubic	205	-0.6848	-0.693	10^{-05}
CoS ₂	Orthorhombic	61	-0.6853	-0.691	0
CoS ₂	Cubic	227	-0.5972	-0.594	0.0898
CoS ₂	Trigonal	166	-0.5722	-0.574	0.0621
CoS ₂	Tetragonal	122	-0.3891	-0.375	0.2956
Co ₂ Sn	Hexagonal	194	0.1434	0.141	0.2151
Co ₃ Sn	Hexagonal	194	0.0887	0.0940	0.1622
Co ₃ Sn ₂	Orthorhombic	62	-0.0207	-0.0178	0.0679
CoSn	Hexagonal	191	-0.1085	-0.108	0
CoSn ₂	Tetragonal	140	-0.0601	-0.0602	0.01811
CoSn ₃	Tetragonal	142	-0.0482	-0.0554	0.0136
CoSn ₃	Orthorhombic	64	-0.0619	-0.0521	0
RhS ₂	Cubic	205	-0.7174	-0.699	0

Continued on the next page

Continued from previous page

Binary Poly-morphs	Crystal System	Space Group No.	Formation Enthalpy, E_f (eV/atom)	Formation Enthalpy, E_f (eV/atom) [88, 95]	Energy above Hull, E_{Hull} (eV/atom)
Rh ₃ S ₄	Monoclinic	12	-0.7860	-0.760	0
Rh ₂ S ₃	Orthorhombic	60	-0.7881	-0.762	0
Rh ₁₇ S ₁₅	Cubic	221	-0.6979	-0.654	0
RhSn	Cubic	198	-0.4642	-0.463	0
RhSn ₂	Orthorhombic	64	-0.3966	-0.415	0
Rh ₂ Sn	Orthorhombic	62	-0.3547	-0.363	0
RhSn ₄	Tetragonal	142	-0.2547	-0.270	0
RhSn ₂	Tetragonal	140	-0.3869	-0.399	0.02
RuS ₂	Cubic	205	-0.8872	-0.885	0
RuSn ₂	Tetragonal	140	-0.1213	-0.147	0.0616
Ru ₂ Sn ₃	Tetragonal	116	-0.1476	-0.179	0.0187
Ru ₃ Sn ₇	Cubic	229	-0.1844	-0.210	0
SSn	Orthorhombic	62	-0.6974	-0.689	0
SSn	Orthorhombic	63	-0.6814	-0.627	0.016048
SSn	Cubic	225	-0.7190	-0.650	0.022797
S ₃ Sn ₂	Orthorhombic	62	-0.6995	-0.698	0.0004
S ₂ Sn	Trigonal	164	-0.7084	-0.710	0
S ₂₈ Sn ₁₂	Hexagonal	194	-0.4015	NA	0.1895
S ₁₇ Sn ₈	Orthorhombic	56	-0.6225	NA	0.0813

TABLE 5.3: The comparison between calculated Formation energies in this work to the experimental known values. The correction applied to the calculated total energy is -0.503eV/atom [88].

Compounds	Formation Enthalpy, E_f (eV/atom)	Experimental Formation Enthalpy, E_f (eV/atom) [105, 106]
Co ₃ S ₄	-0.730	-0.515
Co ₉ S ₈	-0.730	-0.530
CoS ₂	-0.685	-0.508
CoSn	-0.108	-0.152
RhSn ₂	-0.396	-0.436
RuS ₂	-0.887	-0.711
Ru ₃ Sn ₇	-0.184	-0.309
SSn	-0.697	-0.568
S ₂ Sn	-0.708	-0.490

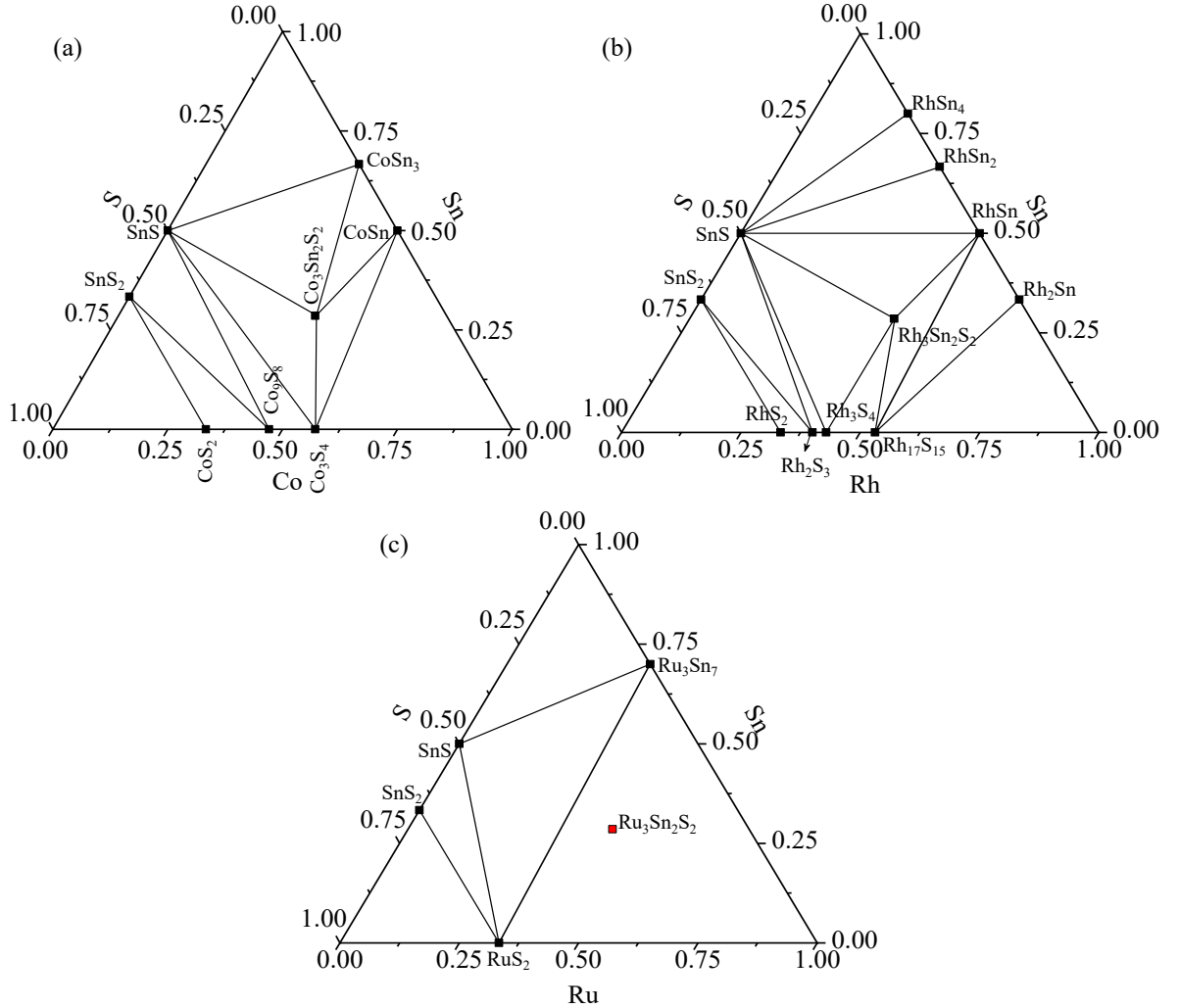
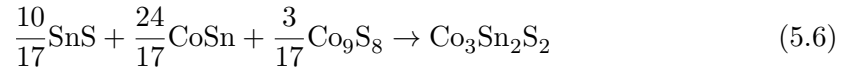


FIGURE 5.5: Ternary phase diagrams for $\text{A}_3\text{Sn}_2\text{S}_2$ (A: Co, Rh, Ru). (a) $\text{Co}_3\text{Sn}_2\text{S}_2$. (b) $\text{Rh}_3\text{Sn}_2\text{S}_2$. (c) $\text{Ru}_3\text{Sn}_2\text{S}_2$, here red dot represents the unstable structure. Illustrations are produced by using data and confirmed from Materials project [88, 95] and ASE python package [101]

The outcomes of our calculations are presented in Table 5.2, and using those results, we were able to investigate the stability of the ternary compounds using our ternary phase diagrams, which are depicted in Fig 5.5. The stable phases of binary compounds are projected on the edges of the ternary phase diagram. This information was obtained by our binary convex hull analysis, which is seen in Fig 5.4. The phase diagrams demonstrate the stability of ternary compounds with respect to binary stable structures. However, to find the stability with respect to the reactants, we have to project the ternary compound illustrated in Fig. 5.6 onto the phase diagram composed of binary

structures (as shown in Fig. 5.2(b),(d),(f)). Afterwards, with the help of triangulation (red triangles in Fig. 5.6), we can find the E_{rxn} for the required compound. One can find the reactants using the triangle vertices. The results are shown in Fig 5.6, where $\text{Co}_3\text{Sn}_2\text{S}_2$ can be a stable structure with respect to the reactants such as SnS, CoSn, and Co_9S_8 . The calculated ternary phase diagrams in this study are consistent available on Materials project [88, 95].

To this point we have defined the reactants but we do not know whether the reaction is stable or not. To find the stability of the reaction we have to find the reaction energy ΔE_{rxn} , for example the reaction for the $\text{Co}_3\text{Sn}_2\text{S}_2$ is



therefore the $\Delta E_{rxn}(eV/f.u)$ is given by

$$\Delta E_{rxn} = E_f(\text{Co}_3\text{Sn}_2\text{S}_2) - \left[\frac{10}{17} \times E_f(\text{SnS}) + \frac{24}{17} \times E_f(\text{CoSn}) + \frac{3}{17} \times E_f(\text{Co}_9\text{S}_8) \right] \quad (5.7)$$

where E_f is the formation energy of the reactants and product. The formation energies are given in Table 5.4, and if we insert the values in the Eq. 5.7 the $\Delta E_{rxn} = -0.1579eV/f.u.$. Here, the negative value of ΔE_{rxn} shows the the product can be synthesis using the reactants. Therefore, we can say the the $\text{Co}_3\text{Sn}_2\text{S}_2$ can be synthesized using the reactants SnS, CoSn, and Co_9S_8 . Similarly, we have calculated the reaction energies for $\text{Rh}_3\text{Sn}_2\text{S}_2$ and $\text{Ru}_3\text{Sn}_2\text{S}_2$, and the results are given in Table 5.5. After looking into the formation energy for $\text{Rh}_3\text{Sn}_2\text{S}_2$ ($\Delta E_{rxn} = -0.1766eV/f.u.$) we found that the $\text{Rh}_3\text{Sn}_2\text{S}_2$ can be synthesis using the reactants SnS, RhSn, and Rh_3S_4 . Whereas for $\text{Ru}_3\text{Sn}_2\text{S}_2$ has $\Delta E_{rxn} = 0.7616eV/f.u.$ shows that this compound is highly unstable as compared to the RuS_2 , Ru, and Ru_3S_7 . Therefore, from our analysis we confirm two stable ($\text{Co}_3\text{Sn}_2\text{S}_2$, $\text{Rh}_3\text{Sn}_2\text{S}_2$) and one unstable ($\text{Ru}_3\text{Sn}_2\text{S}_2$) kagome lattice based compounds.

TABLE 5.4: The formation enthalpies for reactants and product. The correction applied to the total energy is $-0.503eV/\text{atom}$ [88].

Compounds	Formation Enthalpy, $E_f(eV/f.u.)$
SnS	-1.3948
CoSn	-0.2170

Continued on the next page

Continued from previous page

Compounds	Formation Enthalpy, E_f (eV/f.u.)
Co ₉ S ₈	-12.4131
Co ₃ Sn ₂ S ₂	-3.4754
RhSn	-0.9284
Rh ₃ S ₄	-5.5026
Rh ₃ Sn ₂ S ₂	-4.5251
RuS ₂	-2.6616
Ru ₃ Sn ₇	-1.8441
Ru ₃ Sn ₂ S ₂	-2.4269

TABLE 5.5: Chemical reactions and their reaction energies for the Co₃Sn₂S₂, Rh₃Sn₂S₂, and Ru₃Sn₂S₂. The correction applied to the total energy is -0.503eV/atom [88].

Chemical reactions	Reaction energy, ΔE_{rxn} (eV/f.u.)	Stability
$\frac{10}{17}\text{SnS} + \frac{24}{17}\text{CoSn} + \frac{3}{17}\text{Co}_9\text{S}_8 \rightarrow \text{Co}_3\text{Sn}_2\text{S}_2$	-0.1579	Stable
$\frac{2}{7}\text{SnS} + \frac{12}{7}\text{RhSn} + \frac{3}{7}\text{Rh}_3\text{S}_4 \rightarrow \text{Rh}_3\text{Sn}_2\text{S}_2$	-0.1766	Stable
$\text{RuS}_2 + \frac{8}{7}\text{Ru} + \frac{2}{7}\text{Ru}_3\text{Sn}_7 \rightarrow \text{Ru}_3\text{Sn}_2\text{S}_2$	0.7616	Unstable

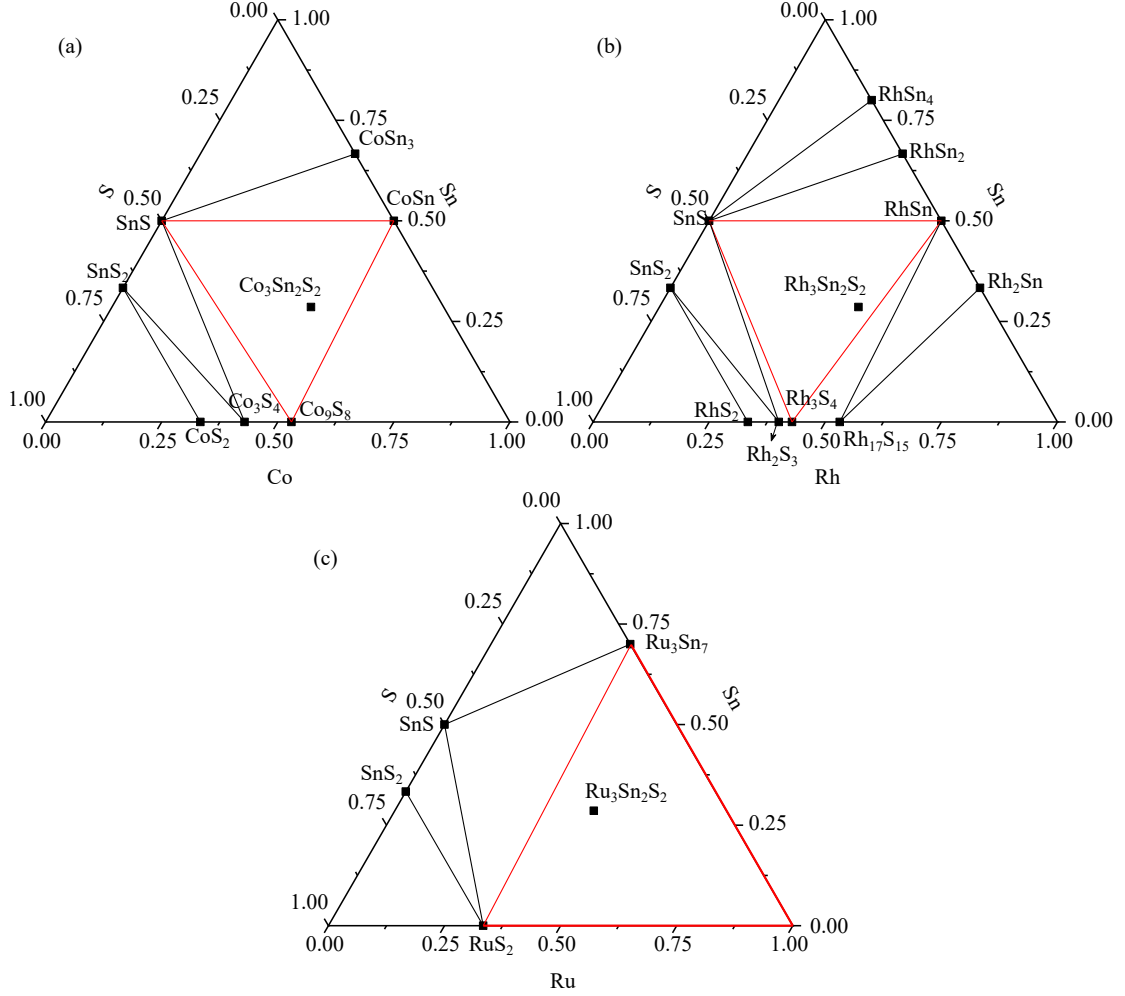


FIGURE 5.6: Reaction prediction using ternary phase diagram for $\text{A}_3\text{Sn}_2\text{S}_2$ (A: Co, Rh, Ru). (a) $\text{Co}_3\text{Sn}_2\text{S}_2$. (b) $\text{Rh}_3\text{Sn}_2\text{S}_2$. (c) $\text{Ru}_3\text{Sn}_2\text{S}_2$. Diagrams are produced using the data and confirmed by in-lab developed python code (see Appendix D). Red triangles shows the compound which we considered for the calculation of the $\Delta E_{rxn,0}$

5.4 Conclusion

We computed the thermodynamic stability of the $\text{A}_3\text{Sn}_2\text{S}_2$ (A: Co, Rh, Ru) system using DFT. At the beginning of our calculations, which is at 0K, the PBE functional predicts multiple binary phases for our investigation. According to the convex hull study, Co_3S_4 , Co_9S_8 , CoS_2 , CoSn , CoSn_3 , RhS_2 , Rh_3S_4 , Rh_2S_3 , $\text{Rh}_{17}\text{S}_{15}$, RhSn , RhSn_2 , Rh_2Sn , RhSn_4 , RuS_2 , Ru_3S_7 , SSn , and S_2Sn are the most stable binary compounds we found. All formation energies of binary structures are consistent with previously computed values

[95]. Using ternary phase diagrams, we were able to examine tertiary compounds with the aid of these binary compounds. According to our study, $\text{Co}_3\text{Sn}_2\text{S}_2$ and $\text{Rh}_3\text{Sn}_2\text{S}_2$ reside at the convex hull and hence, are thermodynamically stable. The calculated value for ΔE_{rxn} of $\text{Co}_3\text{Sn}_2\text{S}_2$ with respect to SnS, CoSn and Co_9S_8 is -0.1579 eV/f.u. and for $\text{Rh}_3\text{Sn}_2\text{S}_2$ with respect to SnS, RhSn and Rh_3S_4 is -0.1766 eV/f.u.. On the other hand, $\text{Ru}_3\text{Sn}_2\text{S}_2$, a newly hypothetical kagome lattice-based material, is unstable with ΔE_{rxn} of 0.7616 eV/f.u. with respect to RuS_2 , Ru, and Ru_3S_7 . The stable compounds we found in our study is also experimentally synthesized [94, 96]. Additionally, we confirm that $\text{Co}_3\text{Sn}_2\text{S}_2$ is a magnetic material with $0.33\mu_B/\text{Co}$ (without spin-orbit coupling), whereas $\text{Rh}_3\text{Sn}_2\text{S}_2$ is non-magnetic. $\text{Ru}_3\text{Sn}_2\text{S}_2$ shows magnetism with $0.34\mu_B/\text{Ru}$ (without spin-orbit coupling). Overall, this study gives the insight methodology to use the DFT in order to design the stable materials with the help of formation and reaction energies. It also shows how the convex Hull and ternary phase diagrams help to screen out the materials on the basis of their stability. Moreover, the in-lab developed python code is used to plot the ternary phase diagram.

Acknowledgements

The authors acknowledge funding provided by the Natural Sciences and Engineering Research Council of Canada (NSERC) under the Discovery Grant Program RGPIN-2020-04788. Calculations were performed using a Compute Canada infrastructure supported by the Canada Foundation for Innovation under the John R. Evans Leaders Fund program.

Appendix A

Chapter 4 Supplement: Block diagram of WloopPHI code.

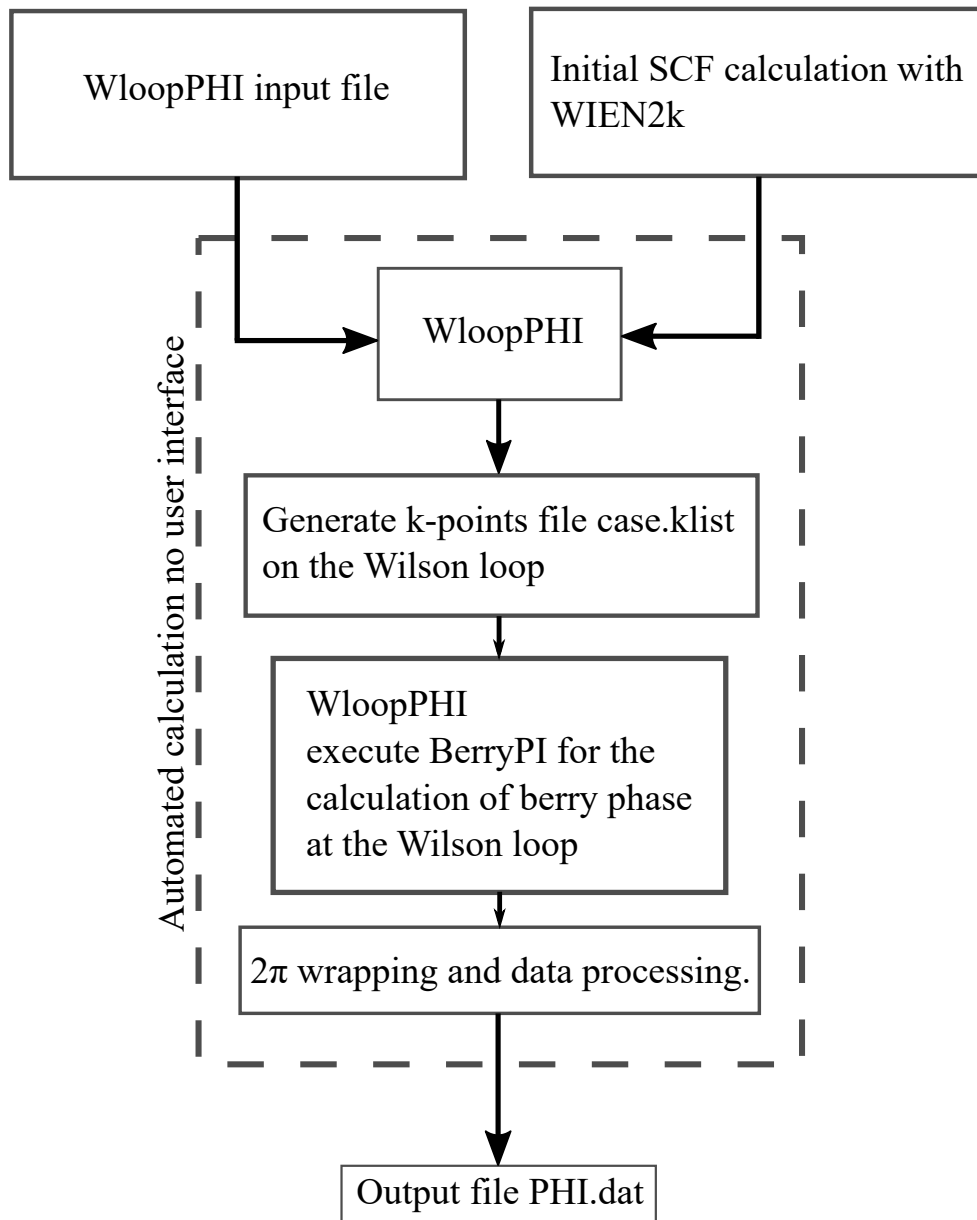


FIGURE A.1: Block diagram of WloopPHI code.

Appendix B

Chapter 5 Supplement: Finite temperature correction in DFT calculated formation energies.

The content in thi Appendix was adapted from the work done by Benisek, A., and Dachs, E [107]. They discussed in order to construct a phase diagram using DFT, it is necessary to calculate the formation energy of the compounds involved precisely. To reflect an accurate analysis, however, it is necessary to account for the uncertainties of reaction energies, as DFT calculations are performed at 0K. The experimental uncertainties for reaction enthalpies derived from solution calorimetry are typically on the order of a few kJ/mol, whereas those for standard entropy values derived from relaxation calorimetry do not exceed 1% [107]. For reliable phase diagrams, the formation energy data from DFT calculations should not exceed the uncertainty range of these two calorimetric techniques. From the DFT-derived formation energy, the standard enthalpy can be calculated, presuming it is equal to the formation enthalpy at 0K [107]

$$\Delta H_f^{298.15} = \Delta_f H^{0K} + \int C_p dT, \quad (\text{B.1})$$

here, C_p is the constant-pressure heat capacity.

The example calculation is shown in Fig. B.1 [107]. Here, the reaction $2\text{MgO} + \text{SiO}_2 = \text{Mg}_2\text{Si}_4$ was investigated. Its reaction energy at 0K ($\Delta_R U^{0K}$) was calculated by the DFT method and it is assumed that the reaction enthalpy at 0K ($\Delta_R H^{0K}$) is identical. Adding the formation enthalpies of the oxides at 0K ($\Delta_R H_{ox}^{0K}$) to this $\Delta_R H^{0K}$ value results in the formation enthalpy of forsterite from the elements at 0K ($\Delta_f H_{fo}^{0K}$). The heat content from 0 to 298.15 K ($= \int C_p^{fo} dT$) is than added to this value yielding finally the standard enthalpy of formation of forsterite from the elements ($\Delta_f H_{fo}^{298.15K}$).

If we compared the DFT calculated value of $\Delta_f H_{fo}^{298.15K} = -2173.07 \text{kJ/mol}$ for forsterite (Mg_2Si_4) to the experimental value $\Delta_f H^{298.15K} = -2172.57 \text{kJ/mol}$ [107], then the change in formation enthalpies are less than 1% which ensures that the DFT calculated values can be used for phase diagram analysis [107].

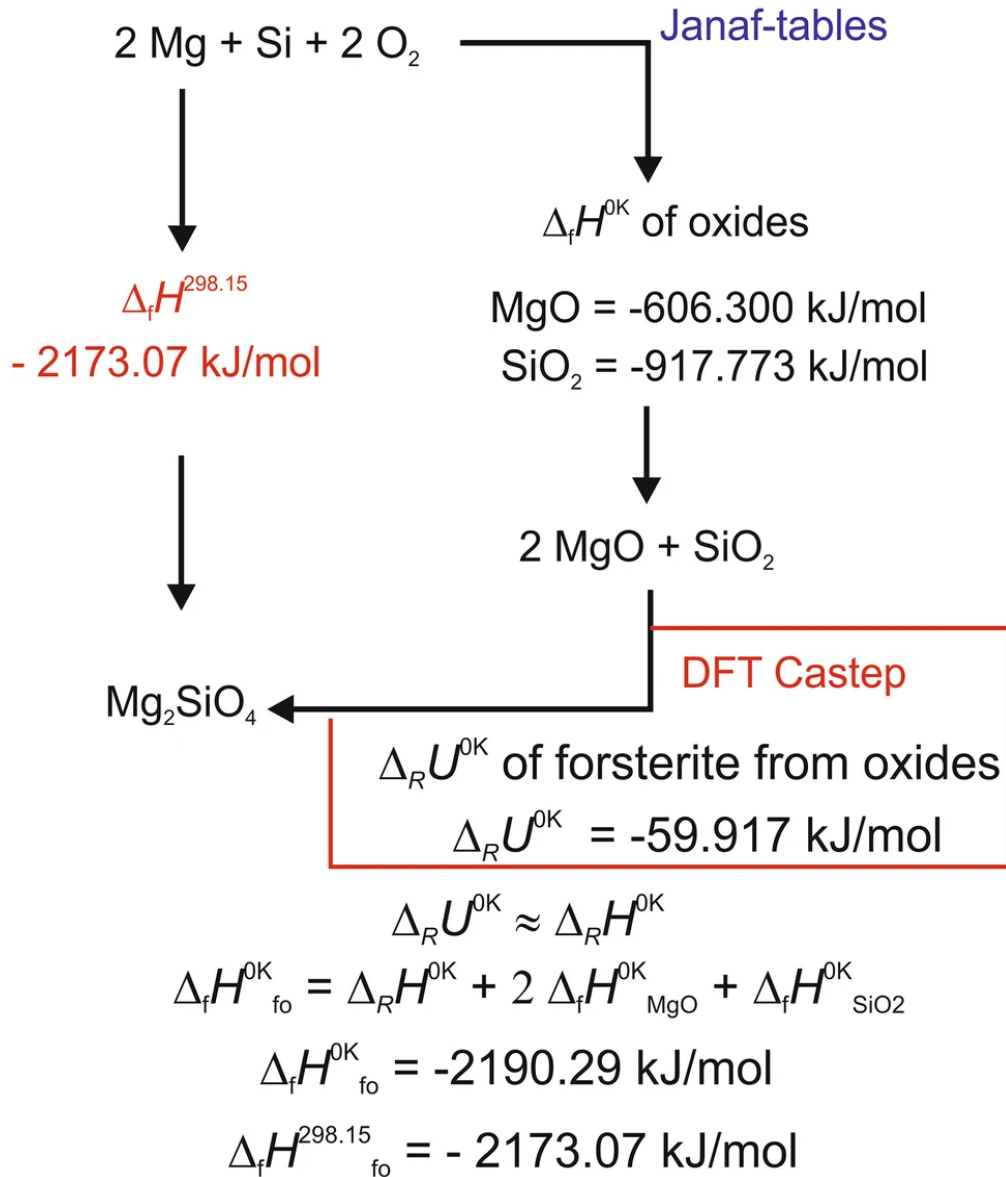


FIGURE B.1: Calculation procedure for forsterite. Reprint with permission from [107], copyright 2018 Springer Nature. This article has Open Access permission under the terms of the Creative Commons Attribution 4.0 International License.

Appendix C

**Chapter 5 Supplement: DFT
input files for all the structures.**

The input files POSCAR and KPOINTS for all the structures with space group number (SG) are shown below.

1. $\text{Co}_3\text{Sn}_2\text{S}_2$ SG:166

```

1 XCrySDen XSF file
2 1.0000000000000000
3 2.6866198364732385 -1.5511216863951995 4.3849409336021523
4 -0.0000000454275811 3.1022378577660010 4.3849408883068257
5 -2.6866200538294898 -1.5511216134360271 4.3849408684057769
6 Co Sn S
7 3 2 2
8 Direct
9 0.5000000000000000 0.0000000000000000 0.0000000000000000
10 0.0000000000000000 0.0000000000000000 0.5000000000000000
11 0.0000000000000000 0.5000000000000000 0.0000000000000000
12 0.0000000000000000 0.0000000000000000 0.0000000000000000
13 0.5000000000000000 0.5000000000000000 0.5000000000000000
14 0.7192396504151843 0.7192396504158385 0.7192396504151700
15 0.2807603495848157 0.2807603495841615 0.2807603495848300
16
17 0.00000000E+00 0.00000000E+00 0.00000000E+00
18 0.00000000E+00 0.00000000E+00 0.00000000E+00
19 0.00000000E+00 0.00000000E+00 0.00000000E+00
20 0.00000000E+00 0.00000000E+00 0.00000000E+00
21 0.00000000E+00 0.00000000E+00 0.00000000E+00
22 0.00000000E+00 0.00000000E+00 0.00000000E+00
23 0.00000000E+00 0.00000000E+00 0.00000000E+00

```

LISTING C.1: POSCAR

```

1 Automatic mesh
2 0 ! number of k-points = 0 -> automatic generation
   scheme
3 Auto ! fully automatic
4 81 ! length (R_k)

```

LISTING C.2: KPOINTS

2. $\text{Rh}_3\text{Sn}_2\text{S}_2$ SG:166

```

1 Sn2 Rh3 S2
2 1.0
3 5.5834746361 0.0000000000 0.0000000000
4 2.6484369717 4.9153810247 0.0000000000
5 2.6484369717 1.5814160132 4.6540406113
6 Sn Rh S

```

```

7      2      3      2
8 Direct
9      0.000000000      0.000000000      0.000000000
10     0.500000000      0.500000000      0.500000000
11     0.000000000      0.000000000      0.500000000
12     0.000000000      0.500000000      0.000000000
13     0.500000000      0.000000000      0.000000000
14     0.712027013      0.712027013      0.712027013
15     0.287972987      0.287972987      0.287972987

```

LISTING C.3: POSCAR

```

1 Automatic mesh
2 0          ! number of k-points = 0 -> automatic generation
   scheme
3 Auto      ! fully automatic
4 81        ! length (R_k)

```

LISTING C.4: KPOINTS

3. Ru₃Sn₂S₂ SG:166

```

1 Ru3Sn2S2
2      1.000000000000000
3      5.5943530045331249      0.0242279878672557      0.0173684473718857
4      2.6671092955125482      4.9177129434794882      0.0173684312022582
5      2.6671086558695678      1.5954438740807757      4.6517485378620416
6      Sn      S      Ru
7      2      2      3
8 Direct
9      0.9999993440000026      0.9999993440000026      0.9999993440000026
10     0.5000024440000033      0.5000024440000033      0.5000024440000033
11     0.7128585758064708      0.7128585758063153      0.7128585758064709
12     0.2871409771935312      0.2871409771936869      0.2871409771935312
13     0.4999994040000004      0.9999995829999975      0.9999995829999975
14     0.9999995829999975      0.9999995829999975      0.4999994040000004
15     0.9999995829999975      0.4999994040000004      0.9999995829999975
16
17     0.00000000E+00      0.00000000E+00      0.00000000E+00
18     0.00000000E+00      0.00000000E+00      0.00000000E+00
19     0.00000000E+00      0.00000000E+00      0.00000000E+00
20     0.00000000E+00      0.00000000E+00      0.00000000E+00
21     0.00000000E+00      0.00000000E+00      0.00000000E+00
22     0.00000000E+00      0.00000000E+00      0.00000000E+00
23     0.00000000E+00      0.00000000E+00      0.00000000E+00

```

LISTING C.5: POSCAR

```

1 Automatic mesh
2 0          ! number of k-points = 0 -> automatic generation
   scheme
3 Auto      ! fully automatic
4 81        ! length (R_k)

```

LISTING C.6: KPOINTS

4. Co₂S₃ SG:167

```

1 Co4 S6
2 1.0
3      6.0118894577      0.0000000000      0.0000000000
4      3.3072939034      5.0204204892      0.0000000000
5      3.3072939034      1.7817018330      4.6936297752
6      Co      S
7      4      6
8 Direct
9      0.850109994      0.850109994      0.850109994
10     0.649890006      0.649890006      0.649890006
11     0.350109994      0.350109994      0.350109994
12     0.149890006      0.149890006      0.149890006
13     0.250000000      0.947170019      0.552829981
14     0.552829981      0.250000000      0.947170019
15     0.947170019      0.552829981      0.250000000
16     0.052829999      0.447169989      0.750000000
17     0.447169989      0.750000000      0.052829999
18     0.750000000      0.052829999      0.447169989

```

LISTING C.7: POSCAR

```

1 Automatic mesh
2 0          ! number of k-points = 0 -> automatic generation
   scheme
3 Auto      ! fully automatic
4 21        ! length (R_k)

```

LISTING C.8: KPOINTS

5. Co₂S₃ SG:141

```

1 Co16 S24
2 1.0
3      14.6876535416      0.0000000000      0.0000000000
4      11.7415412457      8.8240226502      0.0000000000
5      -13.2145969640      -4.4120111816      4.6514246172
6      Co      S

```

```

7      16      24
8 Direct
9      0.667783976      0.667783976      0.000000000
10     0.332215995      0.332215995      0.000000000
11     0.040266000      0.792486012      0.247779995
12     0.417784005      0.917783976      0.500000000
13     0.542486012      0.290266007      0.747780025
14     0.709734023      0.457513988      0.252220005
15     0.082216002      0.582216024      0.500000000
16     0.207514003      0.959734023      0.752219975
17     0.542486012      0.794705987      0.252220005
18     0.875000000      0.125000000      0.750000000
19     0.375000000      0.125000000      0.250000000
20     0.875000000      0.625000000      0.750000000
21     0.207514003      0.455294013      0.247779995
22     0.544705987      0.792486012      0.752219975
23     0.875000000      0.125000000      0.250000000
24     0.205293998      0.457513988      0.747780025
25     0.108190998      0.873107016      0.235083997
26     0.461510003      0.221056998      0.759546995
27     0.778943002      0.538489997      0.240453005
28     0.111977004      0.376893014      0.735083997
29     0.461510003      0.701963007      0.240453005
30     0.623107016      0.888023019      0.264916003
31     0.126892999      0.891808987      0.764916003
32     0.433550000      0.205409497      0.228140503
33     0.772731006      0.044590499      0.728140473
34     0.977268994      0.205409497      0.771859527
35     0.126892999      0.361977011      0.235083997
36     0.623107016      0.358191013      0.735083997
37     0.288489997      0.548036993      0.259546995
38     0.794590473      0.566450000      0.771859527
39     0.971056998      0.711510003      0.259546995
40     0.451963007      0.711510003      0.740453005
41     0.638023019      0.873107016      0.764916003
42     0.794590473      0.022731001      0.228140503
43     0.288489997      0.028943000      0.740453005
44     0.955409527      0.227268994      0.271859497
45     0.641808987      0.376893014      0.264916003
46     0.298036993      0.538489997      0.759546995
47     0.955409527      0.683550000      0.728140473
48     0.316450000      0.044590499      0.271859497

```

LISTING C.9: POSCAR

```

1 Automatic mesh

```

```

2 0          ! number of k-points = 0 -> automatic generation
   scheme
3 Auto      ! fully automatic
4 45        ! length (R_k)

```

LISTING C.10: KPOINTS

6. Co₃S SG:194

```

1 Co6 S2
2 1.0
3      5.1544442177      0.0000000000      0.0000000000
4      -2.5772221088      4.4638796349      0.0000000000
5      0.0000000000      0.0000000000      3.9230320454
6      Co      S
7      6      2
8 Direct
9      0.335711002      0.167855501      0.750000000
10     0.832144499      0.167855501      0.750000000
11     0.832144499      0.664288998      0.750000000
12     0.664288998      0.832144499      0.250000000
13     0.167855501      0.832144499      0.250000000
14     0.167855501      0.335711002      0.250000000
15     0.666666687      0.333333343      0.250000000
16     0.333333343      0.666666687      0.750000000

```

LISTING C.11: POSCAR

```

1 Automatic mesh
2 0          ! number of k-points = 0 -> automatic generation
   scheme
3 Auto      ! fully automatic
4 81        ! length (R_k)

```

LISTING C.12: KPOINTS

7. Co₃S₄ SG:227

```

1 Co6 S8
2 1.0
3      6.5725970268      0.0000000000      0.0000000000
4      3.2862985134      5.6920359941      0.0000000000
5      3.2862985134      1.8973453314      5.3665030002
6      Co      S
7      6      8
8 Direct
9      0.125000000      0.125000000      0.125000000

```

```

10      0.625000000      0.125000000      0.125000000
11      0.125000000      0.125000000      0.625000000
12      0.125000000      0.625000000      0.125000000
13      0.500000000      0.500000000      0.500000000
14      0.750000000      0.750000000      0.750000000
15      0.882149339      0.353552014      0.882149339
16      0.367850661      0.367850661      0.896448016
17      0.367850661      0.367850661      0.367850661
18      0.896448016      0.367850661      0.367850661
19      0.882149339      0.882149339      0.882149339
20      0.353552014      0.882149339      0.882149339
21      0.367850661      0.896448016      0.367850661
22      0.882149339      0.882149339      0.353552014

```

LISTING C.13: POSCAR

```

1 Automatic mesh
2 0          ! number of k-points = 0 -> automatic generation
   scheme
3 Auto      ! fully automatic
4 21        ! length (R_k)

```

LISTING C.14: KPOINTS

8. Co₉S₈ SG:225

```

1 Co9 S8
2 1.0
3      6.9328312874      0.0000000000      0.0000000000
4      3.4664156437      6.0040080150      0.0000000000
5      3.4664156437      2.0013360050      5.6606330423
6      Co      S
7      9      8
8 Direct
9      0.620416999      0.126527667      0.126527667
10     0.126527667      0.126527667      0.126527667
11     0.873472333      0.873472333      0.873472333
12     0.379583001      0.873472333      0.873472333
13     0.873472333      0.379583001      0.873472333
14     0.500000000      0.500000000      0.500000000
15     0.873472333      0.873472333      0.379583001
16     0.126527667      0.126527667      0.620416999
17     0.126527667      0.620416999      0.126527667
18     0.261343986      0.738655984      0.261343986
19     0.738655984      0.261343986      0.738655984
20     0.261343986      0.261343986      0.738655984

```

```

21      0.738655984      0.738655984      0.261343986
22      0.738655984      0.261343986      0.261343986
23      0.261343986      0.738655984      0.738655984
24      0.750000000      0.750000000      0.750000000
25      0.250000000      0.250000000      0.250000000

```

LISTING C.15: POSCAR

```

1 Automatic mesh
2 0          ! number of k-points = 0 -> automatic generation
   scheme
3 Auto      ! fully automatic
4 20       ! length (R_k)

```

LISTING C.16: KPOINTS

9. CoS SG:129

```

1 Co2 S2
2 1.0
3      3.6330139637      0.0000000000      0.0000000000
4      0.0000000000      3.6330139637      0.0000000000
5      0.0000000000      0.0000000000      5.1794638634
6 Co      S
7 2      2
8 Direct
9      0.000000000      0.000000000      0.000000000
10     0.500000000      0.500000000      0.000000000
11     0.500000000      0.000000000      0.765447021
12     0.000000000      0.500000000      0.234552994

```

LISTING C.17: POSCAR

```

1 Automatic mesh
2 0          ! number of k-points = 0 -> automatic generation
   scheme
3 Auto      ! fully automatic
4 45       ! length (R_k)

```

LISTING C.18: KPOINTS

10. CoS SG:194

```

1 Co2 S2
2 1.0
3      3.3466298580      0.0000000000      0.0000000000
4     -1.6733149290      2.8982664741      0.0000000000

```

```

5      0.0000000000      0.0000000000      5.1387758255
6      Co      S
7      2      2
8 Direct
9      0.0000000000      0.0000000000      0.5000000000
10     0.0000000000      0.0000000000      0.0000000000
11     0.666666687      0.333333343      0.7500000000
12     0.333333343      0.666666687      0.2500000000

```

LISTING C.19: POSCAR

```

1 Automatic mesh
2 0          ! number of k-points = 0 -> automatic generation
   scheme
3 Auto          ! fully automatic
4 201         ! length (R_k)

```

LISTING C.20: KPOINTS

11. CoS₂ SG:205

```

1 Co4 S8
2 1.0
3      5.5064010620      0.0000000000      0.0000000000
4      0.0000000000      5.5064010620      0.0000000000
5      0.0000000000      0.0000000000      5.5064010620
6      Co      S
7      4      8
8 Direct
9      0.0000000000      0.5000000000      0.5000000000
10     0.5000000000      0.5000000000      0.0000000000
11     0.5000000000      0.0000000000      0.5000000000
12     0.0000000000      0.0000000000      0.0000000000
13     0.387892991      0.112107001      0.887893021
14     0.112107001      0.887893021      0.387892991
15     0.887893021      0.387892991      0.112107001
16     0.612106979      0.612106979      0.612106979
17     0.387892991      0.387892991      0.387892991
18     0.112107001      0.612106979      0.887893021
19     0.887893021      0.112107001      0.612106979
20     0.612106979      0.887893021      0.112107001

```

LISTING C.21: POSCAR

```

1 Automatic mesh
2 0          ! number of k-points = 0 -> automatic generation
   scheme

```

```

3 Auto          ! fully automatic
4 20            ! length (R_k)

```

LISTING C.22: KPOINTS

12. CoS₂ SG:61

```

1 Co4 S8
2 1.0
3      5.4443769455      0.0000000000      0.0000000000
4      0.0000000000      5.5394768715      0.0000000000
5      0.0000000000      0.0000000000      5.5684838295
6 Co      S
7 4      8
8 Direct
9      0.000000000      0.500000000      0.500000000
10     0.000000000      0.000000000      0.000000000
11     0.500000000      0.000000000      0.500000000
12     0.500000000      0.500000000      0.000000000
13     0.386853009      0.388734996      0.388045013
14     0.386853009      0.888734996      0.111955002
15     0.886852980      0.611265004      0.111955002
16     0.113146998      0.888734996      0.611954987
17     0.613147020      0.111265004      0.888045013
18     0.113146998      0.388734996      0.888045013
19     0.886852980      0.111265004      0.388045013
20     0.613147020      0.611265004      0.611954987

```

LISTING C.23: POSCAR

```

1 Automatic mesh
2 0          ! number of k-points = 0 -> automatic generation
   scheme
3 Auto          ! fully automatic
4 81           ! length (R_k)

```

LISTING C.24: KPOINTS

13. CoS₂ SG:227

```

1 Co4 S8
2 1.0
3      6.5830879211      0.0000000000      0.0000000000
4      3.2915439606      5.7011213751      0.0000000000
5      3.2915439606      1.9003737917      5.3750687796
6 Co      S
7 4      8

```

```

8 Direct
9      0.625000000      0.625000000      0.125000000
10     0.625000000      0.125000000      0.625000000
11     0.125000000      0.625000000      0.625000000
12     0.625000000      0.625000000      0.625000000
13     0.865020990      0.865020990      0.865020990
14     0.845062971      0.384979010      0.384979010
15     0.384979010      0.384979010      0.845062971
16     0.384979010      0.845062971      0.384979010
17     0.384979010      0.384979010      0.384979010
18     0.404936999      0.865020990      0.865020990
19     0.865020990      0.404936999      0.865020990
20     0.865020990      0.865020990      0.404936999

```

LISTING C.25: POSCAR

```

1 Automatic mesh
2 0          ! number of k-points = 0 -> automatic generation
   scheme
3 Auto      ! fully automatic
4 15        ! length (R_k)

```

LISTING C.26: KPOINTS

14. CoS₂ SG:166

```

1 Co1 S2
2 1.0
3      7.3379764557      0.0000000000      0.0000000000
4      6.6359885486      3.1320208249      0.0000000000
5      6.6359885486      1.4873412322      2.7563328004
6      Co      S
7      1      2
8 Direct
9      0.000000000      0.000000000      0.000000000
10     0.607073009      0.607073009      0.607073009
11     0.392926991      0.392926991      0.392926991

```

LISTING C.27: POSCAR

```

1 Automatic mesh
2 0          ! number of k-points = 0 -> automatic generation
   scheme
3 Auto      ! fully automatic
4 100       ! length (R_k)

```

LISTING C.28: KPOINTS

15. CoS₂ SG:122

```

1 Co2 S4
2 1.0
3      6.0429410934      0.0000000000      0.0000000000
4      1.7603977797      5.7808422151      0.0000000000
5      -3.9016694822     -2.8904211414      3.5971624839
6      Co      S
7      2      4
8 Direct
9      0.750000000      0.250000000      0.500000000
10     0.000000000      0.000000000      0.000000000
11     0.875000000      0.907065988      0.532065988
12     0.092933998      0.625000000      0.967934012
13     0.375000000      0.342934012      0.467934012
14     0.657065988      0.125000000      0.032065999

```

LISTING C.29: POSCAR

```

1 Automatic mesh
2 0      ! number of k-points = 0 -> automatic generation
      scheme
3 Auto      ! fully automatic
4 20      ! length (R_k)

```

LISTING C.30: KPOINTS

16. Co₂Sn SG:194

```

1 Co4 Sn2
2 1.0
3      4.2726902962      0.0000000000      0.0000000000
4      -2.1363451481     3.7002583390      0.0000000000
5      0.0000000000      0.0000000000      5.2338519096
6      Co      Sn
7      4      2
8 Direct
9      0.666666687      0.333333343      0.250000000
10     0.000000000      0.000000000      0.500000000
11     0.000000000      0.000000000      0.000000000
12     0.333333343      0.666666687      0.750000000
13     0.333333343      0.666666687      0.250000000
14     0.666666687      0.333333343      0.750000000

```

LISTING C.31: POSCAR

```

1 Automatic mesh

```

```

2 0          ! number of k-points = 0 -> automatic generation
   scheme
3 Auto      ! fully automatic
4 81        ! length (R_k)

```

LISTING C.32: KPOINTS

17. Co₃Sn SG:194

```

1 Co6 Sn2
2 1.0
3      5.3193836212      0.0000000000      0.0000000000
4      -2.6596918106      4.6067213484      0.0000000000
5      0.0000000000      0.0000000000      4.2312479019
6      Co   Sn
7      6    2
8 Direct
9      0.315975994      0.157987997      0.750000000
10     0.842011988      0.157987997      0.750000000
11     0.842011988      0.684023976      0.750000000
12     0.684023976      0.842011988      0.250000000
13     0.157987997      0.842011988      0.250000000
14     0.157987997      0.315975994      0.250000000
15     0.666666687      0.333333343      0.250000000
16     0.333333343      0.666666687      0.750000000

```

LISTING C.33: POSCAR

```

1 Automatic mesh
2 0          ! number of k-points = 0 -> automatic generation
   scheme
3 Auto      ! fully automatic
4 30        ! length (R_k)

```

LISTING C.34: KPOINTS

18. Co₃Sn₂ SG:62

```

1 sm_isp_SD1823856-standardized_unitcell
2 1.0
3      7.0739998817      0.0000000000      0.0000000000
4      0.0000000000      5.2109999657      0.0000000000
5      0.0000000000      0.0000000000      8.1979999542
6      Co   Sn
7      12   8
8 Direct
9      0.235300004      0.004000000      0.382400006

```

```

10 0.764699996 0.995999992 0.617599964
11 0.264699996 0.995999992 0.882400036
12 0.735300004 0.004000000 0.117599994
13 0.764699996 0.504000008 0.617599964
14 0.235300004 0.495999992 0.382400006
15 0.735300004 0.495999992 0.117599994
16 0.264699996 0.504000008 0.882400036
17 0.407700002 0.250000000 0.128399998
18 0.592299998 0.750000000 0.871600032
19 0.092299998 0.750000000 0.628399968
20 0.907700002 0.250000000 0.371600002
21 0.065700002 0.250000000 0.094200000
22 0.934300005 0.750000000 0.905799985
23 0.434300005 0.750000000 0.594200015
24 0.565699995 0.250000000 0.405799985
25 0.102200001 0.250000000 0.641700029
26 0.897799969 0.750000000 0.358299971
27 0.397799999 0.750000000 0.141700029
28 0.602200031 0.250000000 0.858299971

```

LISTING C.35: POSCAR

```

1 Automatic mesh
2 0 ! number of k-points = 0 -> automatic generation
   scheme
3 Auto ! fully automatic
4 15 ! length (R_k)

```

LISTING C.36: KPOINTS

19. CoSn SG:191

```

1 Co3 Sn3
2 1.0
3 5.3085703850 0.000000000 0.000000000
4 -2.6542851925 4.5973568112 0.000000000
5 0.0000000000 0.000000000 4.2374081612
6 Co Sn
7 3 3
8 Direct
9 0.500000000 0.500000000 0.000000000
10 0.500000000 0.000000000 0.000000000
11 0.000000000 0.500000000 0.000000000
12 0.333333343 0.666666687 0.500000000
13 0.666666687 0.333333343 0.500000000

```

```
14      0.000000000      0.000000000      0.000000000
```

LISTING C.37: POSCAR

```
1 Automatic mesh
2 0          ! number of k-points = 0 -> automatic generation
   scheme
3 Auto      ! fully automatic
4 201      ! length (R_k)
```

LISTING C.38: KPOINTS

20. CoSn₂ SG:140

```
1 Co2 Sn4
2 1.0
3      5.2757601738      0.0000000000      0.0000000000
4      -2.4391564360      4.6780510143      0.0000000000
5      -1.4183016423      -2.3390251334      4.5112112883
6      Co      Sn
7      2      4
8 Direct
9      0.750000000      0.750000000      0.000000000
10     0.250000000      0.250000000      0.000000000
11     0.166150004      0.666149974      0.832300007
12     0.833850026      0.333849996      0.167699993
13     0.666149974      0.833850026      0.500000000
14     0.333849996      0.166150004      0.500000000
```

LISTING C.39: POSCAR

```
1 Automatic mesh
2 0          ! number of k-points = 0 -> automatic generation
   scheme
3 Auto      ! fully automatic
4 20        ! length (R_k)
```

LISTING C.40: KPOINTS

21. CoSn₃ SG:142

```
1 Co8 Sn24
2 1.0
3      17.6207313538      0.0000000000      0.0000000000
4      15.3674583353      8.6215658528      0.0000000000
5      -16.4940942266      -4.3107827649      4.4555786423
6      Co      Sn
```

```

7      8      24
8 Direct
9      0.460150987      0.460150987      0.000000000
10     0.789848983      0.289849013      0.500000000
11     0.039848998      0.039848998      0.000000000
12     0.210151002      0.710151017      0.500000000
13     0.289849013      0.789848983      0.500000000
14     0.960151017      0.960151017      0.000000000
15     0.710151017      0.210151002      0.500000000
16     0.539848983      0.539848983      0.000000000
17     0.414586514      0.414586514      0.329172999
18     0.085413501      0.085413501      0.670826972
19     0.835413516      0.664586484      0.500000000
20     0.164586499      0.335413486      0.500000000
21     0.335413486      0.835413516      0.170827001
22     0.664586484      0.164586499      0.829173028
23     0.914586484      0.585413516      0.000000000
24     0.585413516      0.914586484      0.000000000
25     0.985180974      0.347562999      0.998035014
26     0.349528015      0.987146020      0.001965000
27     0.264818996      0.762853980      0.862381995
28     0.900471985      0.402437001      0.137618005
29     0.152437001      0.514819026      0.001965000
30     0.512853980      0.150472000      0.998035014
31     0.737146020      0.235181004      0.137618005
32     0.097562999      0.599528015      0.862381995
33     0.764819026      0.902436972      0.501964986
34     0.400471985      0.262854010      0.498035014
35     0.485181004      0.487145990      0.637618005
36     0.849528015      0.847563028      0.362381995
37     0.597563028      0.735180974      0.498035014
38     0.237146005      0.099528000      0.501964986
39     0.012854000      0.014819000      0.362381995
40     0.652436972      0.650471985      0.637618005

```

LISTING C.41: POSCAR

```

1 Automatic mesh
2 0          ! number of k-points = 0 -> automatic generation
   scheme
3 Auto      ! fully automatic
4 15       ! length (R_k)

```

LISTING C.42: KPOINTS

22. CoSn₃ SG:64

```

1 Co4 Sn12
2 1.0
3      9.0951910019      0.0000000000      0.0000000000
4      -6.9085408801      5.9156201931      0.0000000000
5      0.0000000000      0.0000000000      6.3232312202
6      Co      Sn
7      4      12
8 Direct
9      0.579506993      0.420493007      0.500000000
10     0.079507001      0.920493007      0.000000000
11     0.420493007      0.579506993      0.500000000
12     0.920493007      0.079507001      0.000000000
13     0.163996994      0.163996994      0.336380988
14     0.663996994      0.663996994      0.163618997
15     0.336003006      0.336003006      0.836381018
16     0.836003006      0.836003006      0.663618982
17     0.981868029      0.651794016      0.317829013
18     0.481867999      0.151794001      0.182171002
19     0.848205984      0.518131971      0.817829013
20     0.348206013      0.018131999      0.682170987
21     0.651794016      0.981868029      0.317829013
22     0.151794001      0.481867999      0.182171002
23     0.518131971      0.848205984      0.817829013
24     0.018131999      0.348206013      0.682170987

```

LISTING C.43: POSCAR

```

1 Automatic mesh
2 0          ! number of k-points = 0 -> automatic generation
   scheme
3 Auto      ! fully automatic
4 201      ! length (R_k)

```

LISTING C.44: KPOINTS

23. RhS₂ SG:205

```

1 Rh S2
2 1.0
3      5.5850000381      0.0000000000      0.0000000000
4      0.0000000000      5.5850000381      0.0000000000
5      0.0000000000      0.0000000000      5.5850000381
6      S      Rh
7      8      4
8 Direct
9      0.379999995      0.379999995      0.379999995

```

```

10 0.620000005      0.620000005      0.620000005
11 0.120000005      0.620000005      0.879999995
12 0.879999995      0.379999995      0.120000005
13 0.620000005      0.879999995      0.120000005
14 0.379999995      0.120000005      0.879999995
15 0.879999995      0.120000005      0.620000005
16 0.120000005      0.879999995      0.379999995
17 0.000000000      0.000000000      0.000000000
18 0.500000000      0.000000000      0.500000000
19 0.000000000      0.500000000      0.500000000
20 0.500000000      0.500000000      0.000000000

```

LISTING C.45: POSCAR

```

1 Automatic mesh
2 0          ! number of k-points = 0 -> automatic generation
   scheme
3 Auto      ! fully automatic
4 15        ! length (R_k)

```

LISTING C.46: KPOINTS

24. Rh₃S₄ SG:12

```

1 Rh9 S12
2 1.0
3 7.5629401207      0.0000000000      0.0000000000
4 0.2940345808      7.5572221705      0.0000000000
5 -1.3467559863     1.4001742273      6.0132099924
6 Rh S
7 9 12
8 Direct
9 0.839147985      0.839147985      0.000000000
10 0.160852000     0.160852000     0.000000000
11 0.000000000     0.000000000     0.500000000
12 0.650049984     0.349949986     0.947637022
13 0.349949986     0.650049984     0.052363001
14 0.215758994     0.491549999     0.450645000
15 0.491549999     0.215758994     0.549354970
16 0.784241021     0.508449972     0.549354970
17 0.508449972     0.784241021     0.450645000
18 0.141169995     0.440605015     0.100762002
19 0.440605015     0.141169995     0.899237990
20 0.858829975     0.559395015     0.899237990
21 0.559395015     0.858829975     0.100762002
22 0.882741988     0.117257997     0.111671001

```

```

23      0.117257997      0.882741988      0.888329029
24      0.967047989      0.716165006      0.385664999
25      0.716165006      0.967047989      0.614335001
26      0.032951999      0.283834994      0.614335001
27      0.415872008      0.584128022      0.726453006
28      0.584128022      0.415872008      0.273546994
29      0.283834994      0.032951999      0.385664999

```

LISTING C.47: POSCAR

```

1 Automatic mesh
2 0          ! number of k-points = 0 -> automatic generation
   scheme
3 Auto      ! fully automatic
4 81        ! length (R_k)

```

LISTING C.48: KPOINTS

25. Rh₂S₃ SG:60

```

1 Rh2 S3
2 1.0
3      8.4619998932      0.0000000000      0.0000000000
4      0.0000000000      5.9850001335      0.0000000000
5      0.0000000000      0.0000000000      6.1380000114
6 Rh S
7 8 12
8 Direct
9      0.106449999      0.251700014      0.033799998
10     0.893549979      0.748299956      0.966199994
11     0.393550009      0.248299986      0.533800006
12     0.606450021      0.751700044      0.466199994
13     0.893549979      0.251700014      0.466199994
14     0.106449999      0.748299956      0.533800006
15     0.606450021      0.248299986      0.966199994
16     0.393550009      0.751700044      0.033799998
17     0.151800007      0.390599996      0.393000007
18     0.848199964      0.609400034      0.606999993
19     0.348199993      0.109400004      0.893000007
20     0.651800036      0.890599966      0.106999993
21     0.848199964      0.390599996      0.106999993
22     0.151800007      0.609400034      0.893000007
23     0.651800036      0.109400004      0.606999993
24     0.348199993      0.890599966      0.393000007
25     0.000000000      0.952499986      0.250000000
26     0.000000000      0.047500014      0.750000000

```

27	0.500000000	0.547500014	0.750000000
28	0.500000000	0.452499986	0.250000000

LISTING C.49: POSCAR

```

1 Automatic mesh
2 0          ! number of k-points = 0 -> automatic generation
   scheme
3 Auto      ! fully automatic
4 15        ! length (R_k)
    
```

LISTING C.50: KPOINTS

26. Rh₁₇S₁₅ SG:221

```

1 Rh34 S30
2 1.0
3      10.0192050934      0.0000000000      0.0000000000
4      0.0000000000      10.0192050934      0.0000000000
5      0.0000000000      0.0000000000      10.0192050934
6 Rh      S
7 34      30
8 Direct
9      0.357299000      0.357299000      0.142369002
10     0.357299000      0.857631028      0.357299000
11     0.357299000      0.142369002      0.642701030
12     0.142369002      0.357299000      0.642701030
13     0.857631028      0.357299000      0.357299000
14     0.642701030      0.357299000      0.142369002
15     0.357299000      0.642701030      0.142369002
16     0.142369002      0.357299000      0.357299000
17     0.357299000      0.142369002      0.357299000
18     0.642701030      0.857631028      0.357299000
19     0.142369002      0.642701030      0.642701030
20     0.642701030      0.142369002      0.642701030
21     0.857631028      0.642701030      0.357299000
22     0.857631028      0.357299000      0.642701030
23     0.357299000      0.857631028      0.642701030
24     0.357299000      0.642701030      0.857631028
25     0.642701030      0.357299000      0.857631028
26     0.642701030      0.642701030      0.142369002
27     0.357299000      0.357299000      0.857631028
28     0.642701030      0.642701030      0.857631028
29     0.142369002      0.642701030      0.357299000
30     0.857631028      0.642701030      0.642701030
31     0.642701030      0.142369002      0.357299000
    
```

32	0.642701030	0.857631028	0.642701030
33	0.000000000	0.238578007	0.000000000
34	0.000000000	0.000000000	0.238578007
35	0.000000000	0.000000000	0.761421978
36	0.761421978	0.000000000	0.000000000
37	0.238578007	0.000000000	0.000000000
38	0.000000000	0.761421978	0.000000000
39	0.000000000	0.500000000	0.000000000
40	0.000000000	0.000000000	0.500000000
41	0.500000000	0.000000000	0.000000000
42	0.500000000	0.500000000	0.500000000
43	0.169607997	0.500000000	0.169607997
44	0.169607997	0.830392003	0.500000000
45	0.169607997	0.169607997	0.500000000
46	0.169607997	0.500000000	0.830392003
47	0.830392003	0.500000000	0.169607997
48	0.500000000	0.169607997	0.169607997
49	0.500000000	0.830392003	0.169607997
50	0.500000000	0.169607997	0.830392003
51	0.830392003	0.830392003	0.500000000
52	0.830392003	0.169607997	0.500000000
53	0.500000000	0.830392003	0.830392003
54	0.830392003	0.500000000	0.830392003
55	0.229337007	0.229337007	0.000000000
56	0.229337007	0.000000000	0.229337007
57	0.229337007	0.000000000	0.770663023
58	0.000000000	0.229337007	0.770663023
59	0.000000000	0.229337007	0.229337007
60	0.770663023	0.229337007	0.000000000
61	0.229337007	0.770663023	0.000000000
62	0.770663023	0.000000000	0.229337007
63	0.000000000	0.770663023	0.770663023
64	0.770663023	0.000000000	0.770663023
65	0.000000000	0.770663023	0.229337007
66	0.770663023	0.770663023	0.000000000
67	0.500000000	0.500000000	0.262796998
68	0.500000000	0.737203002	0.500000000
69	0.500000000	0.262796998	0.500000000
70	0.262796998	0.500000000	0.500000000
71	0.737203002	0.500000000	0.500000000
72	0.500000000	0.500000000	0.737203002

LISTING C.51: POSCAR

1 Automatic mesh

```

2 0          ! number of k-points = 0 -> automatic generation
   scheme
3 Auto      ! fully automatic
4 15       ! length (R_k)

```

LISTING C.52: KPOINTS

27. RhSn SG:198

```

1 Rh Sn
2 1.0
3      4.3400001526      0.0000000000      0.0000000000
4      -2.1700000763      3.7585503846      0.0000000000
5      0.0000000000      0.0000000000      5.5549998283
6 Rh Sn
7 2 2
8 Direct
9      0.0000000000      0.0000000000      0.0000000000
10     0.0000000000      0.0000000000      0.5000000000
11     0.333333343      0.666666687      0.2500000000
12     0.666666627      0.333333313      0.7500000000

```

LISTING C.53: POSCAR

```

1 Automatic mesh
2 0          ! number of k-points = 0 -> automatic generation
   scheme
3 Auto      ! fully automatic
4 15       ! length (R_k)

```

LISTING C.54: KPOINTS

28. RhSn₂ SG:64

```

1 Sn8 Rh4
2 1.0
3      6.9980859756      0.0000000000      0.0000000000
4      -4.0568327971      5.7022201798      0.0000000000
5      0.0000000000      0.0000000000      6.4102950096
6 Sn Rh
7 8 4
8 Direct
9      0.335864007      0.335864007      0.836606979
10     0.664135993      0.664135993      0.163393006
11     0.835864007      0.835864007      0.663393021
12     0.164136007      0.164136007      0.336607009
13     0.497049987      0.997049987      0.750000000

```

```

14      0.002950000      0.502950013      0.250000000
15      0.997049987      0.497049987      0.750000000
16      0.502950013      0.002950000      0.250000000
17      0.617645979      0.382353991      0.500000000
18      0.117646001      0.882354021      0.000000000
19      0.382353991      0.617645979      0.500000000
20      0.882354021      0.117646001      0.000000000

```

LISTING C.55: POSCAR

```

1 Automatic mesh
2 0          ! number of k-points = 0 -> automatic generation
   scheme
3 Auto      ! fully automatic
4 54        ! length (R_k)

```

LISTING C.56: KPOINTS

29. Rh₂Sn SG:62

```

1 Rh2 Sn
2 1.0
3      5.5199999809      0.0000000000      0.0000000000
4      0.0000000000      4.2210001945      0.0000000000
5      0.0000000000      0.0000000000      8.2089996338
6 Rh Sn
7 8 4
8 Direct
9      0.039999999      0.250000000      0.209999993
10     0.959999979      0.750000000      0.790000021
11     0.460000008      0.750000000      0.709999979
12     0.540000021      0.250000000      0.290000021
13     0.170000002      0.250000000      0.569999993
14     0.829999983      0.750000000      0.430000007
15     0.329999983      0.750000000      0.069999993
16     0.670000017      0.250000000      0.930000007
17     0.709999979      0.250000000      0.610000014
18     0.290000021      0.750000000      0.389999986
19     0.790000021      0.750000000      0.110000014
20     0.209999979      0.250000000      0.889999986

```

LISTING C.57: POSCAR

```

1 Automatic mesh
2 0          ! number of k-points = 0 -> automatic generation
   scheme

```

```
3 Auto          ! fully automatic
4 15            ! length (R_k)
```

LISTING C.58: KPOINTS

30. RhSn₄ SG:142

```
1 Sn16 Rh4
2 1.0
3      12.5533351898      0.0000000000      0.0000000000
4      9.2875833435       8.4455325484      0.0000000000
5     -10.9204596252     -4.2227664128      4.5274749900
6      Sn   Rh
7      16   4
8 Direct
9      0.137720004      0.636457026      0.147448003
10     0.637719989      0.490271986      0.501263022
11     0.886457026      0.887719989      0.647448003
12     0.386456996      0.739009023      0.998736978
13     0.612280011      0.613542974      0.352551997
14     0.112279996      0.759728014      0.998736978
15     0.863542974      0.362280011      0.852551997
16     0.363543004      0.510990977      0.501263022
17     0.989009023      0.136456996      0.498737007
18     0.489008993      0.990271986      0.852551997
19     0.740271986      0.387719989      0.001263000
20     0.240272000      0.239008993      0.352551997
21     0.760990977      0.113542996      0.001263000
22     0.260991007      0.259728014      0.647448003
23     0.009728000      0.862280011      0.498737007
24     0.509728014      0.010991000      0.147448003
25     0.750000000      0.750000000      0.000000000
26     0.250000000      0.250000000      0.000000000
27     0.000000000      0.500000000      0.500000000
28     0.500000000      0.000000000      0.500000000
```

LISTING C.59: POSCAR

```
1 Automatic mesh
2 0          ! number of k-points = 0 -> automatic generation
   scheme
3 Auto      ! fully automatic
4 81        ! length (R_k)
```

LISTING C.60: KPOINTS

31. RhSn₂ SG:140

```

1 Rh Sn2
2 1.0000000000000000
3 6.3559708548761247 0.0000000000000000 -0.0000000000000000
4 0.0000000000000000 6.3559708548761247 0.0000000000000000
5 0.0000000000000000 0.0000000000000000 5.7525666014918784
6 Sn Rh
7 8 4
8 Direct
9 0.1603802775740230 0.6603802625740181 0.0000000000000000
10 0.8396197374259819 0.3396197374259818 -0.0000000000000000
11 0.3396197374259818 0.1603802775740230 0.0000000000000000
12 0.6603802625740181 0.8396197374259819 -0.0000000000000000
13 0.8396197374259819 0.6603802625740181 0.5000000000000000
14 0.1603802775740230 0.3396197374259818 0.5000000000000000
15 0.6603802625740181 0.1603802775740230 0.5000000000000000
16 0.3396197374259818 0.8396197374259819 0.5000000000000000
17 0.0000000000000000 0.0000000000000000 0.2500000000000000
18 0.0000000000000000 0.0000000000000000 0.7500000000000000
19 0.5000000000000000 0.5000000000000000 0.7500000000000000
20 0.5000000000000000 0.5000000000000000 0.2500000000000000
21
22 0.00000000E+00 0.00000000E+00 0.00000000E+00
23 0.00000000E+00 0.00000000E+00 0.00000000E+00
24 0.00000000E+00 0.00000000E+00 0.00000000E+00
25 0.00000000E+00 0.00000000E+00 0.00000000E+00
26 0.00000000E+00 0.00000000E+00 0.00000000E+00
27 0.00000000E+00 0.00000000E+00 0.00000000E+00
28 0.00000000E+00 0.00000000E+00 0.00000000E+00
29 0.00000000E+00 0.00000000E+00 0.00000000E+00
30 0.00000000E+00 0.00000000E+00 0.00000000E+00
31 0.00000000E+00 0.00000000E+00 0.00000000E+00
32 0.00000000E+00 0.00000000E+00 0.00000000E+00
33 0.00000000E+00 0.00000000E+00 0.00000000E+00

```

LISTING C.61: POSCAR

```

1 Automatic mesh
2 0 ! number of k-points = 0 -> automatic generation
   scheme
3 Auto ! fully automatic
4 81 ! length (R_k)

```

LISTING C.62: KPOINTS

32. RuS₂ SG:205

```

1 Ru S2
2 1.0
3      5.6105999947      0.0000000000      0.0000000000
4      0.0000000000      5.6105999947      0.0000000000
5      0.0000000000      0.0000000000      5.6105999947
6      Ru      S
7      4      8
8 Direct
9      0.000000000      0.000000000      0.000000000
10     0.500000000      0.000000000      0.500000000
11     0.000000000      0.500000000      0.500000000
12     0.500000000      0.500000000      0.000000000
13     0.388309985      0.388309985      0.388309985
14     0.611690044      0.611690044      0.611690044
15     0.111690015      0.611690044      0.888309956
16     0.888309956      0.388309985      0.111690015
17     0.611690044      0.888309956      0.111690015
18     0.388309985      0.111690015      0.888309956
19     0.888309956      0.111690015      0.611690044
20     0.111690015      0.888309956      0.388309985

```

LISTING C.63: POSCAR

```

1 Automatic mesh
2 0          ! number of k-points = 0 -> automatic generation
           scheme
3 Auto      ! fully automatic
4 31        ! length (R_k)

```

LISTING C.64: KPOINTS

33. RuSn₂ SG:140

```

1 Ru Sn2
2 1.0
3      6.3889999390      0.0000000000      0.0000000000
4      0.0000000000      6.3889999390      0.0000000000
5      0.0000000000      0.0000000000      5.6929998398
6      Sn      Ru
7      8      4
8 Direct
9      0.165000007      0.665000021      0.000000000
10     0.834999979      0.334999979      0.000000000
11     0.334999979      0.165000007      0.000000000
12     0.665000021      0.834999979      0.000000000

```

```

13      0.834999979      0.665000021      0.500000000
14      0.165000007      0.334999979      0.500000000
15      0.665000021      0.165000007      0.500000000
16      0.334999979      0.834999979      0.500000000
17      0.000000000      0.000000000      0.250000000
18      0.000000000      0.000000000      0.750000000
19      0.500000000      0.500000000      0.750000000
20      0.500000000      0.500000000      0.250000000

```

LISTING C.65: POSCAR

```

1 Automatic mesh
2 0          ! number of k-points = 0 -> automatic generation
   scheme
3 Auto      ! fully automatic
4 81        ! length (R_k)

```

LISTING C.66: KPOINTS

34. Ru₂Sn₃ SG:116

```

1 Ru2 Sn3
2 1.0
3      6.1719999313      0.0000000000      0.0000000000
4      0.0000000000      6.1719999313      0.0000000000
5      0.0000000000      0.0000000000      9.9149999619
6      Sn   Ru
7      12   8
8 Direct
9      0.177000001      0.177000001      0.750000000
10     0.823000014      0.823000014      0.750000000
11     0.177000001      0.823000014      0.250000000
12     0.823000014      0.177000001      0.250000000
13     0.216000006      0.344999999      0.082999997
14     0.783999979      0.654999971      0.082999997
15     0.344999999      0.783999979      0.916999996
16     0.654999971      0.216000006      0.916999996
17     0.216000006      0.654999971      0.583000004
18     0.783999979      0.344999999      0.583000004
19     0.344999999      0.216000006      0.416999996
20     0.654999971      0.783999979      0.416999996
21     0.000000000      0.500000000      0.375000000
22     0.500000000      0.000000000      0.625000000
23     0.000000000      0.500000000      0.875000000
24     0.500000000      0.000000000      0.125000000
25     0.000000000      0.000000000      0.000000000

```

26	0.000000000	0.000000000	0.500000000
27	0.500000000	0.500000000	0.250000000
28	0.500000000	0.500000000	0.750000000

LISTING C.67: POSCAR

```

1 Automatic mesh
2 0          ! number of k-points = 0 -> automatic generation
   scheme
3 Auto      ! fully automatic
4 81        ! length (R_k)

```

LISTING C.68: KPOINTS

35. Ru₃Sn₇ SG:229

```

1 Ru3 Sn7
2 1.0
3     9.3531999588      0.0000000000      0.0000000000
4     0.0000000000      9.3531999588      0.0000000000
5     0.0000000000      0.0000000000      9.3531999588
6 Ru   Sn
7 12  28
8 Direct
9     0.345129997      0.000000000      0.000000000
10    0.654870033      0.000000000      0.000000000
11    0.000000000      0.345129997      0.000000000
12    0.000000000      0.654870033      0.000000000
13    0.000000000      0.000000000      0.345129997
14    0.000000000      0.000000000      0.654870033
15    0.845129967      0.500000000      0.500000000
16    0.154870003      0.500000000      0.500000000
17    0.500000000      0.845129967      0.500000000
18    0.500000000      0.154870003      0.500000000
19    0.500000000      0.500000000      0.845129967
20    0.500000000      0.500000000      0.154870003
21    0.250000000      0.000000000      0.500000000
22    0.750000000      0.000000000      0.500000000
23    0.500000000      0.250000000      0.000000000
24    0.500000000      0.750000000      0.000000000
25    0.000000000      0.500000000      0.250000000
26    0.000000000      0.500000000      0.750000000
27    0.000000000      0.250000000      0.500000000
28    0.000000000      0.750000000      0.500000000
29    0.250000000      0.500000000      0.000000000
30    0.750000000      0.500000000      0.000000000

```

```

31 0.500000000 0.000000000 0.750000000
32 0.500000000 0.000000000 0.250000000
33 0.161100000 0.161100000 0.161100000
34 0.838899970 0.838899970 0.838899970
35 0.838899970 0.838899970 0.161100000
36 0.161100000 0.161100000 0.838899970
37 0.838899970 0.161100000 0.838899970
38 0.161100000 0.838899970 0.161100000
39 0.161100000 0.838899970 0.838899970
40 0.838899970 0.161100000 0.161100000
41 0.661100030 0.661100030 0.661100030
42 0.338900000 0.338900000 0.338900000
43 0.338900000 0.338900000 0.661100030
44 0.661100030 0.661100030 0.338900000
45 0.338900000 0.661100030 0.338900000
46 0.661100030 0.338900000 0.661100030
47 0.661100030 0.338900000 0.338900000
48 0.338900000 0.661100030 0.661100030

```

LISTING C.69: POSCAR

```

1 Automatic mesh
2 0 ! number of k-points = 0 -> automatic generation
   scheme
3 Auto ! fully automatic
4 81 ! length (R_k)

```

LISTING C.70: KPOINTS

36. SSn SG:62

```

1 Sn4 S4
2 1.0
3 4.0239720345 0.0000000000 0.0000000000
4 0.0000000000 4.4425110817 0.0000000000
5 0.0000000000 0.0000000000 11.4326524734
6 Sn S
7 4 4
8 Direct
9 0.250000000 0.373975992 0.621237993
10 0.750000000 0.626024008 0.378762007
11 0.750000000 0.873975992 0.878762007
12 0.250000000 0.126023993 0.121238001
13 0.250000000 0.019866999 0.349830002
14 0.750000000 0.980132997 0.650170028
15 0.750000000 0.519867003 0.150169998

```

16 0.250000000 0.480132997 0.849829972

LISTING C.71: POSCAR

```

1 Automatic mesh
2 0          ! number of k-points = 0 -> automatic generation
   scheme
3 Auto      ! fully automatic
4 30       ! length (R_k)
    
```

LISTING C.72: KPOINTS

37. SSn SG:63

```

1 Sn4 S4
2 1.0
3 4.1118800000000002 0.0000000000000000 0.0000000000000003
4 0.00000000000000019 11.7162539999999993 0.0000000000000007
5 0.00000000000000000 0.00000000000000000 4.1078960000000002
6 Sn S
7 4 4
8 direct
9 0.00000000000000000 0.12638900000000000 0.25000000000000000
   Sn2+
10 0.50000000000000000 0.37361100000000000 0.75000000000000000
   Sn2+
11 0.50000000000000000 0.62638900000000000 0.25000000000000000
   Sn2+
12 0.00000000000000000 0.87361100000000000 0.75000000000000000
   Sn2+
13 0.00000000000000000 0.34860300000000000 0.25000000000000000 S2
   -
14 0.50000000000000000 0.15139700000000000 0.75000000000000000 S2
   -
15 0.50000000000000000 0.84860300000000000 0.25000000000000000 S2
   -
16 0.00000000000000000 0.65139700000000000 0.75000000000000000 S2
   -
    
```

LISTING C.73: POSCAR

```

1 Automatic mesh
2 0          ! number of k-points = 0 -> automatic generation
   scheme
3 Auto      ! fully automatic
4 30       ! length (R_k)
    
```

LISTING C.74: KPOINTS

38. SSn SG:225

```

1 Sn4 S4
2 1.0
3 5.8519819999999996 0.0000000000000000 0.0000000000000004
4 0.0000000000000009 5.8519819999999996 0.0000000000000004
5 0.0000000000000000 0.0000000000000000 5.8519819999999996
6 Sn S
7 4 4
8 direct
9 0.5000000000000000 0.0000000000000000 0.0000000000000000
   Sn2+
10 0.5000000000000000 0.5000000000000000 0.5000000000000000
   Sn2+
11 0.0000000000000000 0.0000000000000000 0.5000000000000000
   Sn2+
12 0.0000000000000000 0.5000000000000000 0.0000000000000000
   Sn2+
13 0.0000000000000000 0.0000000000000000 0.0000000000000000 S2
   -
14 0.0000000000000000 0.5000000000000000 0.5000000000000000 S2
   -
15 0.5000000000000000 0.0000000000000000 0.5000000000000000 S2
   -
16 0.5000000000000000 0.5000000000000000 0.0000000000000000 S2
   -

```

LISTING C.75: POSCAR

```

1 Automatic mesh
2 0 ! number of k-points = 0 -> automatic generation
   scheme
3 Auto ! fully automatic
4 20 ! length (R_k)

```

LISTING C.76: KPOINTS

39. S₃Sn₂ SG:62

```

1 Sn8 S12
2 1.0
3 3.8015490000000001 0.0000000000000000 0.0000000000000002
4 0.0000000000000015 9.2717679999999998 0.0000000000000006
5 0.0000000000000000 0.0000000000000000 14.4304939999999995
6 Sn S
7 8 12
8 direct

```

```

9  0.7500000000000000  0.4685159999999999  0.8370599999999999
   Sn2+
10 0.2500000000000000  0.5314840000000001  0.1629400000000001
   Sn2+
11 0.7500000000000000  0.9685159999999999  0.6629400000000001
   Sn2+
12 0.2500000000000000  0.0314840000000001  0.3370599999999999
   Sn2+
13 0.7500000000000000  0.8402639999999999  0.0499039999999997
   Sn3+
14 0.2500000000000000  0.1597360000000001  0.9500960000000003
   Sn3+
15 0.7500000000000000  0.3402639999999999  0.4500960000000003
   Sn3+
16 0.2500000000000000  0.6597360000000001  0.5499039999999997
   Sn3+
17 0.7500000000000000  0.3314779999999999  0.0049869999999999 S-
18 0.2500000000000000  0.6685220000000001  0.9950130000000001 S-
19 0.7500000000000000  0.8314779999999999  0.4950130000000001 S-
20 0.2500000000000000  0.1685220000000001  0.5049869999999999 S-
21 0.7500000000000000  0.9821289999999998  0.8949099999999999 S2
   -
22 0.2500000000000000  0.0178710000000002  0.1050900000000001 S2
   -
23 0.7500000000000000  0.4821289999999998  0.6050900000000001 S2
   -
24 0.2500000000000000  0.5178710000000002  0.3949099999999999 S2
   -
25 0.7500000000000000  0.7196979999999999  0.2075679999999998 S2
   -
26 0.2500000000000000  0.2803020000000001  0.7924320000000002 S2
   -
27 0.7500000000000000  0.2196979999999999  0.2924320000000002 S2
   -
28 0.2500000000000000  0.7803020000000001  0.7075679999999998 S2
   -

```

LISTING C.77: POSCAR

```

1 Automatic mesh
2 0          ! number of k-points = 0 -> automatic generation
   scheme
3 Auto      ! fully automatic
4 30       ! length (R_k)

```

LISTING C.78: KPOINTS

40. S₂Sn SG:164

```

1 Sn1 S2
2 1.0000000000000000
3 1.8499601247205979 -3.2042249279925326 0.0000000000000000
4 1.8499601247205979 3.2042249279925326 0.0000000000000000
5 0.0000000000000000 0.0000000000000000 6.9779590000000002
6 Sn S
7 1 2
8 Direct
9 0.0000000000000000 0.0000000000000000 0.0000000000000000
10 0.3333333333333357 0.6666666666666643 0.2117870000000011
11 0.6666666666666643 0.3333333333333357 0.7882129999999989
12
13 0.00000000E+00 0.00000000E+00 0.00000000E+00
14 0.00000000E+00 0.00000000E+00 0.00000000E+00
15 0.00000000E+00 0.00000000E+00 0.00000000E+00

```

LISTING C.79: POSCAR

```

1 Automatic mesh
2 0 ! number of k-points = 0 -> automatic generation
   scheme
3 Auto ! fully automatic
4 201 ! length (R_k)

```

LISTING C.80: KPOINTS

41. S₂₈Sn₁₂ SG:194

```

1 S28 Sn12
2 1.0
3 13.2748003006 0.0000000000 0.0000000000
4 -6.6374001503 11.4963142905 0.0000000000
5 0.0000000000 0.0000000000 19.1520996094
6 Sn S
7 12 28
8 Direct
9 0.847440004 0.423720002 0.491519988
10 0.152559996 0.576279998 0.508480012
11 0.576279998 0.423720002 0.491519988
12 0.423720002 0.576279998 0.508480012
13 0.576279998 0.152559996 0.491519988
14 0.423720002 0.847440004 0.508480012
15 0.152559996 0.576279998 0.991519988
16 0.847440004 0.423720002 0.008480012
17 0.423720002 0.576279998 0.991519988

```

```

18 0.576279998 0.423720002 0.008480012
19 0.423720002 0.847440004 0.991519988
20 0.576279998 0.152559996 0.008480012
21 0.666666687 0.333333343 0.574299991
22 0.333333313 0.666666627 0.425700009
23 0.333333313 0.666666627 0.074299991
24 0.666666687 0.333333343 0.925700009
25 0.769190013 0.230810001 0.440899998
26 0.230809987 0.769190013 0.559100032
27 0.769190013 0.538380027 0.440899998
28 0.230810001 0.461619973 0.559100032
29 0.461619973 0.230809987 0.440899998
30 0.538380027 0.769190013 0.559100032
31 0.230809987 0.769190013 0.940899968
32 0.769190013 0.230810001 0.059100002
33 0.230810001 0.461619973 0.940899968
34 0.769190013 0.538380027 0.059100002
35 0.538380027 0.769190013 0.940899968
36 0.461619973 0.230809987 0.059100002
37 0.977999985 0.488990009 0.589370012
38 0.022000015 0.511009991 0.410629988
39 0.511009991 0.489009976 0.589370012
40 0.488990009 0.510990024 0.410629988
41 0.510990024 0.022000015 0.589370012
42 0.489009976 0.977999985 0.410629988
43 0.022000015 0.511009991 0.089370012
44 0.977999985 0.488990009 0.910629988
45 0.488990009 0.510990024 0.089370012
46 0.511009991 0.489009976 0.910629988
47 0.489009976 0.977999985 0.089370012
48 0.510990024 0.022000015 0.910629988

```

LISTING C.81: POSCAR

```

1 Automatic mesh
2 0 ! number of k-points = 0 -> automatic generation
   scheme
3 Auto ! fully automatic
4 25 ! length (R_k)

```

LISTING C.82: KPOINTS

42. $S_{17}Sn_8$ SG:56

```

1 0.5(S34 Sn16)
2 1.000000000000000

```

3	18.0765185297176920	-0.0000000000000000	0.0000000000000000
4	-0.0000000000000000	12.2641214835580072	0.0000000000000000
5	0.0000000000000000	0.0000000000000000	11.6749448143363121
6	Sn S		
7	32 68		
8	Direct		
9	0.4422273343528808	0.6044503207232695	0.1408068613746178
10	0.5577726656471196	0.3955496792767296	0.8591931086253859
11	0.0577726656471195	0.8955496792767305	0.1408068613746178
12	0.9422273343528804	0.1044503207232704	0.8591931086253859
13	0.5577726656471196	0.1044503207232703	0.3591931386253823
14	0.4422273343528808	0.8955496792767305	0.6408068913746141
15	0.9422273343528804	0.3955496792767297	0.3591931386253823
16	0.0577726656471195	0.6044503207232695	0.6408068913746141
17	0.3132870167301308	0.3647958160071006	0.1299790767725989
18	0.6867129532698674	0.6352041839928985	0.8700209232274012
19	0.1867129832698693	0.1352041839928993	0.1299790767725989
20	0.8132870467301326	0.8647958160071015	0.8700209232274012
21	0.6867129532698674	0.8647958160071015	0.3700209232274012
22	0.3132870167301309	0.1352041839928993	0.6299790767725988
23	0.8132870467301326	0.6352041839928985	0.3700209232274012
24	0.1867129832698693	0.3647958160071006	0.6299790767725988
25	0.4564036704486762	0.3735030396311602	0.3620175712466568
26	0.5435963295513243	0.6264969603688402	0.6379824287533434
27	0.0435963295513239	0.1264969603688397	0.3620175712466568
28	0.9564036704486757	0.8735030396311598	0.6379824287533434
29	0.5435963295513243	0.8735030396311598	0.1379824287533437
30	0.4564036704486761	0.1264969603688396	0.8620175712466566
31	0.9564036704486757	0.6264969603688402	0.1379824287533437
32	0.0435963295513239	0.3735030396311602	0.8620175712466566
33	0.3016349780190442	0.5777883817141551	0.3706345320429235
34	0.6983650219809556	0.4222115882858480	0.6293654679570775
35	0.1983650219809556	0.9222116182858449	0.3706345320429235
36	0.8016349780190444	0.0777884117141516	0.6293654679570775
37	0.6983650219809556	0.0777884117141516	0.1293654679570767
38	0.3016349780190442	0.9222116182858449	0.8706345320429226
39	0.8016349780190444	0.4222115882858480	0.1293654679570767
40	0.1983650219809556	0.5777883817141551	0.8706345320429226
41	0.3817838346653059	0.4826507153479927	0.0027525958310965
42	0.6182161953346886	0.5173492846520137	0.9972474191689075
43	0.1182161653346940	0.0173492846520069	0.0027525958310965
44	0.8817838046653114	-0.0173492846520139	0.9972474191689075
45	0.6182161953346886	-0.0173492846520139	0.4972474191689076
46	0.3817838346653059	0.0173492846520069	0.5027525808310925
47	0.8817838046653114	0.5173492846520137	0.4972474191689076

48	0.1182161653346869	0.4826507153479928	0.5027525808310925
49	0.5322317939073038	0.4904951636270879	0.2406602060754551
50	0.4677682060926970	0.5095048363729122	0.7593398239245468
51	0.9677682060926962	0.0095048363729123	0.2406602060754551
52	0.0322317939073034	-0.0095048363729121	0.7593398239245468
53	0.4677682060926970	-0.0095048363729121	0.2593397939245451
54	0.5322317939073038	0.0095048363729123	0.7406601760754532
55	0.0322317939073034	0.5095048363729122	0.2593397939245451
56	0.9677682060926962	0.4904951636270879	0.7406601760754532
57	0.3864437307749436	0.2457197198738247	0.2478651436375042
58	0.6135562692250560	0.7542802801261752	0.7521348563624962
59	0.1135562692250559	0.2542802801261749	0.2478651436375042
60	0.8864437307749440	0.7457197198738248	0.7521348563624962
61	0.6135562692250560	0.7457197198738248	0.2521348563624962
62	0.3864437307749436	0.2542802801261749	0.7478651436375038
63	0.8864437307749440	0.7542802801261752	0.2521348563624962
64	0.1135562692250559	0.2457197198738247	0.7478651436375038
65	0.3670901625747028	0.7175442006608342	0.2649839888447942
66	0.6329098084252974	0.2824557993391660	0.7350160411552005
67	0.1329098374252968	0.7824557993391658	0.2649839888447942
68	0.8670901915747026	0.2175442006608339	0.7350160411552005
69	0.6329098084252974	0.2175442006608339	0.2350160111552054
70	0.3670901625747028	0.7824557993391658	0.7649839588447995
71	0.8670901915747026	0.2824557993391660	0.2350160111552054
72	0.1329098374252968	0.7175442006608342	0.7649839588447995
73	0.4827909647217098	0.7461908111819052	0.0112354882009717
74	0.5172090652782854	0.2538091888180883	0.9887644977990280
75	0.0172090352782903	0.7538091888180948	0.0112354882009717
76	0.9827909347217146	0.2461908111819117	0.9887644977990280
77	0.5172090652782853	0.2461908111819117	0.4887644977990271
78	0.4827909647217097	0.7538091888180948	0.5112355022009720
79	0.9827909347217147	0.2538091888180883	0.4887644977990271
80	0.0172090352782903	0.7461908111819052	0.5112355022009720
81	0.2257719416542580	0.4678160972180993	0.2448553005705328
82	0.7742280883457445	0.5321839027819006	0.7551446694294636
83	0.2742280583457424	0.0321839027819005	0.2448553005705328
84	0.7257719116542555	0.9678160972180994	0.7551446694294636
85	0.7742280883457445	0.9678160972180994	0.2551446994294673
86	0.2257719416542580	0.0321839027819005	0.7448553305705364
87	0.7257719116542555	0.5321839027819006	0.2551446994294673
88	0.2742280583457424	0.4678160972180993	0.7448553305705364
89	0.3855458724502653	0.4798947145926400	0.4969577134642273
90	0.6144541275497337	0.5201052854073610	0.5030423165357755
91	0.1144541275497345	0.0201052854073602	0.4969577134642273
92	0.8855458724502662	0.9798947145926390	0.5030423165357755

93	0.6144541275497337	0.9798947145926390	0.0030422865357726
94	0.3855458724502653	0.0201052854073602	-0.0030423165357752
95	0.8855458724502663	0.5201052854073610	0.0030422865357726
96	0.1144541275497345	0.4798947145926399	-0.0030423165357752
97	0.2500000000000000	0.2500000000000000	-0.0060417661337304
98	0.7500000000000000	0.7500000000000000	0.0060417511337252
99	0.7500000000000000	0.7500000000000000	0.5060417511337258
100	0.2500000000000000	0.2500000000000000	0.4939582488662747
101	0.2218177277868941	0.6770299057878704	0.5027528403156708
102	0.7781823022131082	0.3229700942121291	0.4972471596843300
103	0.2781822722131055	0.8229700942121296	0.5027528403156709
104	0.7218176977868918	0.1770299057878711	0.4972471596843300
105	0.7781823022131082	0.1770299057878711	-0.0027528403156706
106	0.2218177277868941	0.8229700942121296	0.0027528403156702
107	0.7218176977868918	0.3229700942121292	-0.0027528403156706
108	0.2781822722131056	0.6770299057878704	0.0027528403156702
109			
110	0.00000000E+00	0.00000000E+00	0.00000000E+00
111	0.00000000E+00	0.00000000E+00	0.00000000E+00
112	0.00000000E+00	0.00000000E+00	0.00000000E+00
113	0.00000000E+00	0.00000000E+00	0.00000000E+00
114	0.00000000E+00	0.00000000E+00	0.00000000E+00
115	0.00000000E+00	0.00000000E+00	0.00000000E+00
116	0.00000000E+00	0.00000000E+00	0.00000000E+00
117	0.00000000E+00	0.00000000E+00	0.00000000E+00
118	0.00000000E+00	0.00000000E+00	0.00000000E+00
119	0.00000000E+00	0.00000000E+00	0.00000000E+00
120	0.00000000E+00	0.00000000E+00	0.00000000E+00
121	0.00000000E+00	0.00000000E+00	0.00000000E+00
122	0.00000000E+00	0.00000000E+00	0.00000000E+00
123	0.00000000E+00	0.00000000E+00	0.00000000E+00
124	0.00000000E+00	0.00000000E+00	0.00000000E+00
125	0.00000000E+00	0.00000000E+00	0.00000000E+00
126	0.00000000E+00	0.00000000E+00	0.00000000E+00
127	0.00000000E+00	0.00000000E+00	0.00000000E+00
128	0.00000000E+00	0.00000000E+00	0.00000000E+00
129	0.00000000E+00	0.00000000E+00	0.00000000E+00
130	0.00000000E+00	0.00000000E+00	0.00000000E+00
131	0.00000000E+00	0.00000000E+00	0.00000000E+00
132	0.00000000E+00	0.00000000E+00	0.00000000E+00
133	0.00000000E+00	0.00000000E+00	0.00000000E+00
134	0.00000000E+00	0.00000000E+00	0.00000000E+00
135	0.00000000E+00	0.00000000E+00	0.00000000E+00
136	0.00000000E+00	0.00000000E+00	0.00000000E+00
137	0.00000000E+00	0.00000000E+00	0.00000000E+00

138	0.00000000E+00	0.00000000E+00	0.00000000E+00
139	0.00000000E+00	0.00000000E+00	0.00000000E+00
140	0.00000000E+00	0.00000000E+00	0.00000000E+00
141	0.00000000E+00	0.00000000E+00	0.00000000E+00
142	0.00000000E+00	0.00000000E+00	0.00000000E+00
143	0.00000000E+00	0.00000000E+00	0.00000000E+00
144	0.00000000E+00	0.00000000E+00	0.00000000E+00
145	0.00000000E+00	0.00000000E+00	0.00000000E+00
146	0.00000000E+00	0.00000000E+00	0.00000000E+00
147	0.00000000E+00	0.00000000E+00	0.00000000E+00
148	0.00000000E+00	0.00000000E+00	0.00000000E+00
149	0.00000000E+00	0.00000000E+00	0.00000000E+00
150	0.00000000E+00	0.00000000E+00	0.00000000E+00
151	0.00000000E+00	0.00000000E+00	0.00000000E+00
152	0.00000000E+00	0.00000000E+00	0.00000000E+00
153	0.00000000E+00	0.00000000E+00	0.00000000E+00
154	0.00000000E+00	0.00000000E+00	0.00000000E+00
155	0.00000000E+00	0.00000000E+00	0.00000000E+00
156	0.00000000E+00	0.00000000E+00	0.00000000E+00
157	0.00000000E+00	0.00000000E+00	0.00000000E+00
158	0.00000000E+00	0.00000000E+00	0.00000000E+00
159	0.00000000E+00	0.00000000E+00	0.00000000E+00
160	0.00000000E+00	0.00000000E+00	0.00000000E+00
161	0.00000000E+00	0.00000000E+00	0.00000000E+00
162	0.00000000E+00	0.00000000E+00	0.00000000E+00
163	0.00000000E+00	0.00000000E+00	0.00000000E+00
164	0.00000000E+00	0.00000000E+00	0.00000000E+00
165	0.00000000E+00	0.00000000E+00	0.00000000E+00
166	0.00000000E+00	0.00000000E+00	0.00000000E+00
167	0.00000000E+00	0.00000000E+00	0.00000000E+00
168	0.00000000E+00	0.00000000E+00	0.00000000E+00
169	0.00000000E+00	0.00000000E+00	0.00000000E+00
170	0.00000000E+00	0.00000000E+00	0.00000000E+00
171	0.00000000E+00	0.00000000E+00	0.00000000E+00
172	0.00000000E+00	0.00000000E+00	0.00000000E+00
173	0.00000000E+00	0.00000000E+00	0.00000000E+00
174	0.00000000E+00	0.00000000E+00	0.00000000E+00
175	0.00000000E+00	0.00000000E+00	0.00000000E+00
176	0.00000000E+00	0.00000000E+00	0.00000000E+00
177	0.00000000E+00	0.00000000E+00	0.00000000E+00
178	0.00000000E+00	0.00000000E+00	0.00000000E+00
179	0.00000000E+00	0.00000000E+00	0.00000000E+00
180	0.00000000E+00	0.00000000E+00	0.00000000E+00
181	0.00000000E+00	0.00000000E+00	0.00000000E+00
182	0.00000000E+00	0.00000000E+00	0.00000000E+00

```
183 0.00000000E+00 0.00000000E+00 0.00000000E+00
184 0.00000000E+00 0.00000000E+00 0.00000000E+00
185 0.00000000E+00 0.00000000E+00 0.00000000E+00
186 0.00000000E+00 0.00000000E+00 0.00000000E+00
187 0.00000000E+00 0.00000000E+00 0.00000000E+00
188 0.00000000E+00 0.00000000E+00 0.00000000E+00
189 0.00000000E+00 0.00000000E+00 0.00000000E+00
190 0.00000000E+00 0.00000000E+00 0.00000000E+00
191 0.00000000E+00 0.00000000E+00 0.00000000E+00
192 0.00000000E+00 0.00000000E+00 0.00000000E+00
193 0.00000000E+00 0.00000000E+00 0.00000000E+00
194 0.00000000E+00 0.00000000E+00 0.00000000E+00
195 0.00000000E+00 0.00000000E+00 0.00000000E+00
196 0.00000000E+00 0.00000000E+00 0.00000000E+00
197 0.00000000E+00 0.00000000E+00 0.00000000E+00
198 0.00000000E+00 0.00000000E+00 0.00000000E+00
199 0.00000000E+00 0.00000000E+00 0.00000000E+00
200 0.00000000E+00 0.00000000E+00 0.00000000E+00
201 0.00000000E+00 0.00000000E+00 0.00000000E+00
202 0.00000000E+00 0.00000000E+00 0.00000000E+00
203 0.00000000E+00 0.00000000E+00 0.00000000E+00
204 0.00000000E+00 0.00000000E+00 0.00000000E+00
205 0.00000000E+00 0.00000000E+00 0.00000000E+00
206 0.00000000E+00 0.00000000E+00 0.00000000E+00
207 0.00000000E+00 0.00000000E+00 0.00000000E+00
208 0.00000000E+00 0.00000000E+00 0.00000000E+00
209 0.00000000E+00 0.00000000E+00 0.00000000E+00
```

LISTING C.83: POSCAR

```
1 Automatic mesh
2 0 ! number of k-points = 0 -> automatic generation
   scheme
3 Auto ! fully automatic
4 25 ! length (R_k)
```

LISTING C.84: KPOINTS

Appendix D

Chapter 5 Supplement: Python code for ternary phase diagram

Here, is the supplementary information for chapter 5. The python code we used for the analysis of ternary phase diagram is subdivided into different programs named as `main.py`, `PhaseDiagram.py`, `GenerateData.py`, and `IntersectionPoint.py`.

D.1 `main.py`

To utilize this program, the user is required to provide input. Firstly, the user needs to modify the list of elements involved in the phase diagram by editing the line `species = ['Sn', 'Co', 'S']`. This list is used as input by the program. Secondly, the user has to provide a `*.csv` file, which contains the formation energies of all the binary compounds, and subsequently, modify the file name in the line `CompoundDictionary = GenerateData.data2dict("Co3Sn2S2.csv"), species`. The file name should be the ternary compound, for example, $\text{Co}_3\text{Sn}_2\text{S}_2$ because it will be used further by `GenerateData.py` for the calculation of composition. The code for `main.py` is shown below:

```
1 # -*- coding: utf-8 -*-
2 """
3 @author: sainih5
4 """
5
6 import GenerateData
7 import PhaseDiagram
8 import numpy as np
9 import sys
10 import chemparse
11
12 species = ['Sn', 'Co', 'S']
13 CompoundDictionary = GenerateData.data2dict("Co3Sn2S2.csv", species)
14
15 for i in range(0, len(CompoundDictionary)-3):
16     #print (CompoundDictionary[i])
17     #print (CompoundDictionary[i]["Composition"].keys())
18     temp = GenerateData.Coordinates(CompoundDictionary[i]["Composition"],
19     species)
20     CompoundDictionary[i].update(x=temp[0], y=temp[1])
21
22 for i in range(len(CompoundDictionary)-3, len(CompoundDictionary)):
23     CompoundDictionary[i].update(x=GenerateData.TriangleCoordinates()
24    [:-1][i-len(CompoundDictionary)+3][0],
25     y=GenerateData.TriangleCoordinates()
26    [:-1][i-len(CompoundDictionary)+3][1])
27
28 PhaseDiagram.Figure(species, CompoundDictionary)
```

The format for the *.csv is shown in Fig. D.1. Here, the example file of $\text{Co}_3\text{Sn}_2\text{S}_2$ is shown.

	A	B
1	Compound	Formation energy
2	Co9S8	-0.7301
3	Co3S4	-0.7303
4	CoS2	-0.6848
5	CoSn	-0.1085
6	CoSn3	-0.0619
7	S2Sn	-0.7084
8	SSn	-0.6974

FIGURE D.1: Format for the $\text{Co}_3\text{Sn}_2\text{S}_2$.csv file.

D.2 GenerateData.py

After the user has provided all the necessary inputs, the `GenerateData.py` module executes multiple computations to generate the phase diagram. These calculations include determining the composition of the compounds, arranging the formation energies, and calculating the coordinates for the ternary graph along with the axis points. The code `GenerateData.py` is

```
1 # -*- coding: utf-8 -*-
2 """
3 @author: sainih5
4 """
5
6 import chemparse
7 import pandas as pd
8 import numpy as np
9 import IntersectionPoint
10
11 def TriangleCoordinates(norm=1):
12     A_raw = np.array([[100, 0, 0], [0, 100, 0], [0, 0, 100]])
13     A_norm = np.zeros([3, 3])
14     count = 0
15     sum = 0
16     for i in range(0, 3):
```

```
17         sum = A_raw[count][0]+A_raw[count][1]+A_raw[count][2]
18         count += 1
19         for j in range(0, 3):
20             A_norm[i][j] = norm*A_raw[i][j]/sum
21
22     # Diagram coordinates
23     x = [0.0]
24     y = [0.0]
25     for i in A_norm:
26         x.append(1/2*i[0]+i[1])
27         y.append(i[0])
28
29     XY = np.array([x, y]).transpose()
30     return (XY)
31
32
33 def data2dict(filename, species):
34     df = pd.read_csv(filename)
35     mat = []
36     mat_info = []
37     FormationEnergy = []
38     for i in range(len(df)):
39         mat.append(df.iloc[i, 0])
40         FormationEnergy.append(df.iloc[i, 1])
41         mat_info.append(chemparse.parse_formula(df.iloc[i, 0]))
42     CompoundDictionary = []
43     for i, j, k in zip(mat, FormationEnergy, mat_info):
44         CompoundDictionary.append({
45             "Compound" : i,
46             "Formation Energy" : j,
47             "Composition" : k
48         })
49     for i in species:
50         CompoundDictionary.append({
51             "Compound" : i,
52             "Formation Energy" : 0,
53             "Composition" : chemparse.parse_formula(i)
54         })
55     return (CompoundDictionary)
56
57 def line_AB(a, b, norm=1):
58     return (norm/2 - ((norm-(norm - a/(a+b))))/2)
59
60 def line_BC(a, b, norm=1):
61     return (norm - (a/(2*(a+b))))
```

```
62
63 def Coordinates(i, species, norm=1):
64     if species[0] in i.keys() and species[1] in i.keys():
65         return(np.array([line_AB(i[species[0]], i[species[1]], norm),
66 norm - i[species[0]]/(i[species[0]]+i[species[1]])]))
67     if species[0] in i.keys() and species[2] in i.keys():
68         return(np.array([norm - (i[species[0]]/(i[species[0]]+i[species
69 [2]])), 0]))
70     if species[1] in i.keys() and species[2] in i.keys():
71         return(np.array([line_BC(i[species[1]], i[species[2]], norm), i[
72 species[1]]/(i[species[1]]+i[species[2]])]))
73
74 def FindLineCoordinates(CompoundDictionary):
75     line_x = []
76     line_y = []
77     for i in CompoundDictionary:
78         line_x.append(i["x"])
79         line_y.append(i["y"])
80
81     return (line_x, line_y)
82
83 def ReduceLines(lines):
84     a1 = (lines[0]["x1"], lines[0]["y1"])
85     a2 = (lines[0]["x2"], lines[0]["y2"])
86     b1 = (lines[1]["x1"], lines[1]["y1"])
87     b2 = (lines[1]["x2"], lines[1]["y2"])
88     if (IntersectionPoint.get_intersect(a1, a2, b1, b2) != 0):
89         temp1, temp2 = IntersectionPoint.get_intersect(a1, a2, b1, b2)
90         p1 = lines[0]["x1"], lines[0]["y1"], lines[0]["z1"]
91         p2 = lines[0]["x2"], lines[0]["y2"], lines[0]["z2"]
92         z1 = IntersectionPoint.getZ(p1, p2, temp1, temp2)
93         p1 = lines[1]["x1"], lines[1]["y1"], lines[1]["z1"]
94         p2 = lines[1]["x2"], lines[1]["y2"], lines[1]["z2"]
95         z2 = IntersectionPoint.getZ(p1, p2, temp1, temp2)
96         if (z1 < z2):
97             #print ("Line 1 present")
98             return (lines[0])
99         if (z1 > z2):
100             print ("Line 2 present")
101             return (lines[1])
102         else:
103             #print ("-----Line 1 & 2 present")
104             return (lines)
105     else:
106         #print ("No intersection point")
107         #print ("Line 1 & 2 present")
```

```
return 0
```

D.3 PhaseDiagram.py

Upon completion of the data organization process, the `PhaseDiagram.py` module examines the data and generates a ternary phase diagram. The program produces two types of plots: one containing all possible composition lines in the phase diagram and the other depicting reduced composition lines. The reduced composition lines correspond to the most favorable compositions present in the ternary phase diagram as shown in Fig. [D.2](#).

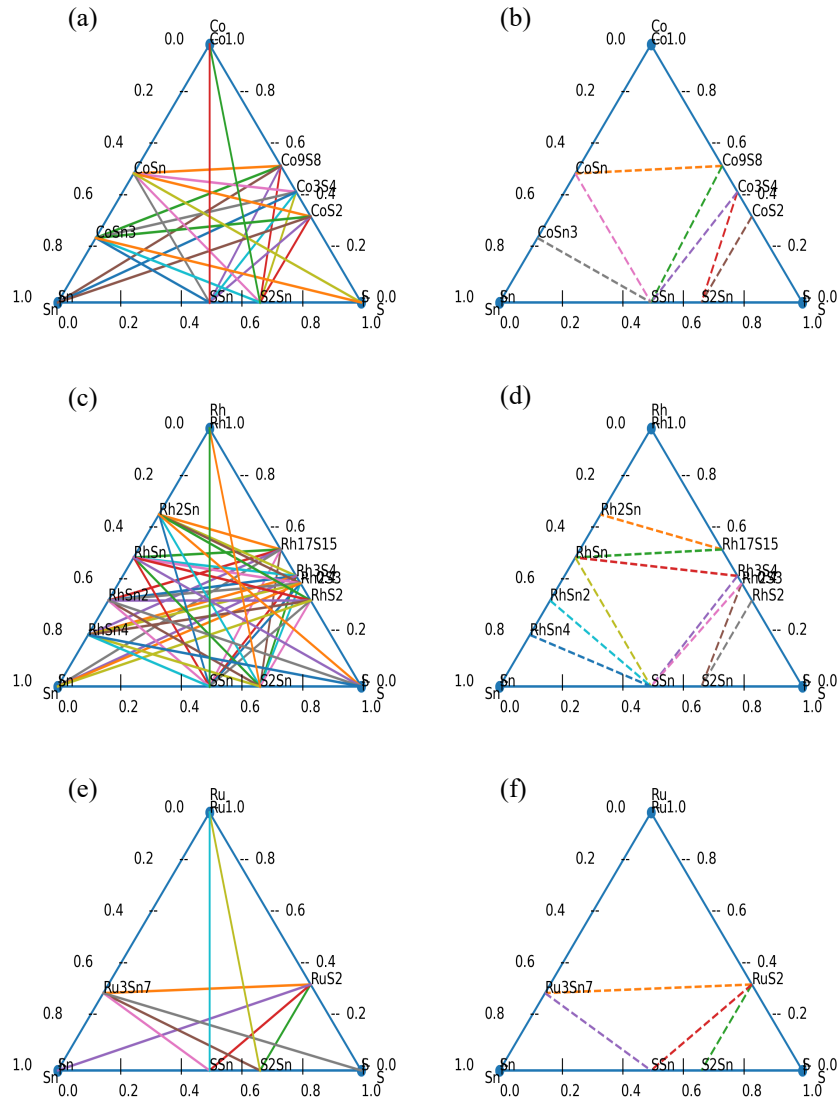


FIGURE D.2: Illustration of ternary phase diagram using in-lab developed python code. (a), (c), and (e) are composed with solid lines which shows all the possible compositions exist. (b), (d), and (f) are composed with dotted lines which belongs to the stable compositions. (a), (b) $\text{Co}_3\text{Sn}_2\text{S}_2$; (c), (d) $\text{Rh}_3\text{Sn}_2\text{S}_2$; (e), (f) $\text{Ru}_3\text{Sn}_2\text{S}_2$,

The python code for PhaseDiagram.py is

```

1 # -*- coding: utf-8 -*-
2 """
3 @author: sainih5

```

```
4 """
5
6 import numpy as np
7 import matplotlib.pyplot as plt
8 import GenerateData
9 import IntersectionPoint
10
11 def axis_points(n_points, X, Y):
12     len_x = (Y[0] - X[0])/n_points
13     len_y = (Y[1] - X[1])/n_points
14     axis_x = []
15     axis_y = []
16     for i in range(0, n_points+1):
17         axis_x.append((Y[0] - (i*len_x))
18         axis_y.append((Y[1] - (i*len_y))
19
20     axis_xy = np.array([np.abs(axis_x), np.abs(axis_y)]).transpose()
21     return (axis_xy)
22
23 def Figure(species, CompoundDictionary, norm=1):
24     XY = GenerateData.TriangleCoordinates()
25     axis_AB = axis_points(5, XY[0, :], XY[1, :])
26     axis_BC = axis_points(5, XY[1, :], XY[2, :])
27     axis_AC = axis_points(5, XY[2, :], XY[0, :])
28
29     plt.figure(dpi=300)
30     plt.scatter(XY[:, 0], XY[:, 1], marker='o')
31     plt.plot(XY[:, 0], XY[:, 1], '-o')
32     plt.xlim(0-20*norm/100, norm + 20*norm/100)
33     plt.ylim(0-20*norm/100, norm + 20*norm/100)
34     plt.annotate(species[0], ((-5*XY.max()/100), -(5*XY.max()/100)))
35     plt.annotate(species[1], ((5*XY.max()/100), (5*XY.max()/100 + XY.max()
36     plt.annotate(species[2], ((5*XY.max()/100 + XY.max()), -(5*XY.max()
37     #plt.grid()
38     plt.axis('off')
39     for i in axis_AB:
40         plt.annotate('--', (i[0], i[1]))
41         plt.annotate(str("%.1f"%np.abs(i[1]-axis_AB.max())), (i[0]-(15*
42     axis_AB[:, 1].max()/100), i[1]))
43
44     for i in axis_BC:
45         plt.annotate('--', (i[0], i[1]))
```

```
45     plt.annotate(str("%.1f"%np.abs(i[1])), (i[0]+(5*axis_BC[:, 0].max
46     ()/100),i[1]))
47
48     for i in axis_AC:
49         plt.annotate('|', (i[0],i[1]))
50         plt.annotate(str("%.1f"%np.abs(i[0])), (i[0],i[1]-(10*axis_AC[:,
51     0].max()/100)))
52     for i in CompoundDictionary:
53         plt.annotate(i["Compound"], (i["x"], i["y"]))
54
55     lines = []
56     count = 0
57     for i in range(0, len(CompoundDictionary)):
58         for j in range(i+1, len(CompoundDictionary)):
59             p1 = (float("%.4f" %CompoundDictionary[i]["x"]), float("%.4f"
60             %CompoundDictionary[i]["y"]))
61             p2 = (float("%.4f" %CompoundDictionary[j]["x"]), float("%.4f"
62             %CompoundDictionary[j]["y"]))
63
64             if (IntersectionPoint.get_identical(p1, p2) == False):
65                 count += 1
66                 lines.append({"Line"+str(count) :
67                 CompoundDictionary[i]["Compound"] + "-" +
68                 CompoundDictionary[j]["Compound"],
69                 "x1" : CompoundDictionary[i]["x"],
70                 "y1" : CompoundDictionary[i]["y"],
71                 "z1" : CompoundDictionary[i]["Formation
72                 Energy"],
73                 "x2" : CompoundDictionary[j]["x"],
74                 "y2" : CompoundDictionary[j]["y"],
75                 "z2" : CompoundDictionary[j]["Formation
76                 Energy"]})
77
78     #plt.plot([CompoundDictionary[i]["x"],
79     #         CompoundDictionary[j]["x"]],
80     #         [CompoundDictionary[i]["y"],
81     #         CompoundDictionary[j]["y"]],
82     #         '-')
```

```
83         b2 = (lines[n]["x2"], lines[n]["y2"])
84         if (IntersectionPoint.get_intersect(a1, a2, b1, b2) != 0):
85             temp1, temp2 = IntersectionPoint.get_intersect(a1, a2, b1
, b2)
86             temp1 = float("%.4f" %temp1)
87             temp2= float("%.4f" %temp2)
88             x1 = float("%.4f" %lines[m]["x1"])
89             x2 = float("%.4f" %lines[m]["y1"])
90             x3 = float("%.4f" %lines[m]["x2"])
91             x4 = float("%.4f" %lines[m]["y2"])
92             if (temp1 == x1 and temp2 == x2):
93                 True
94             elif (temp1 == x3 and temp2 == x4):
95                 True
96             else:
97
98                 z1 = IntersectionPoint.getZ((lines[m]["x1"], lines[m]
["y1"], lines[m]["z1"]),
99                                     (lines[m]["x2"],
lines[m]["y2"], lines[m]["z2"]),
100                                     temp1, temp2)
101                 z2 = IntersectionPoint.getZ((lines[n]["x1"], lines[n]
["y1"], lines[n]["z1"]),
102                                     (lines[n]["x2"], lines[n]
["y2"], lines[n]["z2"]),
103                                     temp1, temp2)
104                 z1 = float("%.4f" %z1)
105                 z2 = float("%.4f" %z2)
106                 if z1 < z1:
107                     data.append([m+1, n+1, z1, z2, m+1, n+1])
108                 if z1 > z2:
109                     data.append([m+1, n+1, z1, z2, n+1, m+1])
110
111         del_line_no = []
112         line_no = []
113         for i in range(0, len(data)):
114             line_no.append(data[i][-2])
115             for j in range(0, len(data)):
116                 if (data[i][-2] == data[j][-1]):
117                     del_line_no.append(data[i][-2])
118                     del_line_no.append(data[i][-1])
119
120         del_line_no = [i for n, i in enumerate(del_line_no) if i not in
del_line_no[n + 1:]]
121         del_line_no.sort()
```

```
122     line_no = [i for n, i in enumerate(line_no) if i not in line_no[n +
123     1:]]
123     line_no.sort()
124     test = np.setdiff1d(line_no, del_line_no)
125     for i in test:
126         line = str("Line"+str(i))
127         for k in lines:
128             if line in k.keys():
129                 #True
130                 plt.plot([k["x1"], k["x2"]], [k["y1"], k["y2"]], '--')
131     return (lines)
```

The `IntersectionPoint.py` module computes the intersection points of all the possible composition lines. Once the coordinates of the intersection points have been determined, a nested loop compares the corresponding formation energies. The composition line that yields the minimum formation energy is projected onto the ternary phase diagram as shown in Fig. D.2(b),(d),(f).

The python code for `IntersectionPoint.py` is

```
1 # -*- coding: utf-8 -*-
2 """
3 @author: sainih5
4 """
5
6 import numpy as np
7
8 def get_identical(p1, p2):
9     x1, y1 = p1
10    x2, y2 = p2
11    #print (p1, p2)
12    if (float("%.3f" %y1) == float("%.3f" %(2*x1)) and float("%.3f" %y2)
13    == float("%.3f" %(2*x2))):
14        return True
15    elif (float("%.3f" %y1) == float("%.3f" %((-2*x1)+2)) and float("%.3f
16    " %y2) == float("%.3f" %((-2*x2)+2))):
17        return True
18    elif (y1 == (0*x1) and y2 == (0*x2)):
19        return True
20    else:
21        return False
22
23 def get_intersect(a1, a2, b1, b2):
24     """
```

```
24 Returns the point of intersection of the lines passing through a2,a1
25 and b2,b1.
26 a1: [x, y] a point on the first line
27 a2: [x, y] another point on the first line
28 b1: [x, y] a point on the second line
29 b2: [x, y] another point on the second line
30 """
31 s = np.vstack([a1,a2,b1,b2])          # s for stacked
32 h = np.hstack((s, np.ones((4, 1))))  # h for homogeneous
33 l1 = np.cross(h[0], h[1])            # get first line
34 l2 = np.cross(h[2], h[3])            # get second line
35 x, y, z = np.cross(l1, l2)           # point of intersection
36 if z == 0:                            # lines are parallel
37     #return (float('inf'), float('inf'))
38     return 0
39 #if ((x/z, y/z) == a1 or (x/z, y/z) == a2 or (x/z, y/z) == b1 or (x/z
40 , y/z) == b2):
41     # return 0
42
43 if (x/z < 0):
44     return 0
45 if (y/z < 0):
46     return 0
47 if (x/z > 1):
48     return 0
49 if (y/z > 1):
50     return 0
51 if (x/z < y/(2*z)):
52     return 0
53 if (x/z > (1 - y/(2*z))):
54     return 0
55
56 return (x/z, y/z)
57
58 def getZ(p1, p2, x, y):
59     x1, y1, z1 = p1
60     x2, y2, z2 = p2
61
62     if x2 - x1 != 0:
63         t = (x - x1) / (x2 - x1)
64     elif y2 - y1 != 0:
65         t = (y - y1) / (y2 - y1)
66     else:
67         return 0
```

```
67     return z1 + (z2 - z1)*t
```

D.4 Phase diagrams and convex Hull using ASE Python Package [101]

To check the accuracy of our results we have compared the ternary phase diagrams and convex Hull with the one generated by ASE python package [101], as shown in Fig. D.3. The results in Fig. D.3(a),(b) are consistent with our results in Fig. D.2. The convex Hull in Fig. D.3(c) is also same as we got in Fig. 5.4(a). The script we used to generate the figure using ASE python package [101] is

```
1  #!/usr/bin/env python
2  #coding: utf-8
3
4  # In[7]:
5
6
7  from ase.phasediagram import PhaseDiagram
8
9
10 # In[8]:
11
12
13 from ase.phasediagram import PhaseDiagram
14 references = [('Sn', -3.84555104), ('S', -4.127496789), ('Co',
15               -7.014222655),
16               ('Co9S8', -108.5611298), ('Co3S4', -42.66482287),
17               ('CoS2', -17.32511867), ('CoSn', -11.07683866),
18               ('CoSn3', -18.79850623), ('S2Sn', -14.22580525),
19               ('SSn', -9.367919135)]#, ('Co3Sn2S2', -40.46422341)]
20 pd = PhaseDiagram(references)
21 pd.plot(dims=2, show=False)
22
23 # In[9]:
24
25
26 from ase.phasediagram import PhaseDiagram
27 references = [('Sn', -3.84555104), ('S', -4.127496789), ('Co',
28               -7.014222655),
29               ('Co9S8', -108.5611298), ('Co3S4', -42.66482287),
30               ('CoS2', -17.32511867), ('CoSn', -11.07683866),
31               ('CoSn3', -18.79850623), ('S2Sn', -14.22580525),
```

```
31         ('SSn', -9.367919135), ('Co3Sn2S2', -40.46422341)]
32 pd = PhaseDiagram(references)
33 pd.plot(dims=2, show=False)
34
35
36 # In[6]:
37
38
39 refs = [('Co', 0.0),
40         ('S', 0.0),
41         ('Co2S3', -3.542875238),
42         ('Co2S3', -3.48068019),
43         ('Co3S', 0.386698089),
44         ('Co9S8', -12.41315161),
45         ('CoS', -1.372446176),
46         ('CoS', -1.064261821),
47         ('CoS2', -2.054518659),
48         ('CoS2', -2.055902434),
49         ('CoS2', -1.791885784),
50         ('CoS2', -1.716813077),
51         ('CoS2', -1.167579957),
52         ('Co3S4', -5.112167744)]
53 pd = PhaseDiagram(refs)
54 pd.plot(show=True)
55
56
57 # In[ ]:
```

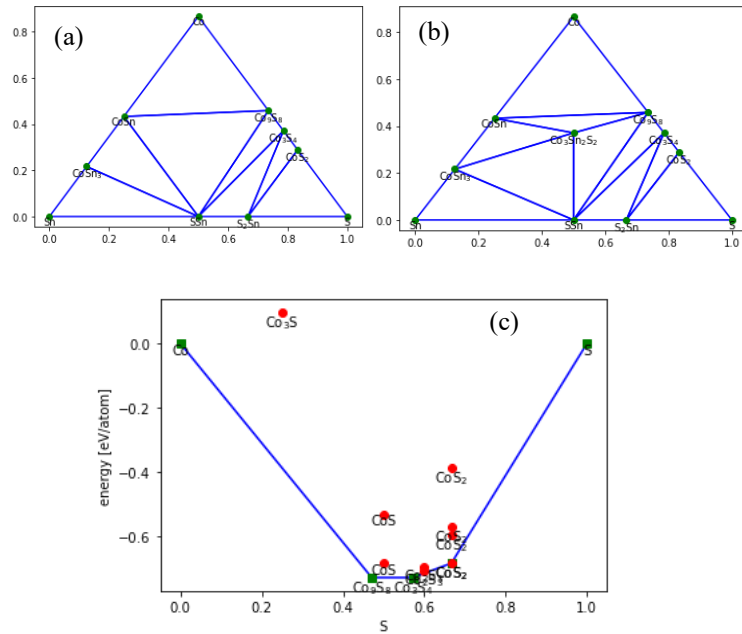


FIGURE D.3: Illustration of ternary phase diagram using ASE python package [101]. (a) Ternary phase diagram with binary phase only, (b) Ternary phase diagram with ternary compound, and (c) Convex Hull diagram for Co-S

Bibliography

- [1] S. M. Young et al. Dirac Semimetal in Three Dimensions. *Physical Review Letters* 108(14) (2012), 140405.
- [2] J. Liu and D. Vanderbilt. Weyl semimetals from noncentrosymmetric topological insulators. *Physical Review B* 90(15) (2014), 155316.
- [3] H. Weng et al. Weyl Semimetal Phase in Noncentrosymmetric Transition-Metal Monophosphides. *Physical Review X* 5(1) (2015), 011029.
- [4] D. Vanderbilt. *Berry phases in electronic structure theory*. Cambridge University Press, 2018.
- [5] D. Gresch et al. Z2Pack: Numerical implementation of hybrid Wannier centers for identifying topological materials. *Physical Review B* 95(7) (2017), 075146.
- [6] F. Giustino. *Materials modelling using density functional theory: properties and predictions*. Oxford University Press, 2014.
- [7] R. M. Martin. *Electronic Structure: Basic Theory and Practical Methods*. Cambridge University Press, 2020.
- [8] C. J. Bartel. Review of computational approaches to predict the thermodynamic stability of inorganic solids. *Journal of Materials Science* 57(23) (2022), 10475–10498.
- [9] *Beyond CMOS - IEEE International Roadmap for Devices and Systems*. <https://irds.ieee.org/home/what-is-beyond-cmos>. 2018.
- [10] B. Dieny et al. Opportunities and challenges for spintronics in the microelectronics industry. *Nature Electronics* 3(8) (2020), 446–459.
- [11] Y. Tokura, M. Kawasaki, and N. Nagaosa. Emergent functions of quantum materials. *Nature Physics* 13(11) (2017), 1056–1068.
- [12] T. Liang et al. Ultrahigh mobility and giant magnetoresistance in the Dirac semimetal Cd_3As_2 . *Nature Materials* 14(3) (2015), 280–284.
- [13] X. Huang et al. Observation of the Chiral-Anomaly-Induced Negative Magnetoresistance in 3D Weyl Semimetal TaAs. *Physical Review X* 5(3) (2015), 031023.

- [14] C.-L. Zhang et al. Signatures of the Adler–Bell–Jackiw chiral anomaly in a Weyl fermion semimetal. *Nature Communications* 7(1) (2016), 10735.
- [15] J. Xiong et al. Evidence for the chiral anomaly in the Dirac semimetal Na_3Bi . *Science* 350(6259) (2015), 413–416.
- [16] H. Nielsen and M. Ninomiya. The Adler-Bell-Jackiw anomaly and Weyl fermions in a crystal. *Physics Letters B* 130(6) (1983), 389–396.
- [17] D. T. Son and B. Z. Spivak. Chiral anomaly and classical negative magnetoresistance of Weyl metals. *Physical Review B* 88(10) (2013), 104412.
- [18] A. K. Nayak et al. Large anomalous Hall effect driven by a nonvanishing Berry curvature in the noncollinear antiferromagnet Mn_3Ge . *Science Advances* 2(4) (2016), e1501870.
- [19] T. Suzuki et al. Large anomalous Hall effect in a half-Heusler antiferromagnet. *Nature Physics* 12(12) (2016), 1119–1123.
- [20] Q. Wang et al. Large intrinsic anomalous Hall effect in half-metallic ferromagnet $\text{Co}_3\text{Sn}_2\text{S}_2$ with magnetic Weyl fermions. *Nature Communications* 9(1) (2018), 3681.
- [21] E. Liu et al. Giant anomalous Hall effect in a ferromagnetic Kagome-lattice semimetal. *Nature Physics* 14(11) (2018), 1125–1131.
- [22] S. Nakatsuji, N. Kiyohara, and T. Higo. Large anomalous Hall effect in a non-collinear antiferromagnet at room temperature. *Nature* 527(7577) (2015), 212–215.
- [23] X. Wan, A. M. Turner, A. Vishwanath, and S. Y. Savrasov. Topological semimetal and Fermi-arc surface states in the electronic structure of pyrochlore iridates. *Physical Review B* 83(20) (2011), 205101.
- [24] S.-Y. Xu et al. Discovery of a Weyl fermion semimetal and topological Fermi arcs. *Science* 349(6248) (2015), 613–617.
- [25] M. Z. Hasan and C. L. Kane. *Colloquium* : Topological insulators. *Reviews of Modern Physics* 82(4) (2010), 3045–3067.
- [26] X.-L. Qi and S.-C. Zhang. Topological insulators and superconductors. *Reviews of Modern Physics* 83(4) (2011), 1057–1110.
- [27] A. Bansil, H. Lin, and T. Das. *Colloquium* : Topological band theory. *Reviews of Modern Physics* 88(2) (2016), 021004.
- [28] D. N. Basov, R. D. Averitt, and D. Hsieh. Towards properties on demand in quantum materials. *Nature Materials* 16(11) (2017), 1077–1088.

Bibliography

- [29] N. Armitage, E. Mele, and A. Vishwanath. Weyl and Dirac semimetals in three-dimensional solids. *Reviews of Modern Physics* 90(1) (2018), 015001.
- [30] H. Weng, X. Dai, and Z. Fang. Topological semimetals predicted from first-principles calculations. *Journal of Physics: Condensed Matter* 28(30) (2016), 303001.
- [31] H. Weng, C. Fang, Z. Fang, and X. Dai. Topological semimetals with triply degenerate nodal points in θ -phase tantalum nitride. *Physical Review B* 93 (24 2016), 241202.
- [32] S. Dzsaber et al. Giant spontaneous Hall effect in a nonmagnetic Weyl-Kondo semimetal. *Proceedings of the National Academy of Sciences* 118 (8 2021), e2013386118.
- [33] G. Xu et al. Chern Semimetal and the Quantized Anomalous Hall Effect in HgCr_2Se_4 . *Physical Review Letters* 107(18) (2011), 186806.
- [34] J. Kübler and C. Felser. Weyl points in the ferromagnetic Heusler compound Co_2MnAl . *EPL (Europhysics Letters)* 114(4) (2016), 47005.
- [35] Z. Wang et al. Time-Reversal-Breaking Weyl Fermions in Magnetic Heusler Alloys. *Physical Review Letters* 117(23) (2016), 236401.
- [36] G. Chang et al. Room-temperature magnetic topological Weyl fermion and nodal line semimetal states in half-metallic Heusler Co_2TiX (X=Si, Ge, or Sn). *Scientific Reports* 6(1) (2016), 38839.
- [37] K. Ohgushi, S. Murakami, and N. Nagaosa. Spin anisotropy and quantum Hall effect in the *kagomé* lattice: Chiral spin state based on a ferromagnet. *Physical Review B* 62(10) (2000), R6065–R6068.
- [38] G. Xu, B. Lian, and S.-C. Zhang. Intrinsic Quantum Anomalous Hall Effect in the Kagome Lattice $\text{Cs}_2\text{LiMn}_3\text{F}_{12}$. *Physical Review Letters* 115(18) (2015), 186802.
- [39] L. Balents. Spin liquids in frustrated magnets. *Nature* 464(7286) (2010), 10.
- [40] Z. Guguchia et al. Tunable anomalous Hall conductivity through volume-wise magnetic competition in a topological kagome magnet. *Nature Communications* 11(1) (2020), 559.
- [41] *Wikipedia-Topology* <https://en.wikipedia.org/wiki/Topology>. Wikimedia Foundation.
- [42] T. Liu. Dirac materials and the response to elastic lattice deformation Retrieved from <https://open.library.ubc.ca/collections/ubctheses/24/items/1.0379912>. PhD thesis. University of British Columbia, 2019.

-
- [43] A. A. Soluyanov. Topological aspects of band theory. Retrieved from <https://doi.org/doi:10.7282/T3N0159G>. PhD thesis. Rutgers, The State University of New Jersey, 2012.
- [44] Q. Wu et al. WannierTools: An open-source software package for novel topological materials. *Computer Physics Communications* 224 (2018), 405–416.
- [45] *Line graphs: Kagom'e and Checkerboard Lattices*. https://courses.physics.ucsd.edu/2019/Fall/physics239/LECTURES/line_graphs.pdf. 2019.
- [46] A. J. Kollár, M. Fitzpatrick, P. Sarnak, and A. A. Houck. Line-Graph Lattices: Euclidean and Non-Euclidean Flat Bands, and Implementations in Circuit Quantum Electrodynamics. *Communications in Mathematical Physics* 376(3) (2020), 1909–1956.
- [47] R. Chisnell et al. Topological Magnon Bands in a Kagome Lattice Ferromagnet. *Physical Review Letters* 115 (14 2015), 147201.
- [48] Q. Xu et al. Topological surface Fermi arcs in the magnetic Weyl semimetal $\text{Co}_3\text{Sn}_2\text{S}_2$. *Physical Review B* 97(23) (2018), 235416.
- [49] W. Luo, Y. Nakamura, J. Park, and M. Yoon. Cobalt-based magnetic Weyl semimetals with high-thermodynamic stabilities. *npj Computational Materials* 7(1) (2021), 2.
- [50] Y. Wang, J. Lv, L. Zhu, and Y. Ma. Crystal structure prediction via particle-swarm optimization. *Physical Review B* 82(9) (2010), 094116.
- [51] F. Bechstedt. *Many-Body Approach to Electronic Excitations*. Vol. 181. Springer Series in Solid-State Sciences. Springer Berlin Heidelberg, 2015.
- [52] B. Lv et al. Experimental Discovery of Weyl Semimetal TaAs. *Physical Review X* 5(3) (2015), 031013.
- [53] B. Q. Lv et al. Observation of three-component fermions in the topological semimetal molybdenum phosphide. *Nature* 546(7660) (2017), 627–631.
- [54] M. V. Berry. Quantal phase-factors accompanying adiabatic changes. *Proceedings of the Royal Society A* 392 (1984), 45.
- [55] H. Nielsen and M. Ninomiya. Absence of neutrinos on a lattice: (II). Intuitive topological proof. *Nuclear Physics B* 193(1) (1981), 173–194.
- [56] H. Nielsen and M. Ninomiya. Absence of neutrinos on a lattice: (I). Proof by homotopy theory. *Nuclear Physics B* 185(1) (1981), 20–40.

- [57] C. Fang, M. J. Gilbert, X. Dai, and B. A. Bernevig. Multi-Weyl Topological Semimetals Stabilized by Point Group Symmetry. *Physical Review Letters* 108 (2012), 266802.
- [58] A. A. Soluyanov et al. Type-II Weyl semimetals. *Nature* 527(7579) (2015), 495–498.
- [59] M. Z. Hasan, S.-Y. Xu, I. Belopolski, and S.-M. Huang. Discovery of Weyl Fermion Semimetals and Topological Fermi Arc States. *Annual Review of Condensed Matter Physics* 8(1) (2017), 289–309.
- [60] B. Yan and C. Felser. Topological Materials: Weyl Semimetals. *Annual Review of Condensed Matter Physics* 8(1) (2017), 337–354.
- [61] A. A. Soluyanov and D. Vanderbilt. Computing topological invariants without inversion symmetry. *Physical Review B* 83(23) (2011), 235401.
- [62] A. A. Mostofi et al. wannier90: A tool for obtaining maximally-localised Wannier functions. *Computer Physics Communications* 178(9) (2008), 685–699.
- [63] R. D. King-Smith and D. Vanderbilt. Theory of polarization of crystalline solids. *Physical Review B* 47(3) (1993), 1651–1654.
- [64] K. G. Wilson. Confinement of quarks. *Physical Review D* 10(8) (1974), 2445–2459.
- [65] R. Yu et al. Equivalent expression of \mathbb{Z}_2 topological invariant for band insulators using the non-Abelian Berry connection. *Physical Review B* 84(7) (2011), 075119.
- [66] M. Taherinejad, K. F. Garrity, and D. Vanderbilt. Wannier center sheets in topological insulators. *Physical Review B* 89(11) (2014), 115102.
- [67] X.-L. Sheng et al. Topological insulator to Dirac semimetal transition driven by sign change of spin-orbit coupling in thallium nitride. *Physical Review B* 90(24) (2014), 245308.
- [68] Y. Sun et al. Prediction of Weyl semimetal in orthorhombic MoTe_2 . *Physical Review B* 92(16) (2015), 161107.
- [69] P. Blaha et al. *WIEN2k: An Augmented Plane Wave plus Local Orbitals Program for Calculating Crystal Properties*. Vienna University of Technology, 2018.
- [70] P. Blaha et al. WIEN2k: An APW+lo program for calculating the properties of solids. *The Journal of Chemical Physics* 152(7) (2020), 074101.
- [71] P. Hohenberg and W. Kohn. Inhomogeneous Electron Gas. *Physical Review* 136(3B) (1964), B864–B871.

- [72] W. Kohn and L. J. Sham. Self-Consistent Equations Including Exchange and Correlation Effects. *Physical Review* 140(4A) (1965), A1133–A1138.
- [73] J. Kunes et al. Wien2wannier: From linearized augmented plane waves to maximally localized Wannier functions. *Computer Physics Communications* 181(11) (2010), 1888–1895.
- [74] S. Ahmed et al. BerryPI: A software for studying polarization of crystalline solids with WIEN2k density functional all-electron package. *Computer Physics Communications* 184(3) (2013), 647–651.
- [75] D. Voßwinkel, O. Niehaus, and R. Pöttgen. New Rhodium-rich Germanides $RERh_6Ge_4$ ($RE = Y, La, Pr, Nd, Sm-Lu$): Rhodium-rich Germanides $RERh_6Ge_4$. *Zeitschrift für anorganische und allgemeine Chemie* 639(14) (2013), 2623–2630.
- [76] Y. Zhu et al. Evidence from transport measurements for YRh_6Ge_4 being a triply degenerate nodal semimetal. *Physical Review B* 101(3) (2020), 035133.
- [77] P.-J. Guo, H.-C. Yang, K. Liu, and Z.-Y. Lu. Triply degenerate nodal points in RRh_6Ge_4 ($R = Y, La, Lu$). *Physical Review B* 98(4) (2018), 045134.
- [78] *BerryPI: A software for the calculation of Berry phase and related properties of solids*. <https://github.com/spichardo/BerryPI>. 2021.
- [79] J. P. Perdew, K. Burke, and M. Ernzerhof. Generalized Gradient Approximation Made Simple. *Physical Review Letters* 77 (18 1996), 3865–3868.
- [80] A. Kokalj. XCrySDen—a new program for displaying crystalline structures and electron densities. *Journal of Molecular Graphics and Modelling* 17(3-4) (1999), 176–179.
- [81] P. E. Blöchl. Projector augmented-wave method. *Physical Review B* 50(24) (1994), 17953–17979.
- [82] G. Kresse and D. Joubert. From ultrasoft pseudopotentials to the projector augmented-wave method. *Physical Review B* 59(3) (1999), 1758–1775.
- [83] G. Kresse and J. Hafner. *Ab initio* molecular dynamics for liquid metals. *Physical Review B* 47(1) (1993), 558–561.
- [84] G. Kresse and J. Furthmüller. Efficiency of *ab-initio* total energy calculations for metals and semiconductors using a plane-wave basis set. *Computational Materials Science* 6(1) (1996), 15–50.
- [85] G. Kresse and J. Furthmüller. Efficient iterative schemes for *ab initio* total-energy calculations using a plane-wave basis set. *Physical Review B* 54(16) (1996), 11169–11186.

Bibliography

- [86] C. K. Barman, C. Mondal, B. Pathak, and A. Alam. Symmetry-driven topological phases in $X\text{AgBi}$ ($X = \text{Ba}, \text{Sr}$): An *ab initio* hybrid functional calculation. *Physical Review Materials* 4(8) (2020), 084201.
- [87] Z. Zhu et al. Triple point topological metals. *Physical Review X* (3 2016), 031003.
- [88] A. Wang et al. A framework for quantifying uncertainty in DFT energy corrections. *Scientific Reports* 11(1) (2021), 15496.
- [89] B. Keimer and J. E. Moore. The physics of quantum materials. *Nature Physics* 13(11) (2017), 1045–1055.
- [90] S. S. Tsirkin, I. Souza, and D. Vanderbilt. Composite Weyl nodes stabilized by screw symmetry with and without time-reversal invariance. *Physical Review B* 96 (4 2017), 045102.
- [91] N. Nagaosa, T. Morimoto, and Y. Tokura. Transport, magnetic and optical properties of Weyl materials. *Nature Reviews Materials* 5(8) (2020), 045102.
- [92] D. Hsieh et al. Observation of Unconventional Quantum Spin Textures in Topological Insulators. *Science* 323(5916) (2009), 919–922.
- [93] P. Hosur and X. Qi. Recent developments in transport phenomena in Weyl semimetals. *Comptes Rendus Physique* 14(9) (2013), 857–870.
- [94] E. Liu et al. Giant anomalous Hall effect in a ferromagnetic kagome-lattice semimetal. *Nature Physics* 14(11) (2018), 8.
- [95] A. Jain et al. The Materials Project: A materials genome approach to accelerating materials innovation. *APL Materials* 1(1) (2013), 011002.
- [96] I. Anusca et al. Half Antiperovskites: IV. Crystallographic and Electronic Structure Investigations on $\text{A}_2\text{Rh}_3\text{S}_2$ ($\text{A} = \text{In}, \text{Sn}, \text{Tl}, \text{Pb}, \text{Bi}$). *Zeitschrift für anorganische und allgemeine Chemie* (2009), 2410–2428.
- [97] J. C. Slater. Atomic Radii in Crystals. *The Journal of Chemical Physics* 41(10) (1964), 3199–3204.
- [98] *Wikipedia-Oxidation state* https://en.wikipedia.org/wiki/Oxidation_state.
- [99] J. P. Perdew, K. Burke, and M. Ernzerhof. Generalized Gradient Approximation Made Simple. *Physical Review Letters* 77(18) (1996), 4.
- [100] K. Momma and F. Izumi. *VESTA3* for three-dimensional visualization of crystal, volumetric and morphology data. *Journal of Applied Crystallography* 44(6) (2011), 1272–1276.

Bibliography

- [101] The atomic simulation environment—a Python library for working with atoms. *Journal of Physics: Condensed Matter* 29(27) (2017), 273002.
- [102] W Schnelle et al. Ferromagnetic ordering and half-metallic state of $\text{Co}_3\text{Sn}_2\text{S}_2$ with the shandite-type structure. *Physical Review B* 88(14) (2013), 8.
- [103] M. Holder et al. Photoemission study of electronic structure of the half-metallic ferromagnet $\text{Co}_3\text{Sn}_2\text{S}_2$. *Physical Review B* 79(20) (2009), 205116.
- [104] R. Weihrich, I. Anusca, and M. Zabel. Half-Antiperovskites: Structure and Type-Antitype Relations of Shandites $\text{M}_{3/2}\text{AS}$ (M: Co, Ni; A: In, Sn). *ChemInform* 36 (35 2005).
- [105] J. E. Saal et al. Materials Design and Discovery with High-Throughput Density Functional Theory: The Open Quantum Materials Database (OQMD). *Journal of The Minerals* 65(11) (2013), 1501–1509.
- [106] S. Kirklin et al. The Open Quantum Materials Database (OQMD): assessing the accuracy of DFT formation energies. *npj Computational Materials* 1(1) (2015), 15010.
- [107] A. Benisek and E. Dachs. The accuracy of standard enthalpies and entropies for phases of petrological interest derived from density-functional calculations. *Contributions to Mineralogy and Petrology* 173(11) (2018), 90.